ASPECTS OF WIMP DARK MATTER:
Multi-wavelength signals and Extra-dimension scenarios

Thesis submitted for the degree of
Doctor Philosophiæ

October 2008

CANDIDATE

Marco Regis

SUPERVISOR

Prof. Piero Ullio

Abstract

Weakly interacting massive particles (WIMPs) are among the leading candidates for the dark matter (DM) component in the Universe. The thesis presents a review of the current status of the DM problem, focussing on the WIMP paradigm and discussing motivations, properties, examples, and detection prospects.

As a novel approach to detect WIMP dark matter, we analyze the multi–wavelength signals induced by WIMP pair annihilations in DM halos. We perform, in particular, a systematic study on the Galactic center (GC) region for a generic WIMP scenario. Depending on the uncertainties of the astrophysical environment, we discuss spectral and angular features, and sketch correlations among signals in the different energy bands. We find that none of the components which have been associated to the GC source Sgr A*, nor the diffuse emission components from the GC region, have spectral or angular features typical of a DM source. Still, data-sets at all energy bands contribute to place significant constraints on the WIMP parameter space.

We turn then to a specific WIMP model, showing how to embed a viable WIMP dark matter candidate in a five–dimensional (5D) theory with a non-universal flat extra-dimension. In a large fraction of the parameter space, the first Kaluza–Klein (KK) mode of a 5D Abelian gauge field is the lightest KK particle odd under a certain discrete $\mathbf{Z}_2$ symmetry, which had been introduced to improve the naturalness of the model. Electroweak bounds force the mass of this particle above the TeV scale, in a range at which the pair annihilation rate would be to too small to provide a thermal relic abundance compatible with the DM density in the Universe today; on the other hand, "coannihilations" in the early Universe with other KK particles of the model, which are strongly interacting and nearly degenerate in mass with the DM candidate, lead naturally to the correct relic density.

For such a heavy WIMP dark matter candidate, detection is especially hard. The related multi-wavelength emission at the GC is expected to be faint, unless a significant enhancement of the DM density is present in the central region of the Milky Way. If this is the case, and depending on few additional assumptions, we find that next-generation gamma-ray and wide-field radio observations can test the model, possibly even with the detection of the induced monochromatic gamma-ray emission.

Preface

Before of my diploma courses, I was unaware that the 96% of the energy content of the Universe is commonly considered to be dark, or better, unknown (maybe, even because it was not well established yet). The fact that the ordinary matter constitutes less than the 4% was, for me, a puzzling and amazing discovery. Cosmological arguments drove me towards the dark matter (DM) subject.

On the other hand, my formation as undergraduated student proceeded strictly on the particle physics side. The convergence to astroparticle physics became foreseeable. Actually, it was completed during the introductory courses in my first year at SISSA. In this context, I also became fully aware about the great potentialities for astroparticle studies at the present time. The main scope of this thesis is to report most of the work done in the subsequent three years, contextualizing it in its general ground, namely, the weakly interacting massive particle (WIMP) DM framework.

The outline of the thesis is as follows: In the Introduction, we review dark matter (DM) gravitational evidences on cosmological, cluster and galactic scales. Proposed solutions are discussed, focusing on theories of modified gravity and baryonic and non-baryonic DM.

In Chapter 2, we concentrate on the WIMP DM scenario. WIMPs can arise in many extensions to the standard model (SM) of particle physics and easily fit in the standard cosmological scenario, being a thermal relic component. We discuss the basics of the WIMP paradigm, drawing particular attention to the chemical and kinetic decouplings in the primordial Universe. Examples of WIMP models and observational prospects are outlined.

Chapter 3 is devoted to multi-wavelength indirect signals of WIMP annihilations. We focus, in particular, on the innermost region of the Galaxy and summarize currently available observations on the Galactic center. The DM source and the related mechanisms of photon production are described. We compute the approximate scalings of the multi–wavelength spectrum and perform the full treatment for some benchmark models. Then, we compare the DM–induced signal with the present limits and with the projected constraints of forthcoming experiments. Finally, the cases of galaxy clusters, dwarf spheroidal galaxies and galactic clumps are briefly discussed.

In Chapter 4, we outline possible solutions for the gauge hierarchy prob-

lem of the SM in the context of extra-dimension scenarios, with particular attention devoted to models which can simultaneously account for the DM content in the Universe. We present a recently proposed DM candidate. Some ingredients of the model, namely, the symmetry making the WIMP stable and the mass spectrum, are extensively discussed. We compute the relic density for two different scenarios and we add some remarks about the fine–tuning. Prospects for the detection of the WIMP candidate through the multi-wavelength signals induced by annihilations at the GC are highlighted. Various details regarding the Feynman rules in the model, a one–loop mass splitting computation, and the list of all processes relevant for the relic density calculation are contained in the appendices.

Chapter 5 concludes.

I should greatly thank my Ph.D. supervisor, my family, my girlfriend, my friends, etc.. An enormous amount of people have contributed to this thesis with their support and in various ways. Moreover, it's not falling into the banal to mention that most of our thoughts, actual possibilities, and quality of life are based on the efforts and thoughts of billions of persons during the past and present time. According to me, acknowledgments are intrinsically a partial and suspicious procedure.

Nevertheless, it's very nice to remember people who stayed more directly and deeply in contact with me during these four years at SISSA. On the other hand, I hope that everyone found his/her benefit in sharing the time with me (even in boring and exerting helps or supports). We don't need to repeat we are grateful to each other. The best way to thank I consider is staying in touch.

Contents

Chapter 1

Introduction

The definition of the concept of matter has historically undergone many transformations and much debate. For the common sense, the term matter[1] identifies that out of which anything is made or composed. Plato introduces a dichotomy between matter (related to raw material, imperfect) and shape (related to ideals, namely to God, and perfect), which, with mutated forms and refined treatments, has became recurrent in epistemology. Applied to human beings, this sounds as the more familiar distinction between body (material, mortal, and causally determined) and soul (ideal, immortal, and endowed with free will).

According to Descartes, we know only what is in our own consciousnesses. The question of the real and the ideal, namely the question concerning what in our knowledge is objective and what subjective, led in Western philosophy to the opposition between idealism, which relates our knowledge to subjective mental ideas, and materialism, where the real has an absolute objective existence. Most of the formulations of the latter imply reductionism, according to which a phenomenon considered at one level of description, can be expressed in terms of other phenomena at a more general and fundamental level.

Exposing us to several criticisms, we can say that any physicist implicitly adopts a materialist perspective in the day-to-day work. The opposite of matter (res extensa) is not spirit (res cogitans), but rather anti-matter, where, actually, the conceptual symmetry matter/antimatter includes the latter in an extended definition of matter. General relativity (GR) and quantum field theory (QFT) (which constitute the theoretical ground of this thesis) have modified the traditional concept of matter. Indeed, strictly speaking, from a particle physics point of view, matter means a fermionic spin one-half particle. Interactions are described through exchanges of other particles, the gauge bosons. Even keeping away from the question of how

[1] The word matter comes from the Latin *materia*, which meaning was wood for building, opposed to *lignum*, namely the wood for fuel

this is a way to describe the reality or the reality itself, this formulation can be easily accommodate in a materialist theory, by enlarging the traditional definition of matter. This is definitively required also by the compelling evidence for a new form of matter which is arisen in the last decades. This is the dark matter (DM).

The first claim for the existence of DM, in the modern sense, was done by Zwicky in 1933 [1]. He derives this conclusion by observing an unexpectedly large velocity dispersion in the Coma cluster. A missing mass problem in clusters of galaxies was also found in Virgo in 1936 [2]. On the other hand, initially, few astronomers paid attention to these results. The incredibly small number of citations (probably around 15 [3]) of the Zwicky's paper before the late 70's was not only due to the fact that it was written in German and published in a not so popular journal. Many alternative explanations were invoked for the mentioned phenomena. Only a clear determination of the cluster properties, like the hot gas mass from its X-ray radiation, and a compelling evidence for the presence of DM in individual galaxies [4, 5], make the DM hypothesis to be investigated in depth. Nowadays, observations of the cosmic microwave background (CMB) anisotropies strongly suggest the presence of a cosmological relevant amount of cold dark matter, where the term cold refers to slowly moving particles.

So far, the evidences for DM are gravitational evidences (restricting, conservatively, on experimental results and interpretations having a wide consensus). Such results require a solution either in the modification of the laws of gravitation or in the prediction of an unseen form of matter. To some extent, the case of DM is analogous to past controversies about deviations of the planetary motions from the expected orbits. The first solution is successful, e.g., in the case of Mercury, leading to GR, while the second approach, applied to Uranus, led to the Neptune discovery.

Currently, the DM hypothesis is introduced to explain some gravitational anomalies extending from cosmological to galactic scales. In this respect, any of the theory of modified gravity proposed so far show, for various reasons, some drawbacks. Moreover, particle DM can be embedded in most of the models proposed to solve particle physics issues.

The forthcoming years will be very promising and attractive for sheding light on the DM hypothesis. More than 15 experiments aimed to the direct detection of DM particles are currently running or under construction. Few days ago, the Large Hadronic Collider (LHC) [6] started the commissioning phase with beam; it will test extensions to the standard model (SM) of particle physics up to energies of few TeV. Space satellite experiments and ground based telescopes are going to probe different DM induced signals from astrophysical structures with highly improved sensitivities and angular resolutions. The next generation of CMB experiments can reconstruct the primordial density distribution of DM.

The challenge for the discovery of the elusive nature of dark matter is in

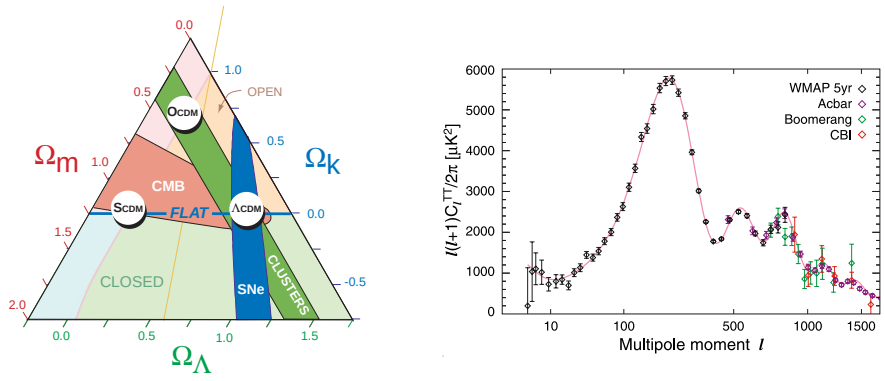

Figure 1.1: *Left Panel:* The Cosmic Triangle [7]. This triangle represents the three key cosmological parameters (Ω_m, Ω_Λ , and Ω_k), where each point in the triangle satisfies the sum rule $\Omega_m + \Omega_\Lambda + \Omega_k = 1$. The observational constraints from measurements at low redshift (clusters), intermediate redshift (SNe), and high redshift (CMB) are shown by the three color bands. They select the so called ΛCDM model, with $\Omega_m \simeq 1/4$, $\Omega_\Lambda \simeq 3/4$, and $\Omega_k = 0$. *Right Panel:* Temperature angular power spectrum versus multiple moment, from WMAP 5-year, ACBAR, Boomerang, and CBI data. The red curve is the best-fit ΛCDM model to the WMAP data. Figure from [8].

a promising era.

1.1 Gravitational Evidences

1.1.1 Dark Matter on Cosmological Scales

During the last decade, our understanding of cosmology have experienced tremendous progresses, allowing to distinguish among cosmological models, as shown in Fig. 1.1a. As a cornerstone, the measurement of the power spectrum of cosmic microwave background anisotropies (Fig. 1.1b) led to a detailed determination of cosmological parameters. The total amount of energy in the Universe, ${\Omega_{tot}}^2$, can be inferred through the positions of peaks in the spectrum (in particular of the first peak). Indeed, the peaks appear at harmonics of the the sound horizon scale at last scattering. The ratio between the measured apparent angular scale (~ 0.6 degree) and the physical scale depends on the curvature of the Universe, which is in turn induced by the total amount of energy. Latest results extracted by the WMAP

[2]Cosmological energy densities are often expressed in terms of $\Omega_i h^2 = \rho_i/\rho_c\, h^2$, where ρ_i is the energy density of a species of particle i , $\rho_c = 1.879 \times 10^{-29} h^2 \mathrm{g/cm}^3$ is the critical density (i.e., implying $\Omega = 1$), and $h = 0.730 \pm 0.019$ is the Hubble constant in units of $100\,\mathrm{km\,s^{-1}\,Mpc^{-1}}$.

collaboration from CMB data alone have found Ω_{tot} to be compatible[3] with one ($\Omega_{tot} = 1 - \Omega_k = 1.01 \pm 0.01$ [9]), namely a strong indication for a Universe with flat geometry. The constraint on the geometry becomes much more stringent ($\Omega_{tot} = 1.0052 \pm 0.0064$ [10]) combining CMB measurements with other cosmological observations, like Supernovae type Ia (see below), since there is a degeneracy with the distance of the last scattering surface, namely with the expansion rate of the Universe.

Baryons increase the effective mass of the photon-baryon fluid and make the fluid fall deeper in the potential well. This changes the relative strength of the peaks. Indeed, the amplitudes of the odd peaks (due to compressions) become enhanced relative to the even peaks (due to rarefactions). Moreover, a subdominant Doppler effect indicates a significant baryon content, which increases the effective mass, reducing the velocity of the oscillations. The ratio between the first and the second peaks of the CMB anisotropy spectrum can be therefore exploited to determine the baryon density, which is found to be $\Omega_b h^2 = 0.02273 \pm 0.00062$ [9] (hereafter, we report parameters derived from the 6 parameter ΛCDM model).

The effect of DM is to increase the potential wells and, thus, to boost the odd peaks, associated to adiabatic and gravitational density fluctuations. Moreover, radiation decayed potential wells in the radiation era and this would eliminate alternating peak heights. This effect depends strongly on the ratio between matter and radiation, i.e., on the epoch of matter-radiation equality. The amplitude of the third peak, compared with the first and second, strongly constrains the DM density: $\Omega_{CDM} h^2 = 0.1099 \pm 0.0062$ [9] (the acronym CDM refers to cold dark matter, whose properties will be discussed in Section 1.3.2)

The first point we have to note is that the total matter density $\Omega_m = 0.258 \pm 0.030$ is definitively different from Ω_b at a very high precision. Most of the matter component in the Universe is not protons or neutrons or any kind of matter detected in accelerator experiments so far.

Acoustic oscillations, arising in the photon-baryon plasma from the competition between gravitational attraction and gas pressure, are imprinted on the distribution of matter, traced by the distribution of galaxies. Baryon acoustic oscillations (BAO) in the three-dimensional matter power spectrum were recently detected at low redshift in the 2dFGRS and Sloan Digital Sky Survey (SDSS) galaxy samples, with the latest SDSS data-precision (surveys of $700,000$ galaxy redshifts) allowing to determine cosmological parameters [11]. They are consistent with the CMB data, and the Ω_m extracted confirms the need for non-baryonic DM. The oscillations leave their imprint on very large scales, roughly 100 Mpc/h, and this agreement seems to indicate that structure formation on these scales is rather well understood.

[3]This value assumes a 7 parameter model, namely the standard 6 parameter ΛCDM model plus allowing a non-zero curvature.

Another important way to determine the baryon density of the Universe is based on Big-Bang Nucleosynthesis (BBN), namely the synthesis of light nuclei (i.e., D, ^{3}He, ^{4}He, ^{7}Li) in the primordial Universe. At present, observations of these nuclei in a variety of astrophysical sites (stars, Galactic and extragalactic HII regions, etc.) have allowed quite precise estimates of their primordial abundances, providing a stringent constraint to Ω_b (for a review on BBN, see e.g., [12] and reference therein). The inferred value is consistent with the baryon density obtained from the CMB data, $\Omega_b h^2 = 0.0216 \pm 0.0020$. This fact gives us confidence about the estimate of the baryonic content of the Universe, since the two data refer to very different epochs: T $\sim$ 0.1 eV for CMB and T $\sim$ 1 MeV for BBN (see the history of the Universe in Sec. 2.2.1).

Supernovae (SN) are among the most important cosmological distance indicator. The total energy density of the Universe can be inferred through magnitude measurements for objects distant enough so that the spatial curvature can affects the result in a sizable way. SN type Ia, discovered at redshifts larger than 0.3, constitutes a very useful tool for this investigation. SN observations imply that the expansion of the Universe is accelerating [13, 14], and point toward the presence of a form of energy (i.e., the dark energy) responsible for it (whose cosmological density is denoted by Ω_Λ). Putting together SN type Ia, BAO and WMAP data, $\Omega_{CDM} h^2 = 0.1143 \pm 0.0034$ [10].

Another contribution in improving constraints on cosmological parameters, can be given by Lyman-α (Lyα) forest observations (i.e., the absorption observed in distant quasar spectra, caused by neutral hydrogen in the intergalactic medium). It can probe the matter power spectrum at high redshift, providing information on smaller scales. Present data are consistent with the ΛCDM picture [15].

1.1.2 Dark Matter on Cluster Scales

In 1933, the Swiss astrophysicist Fritz Zwicky [1] estimated the mass of Coma cluster, by measuring the velocity dispersion (through the Doppler effect associated to the observed redshift) of some galaxies in the cluster and applying the virial theorem. Measuring the total brightness of the cluster, he found a mass-to-light ratio exceeding by two orders of magnitude the ratio in the solar neighborhood. He was the first inferring, based on experimental evidences, the existence of an invisible form of matter, holding the cluster together.

Today the mass of a cluster can be estimated through three independent methods: the motion of galaxies in the cluster (i.e., through the dispersion velocity, as Zwicky did), gravitational lensing and thermal X-ray emissions (which can provide the temperature of the hot intra-cluster gas).

GR predicts light deflection in presence of a gravitational field. By observing the distorsion in the image of some background objects induced by

the gravitational potential of a cluster, one can infer the cluster mass generating such a lensing phenomenon. If the lens is strong enough to form multiple images or giant arcs, this effect is called strong gravitational lensing. In the weak lensing regime, on the other hand, the background objects are still stretched and magnified, but by small amounts which are hard to measure. However, the presence of a cluster mass can be detected, looking at the systematic alignment of background sources around the lensing mass. A list of clusters, that had their dark matter content measured using weak gravitational lensing, is reported in the compilation of [16].

For rich cluster, the mass can be also inferred by measuring the temperature of the gas through its X-ray emission. The intensity of the latter traces the gas density, which is the dominant baryonic component of clusters. Considering hydrostatic equilibrium, the balance between gravity and pressure leads to a relation between the cluster mass enclosed within the radial distance r and the temperature T. Assuming the mentioned baryonic mass, it reads: $kT \sim 1.5\,\mathrm{keV}\frac{M(r)}{10^{14}M_{\odot}}\frac{1\,Mpc}{r}$. The observed temperature (T$\sim$ 10 keV) is incompatible with this estimate, implying a DM component.

If there are no mechanism other than gravitational collapse for organizing matter on large scales, then the fraction of matter (and baryons) in clusters, which form in the present epoch, should be representative of the cosmic average. There is good agreement among the mentioned estimators for the mass of clusters [17], leading to $\Omega_m \simeq 0.2 - 0.3$, which is consistent with cosmological constraints. This value implies a cosmic mass-to-light ratio $\rho_m/\rho_L \sim 400\,hM_{\odot}/L_{\odot}$, where $\rho_L \sim 5 \cdot 10^{-4} L_{\odot}/M_{\odot}\,\rho_c/h$ is the luminosity density of the Universe. Including the contribution of their DM halo, galaxies have a typical mass-to-light ratio $\rho_m/\rho_L \sim 10\,hM_{\odot}/L_{\odot}$. Therefore, it turns out that galaxies contribute less than 3% to the mass content of the Universe and DM appears mostly distributed in large scale structures.

In August 2006, Clowe et al. [18] reported a compelling (probably the most compelling on cluster scale) evidence for DM. They observed the so-called Bullet cluster (1E0657-558), a very massive system consisting of a main cluster which has been recently crossed, at a very high speed, by a satellite cluster (namely, the bullet). During the merger, the dynamics of galaxies within each of the two clusters, observable in visible light, was not greatly altered. As expected, galaxies behave as a collisionless fluid. The hot gases (i.e., the dominant mass component in the two sub-clusters), detected by their X-rays emission, dramatically slow down since electromagnetic interactions, generating an offset from the galaxies toward the center of the system. By gravitational lensing of background objects, they mapped the gravitational potential. In theories of modified gravity, it would be expected to trace the plasma distribution (i.e., the collisional component). However, the lensing is strongest in two separated regions, near the visible galaxies. This has been considered as a clear indication of the existence of collisionless

DM.

An independent method for estimating the baryonic fraction in clusters is the Sunyaev-Zel'dovich effect (SZE). A small fraction of CMB photons are heated by inverse Compton scattering with intra-cluster electrons, distorting the Planck black-body spectrum. In Bullet cluster, the SZE map has a broadly similar morphology to that in existing X-ray maps.

1.1.3 Dark Matter on Galactic Scales

Rotation velocity (RC) for rotationally supported galaxies (e.g., spirals) or velocity dispersion for pressure supported galaxies (e.g., ellipticals and dwarfs spheroidal) can be exploited to estimate the kinematical mass of the system (assuming Newtonian gravitation). Luminosity measurements can then determine the mass-to-light ratio.

For spirals, RCs can be traced using optical (Hα) observations for the inner part and radio (HI lines) data at large radii. According to Newtonian dynamics and assuming that mass in galaxies traces the distribution of stars and gas, spiral galaxies show a discrepancy between the predicted orbital speed v_r and the observed one. The predicted rotational velocity for stars is:

$$v_r(r) = \sqrt{\frac{G\,M(r)}{r}}\ , \tag{1.1}$$

where G is the Newton's constant, r is the distance from the center of the galaxy and M is the mass of the galaxy inside r. Newtonian gravitation predict that rotation curves should fall as $r^{-1/2}$ outside the bright parts of galaxies (where $M(r) \simeq$ const.). As first pointed out by Rubin et al. [4] (and confirmed by Bosma [5]) in the late 70's, the RC of disk galaxies does not show such Keplerian fall-off in correspondence to the stellar and gas distribution fall-off. The most intuitive explanation is the presence of an invisible mass component. Moreover, a DM halo appeared to be essential to dynamically explain the stability of the disk of spiral galaxies. Indeed, without being embedded within massive halos, self-gravitating disks lead to bar instabilities.

At the time of writing, many hundreds of RCs of spiral galaxies have been analyzed (for a recent review on DM in spiral galaxies, see, e.g., [19] and references therein). In few tens of them, the observations are free from most of the experimental bias and non-axisymmetric disturbances. In these galaxies, the observable quantity, namely, the projection on the line of sight of the tangential velocity, has been identified with v_r with very high precision. The component of the velocity non-related to the central potential is found to be negligible and the measured velocity represents a good tracer for the gravitational potential. At the present time, the presence of DM in spiral galaxies is very well established.

RCs in spirals can be generally represented, out to their virial radius, by a universal function of radius; the spherical halo mass, eventually involving few other quantities, determines at any radii the circular velocity of any spiral.

An example of RC is shown in Fig. 1.2. Spiral galaxies have three luminous components: a stellar bulge, a thin stellar disk and an extended thin gas disk. The circular velocity is obtained by summing in quadrature the luminous and halo contributions. The reconstruction of RCs for galaxy with a significant bulge component can be hard to be performed. The mass (and thus the potential) of the gas component can be directly inferred through its HI line emissions. The velocity induced by the gravitational potential associated to the stellar disk is usually described with one free parameter, which is fitted by observation of RCs. However, it is also quite strongly constrained by fitting their spectral energy distribution with spectro-photometric models. As shown in Fig. 1.2, the latter is often the dominant luminous component in the inner part, while in the outer region gas can dominate.

First observations of spirals seemed to indicate a nearly constant v_r at large radii and it had suggested a halo distribution $\rho \propto r^{-2}$, i.e. an isothermal profile. On the other hand, it has been now established that only a minority of the observed RCs of spirals are asymptotically flat. The RC slope has found to take values from 1 to -1/2 (Newtonian) [19].

If elliptical galaxies originate from major mergers of spiral galaxies, then they should possess dark matter halos. However, for ordinary ellipticals, the picture is more controversial than for spirals, even because lack of velocity tracers at large distances from the center (bright planetary nebulae provide a tool for extracting the velocity dispersion). Nevertheless, while appearing with lower mass-to-light ratios, measurements of ellipticals still indicate a DM content [20].

The so-called Low-Surface-Brightness galaxies (LSB) are the most interesting galaxies for DM studies, since their mass density is probably dominated by DM in all regions, and the disentanglement between dark and luminous components becomes easier. Most LSB are dwarf galaxies. Very recently, based on SDSS observations on a large number of extremely low-luminosity satellites of Milky Way and M31, the DM hypothesis in dwarf spheroidal (dSph) galaxies has been strengthened [21]. DSphs generally consist of a stellar population, with little gas and dust components (for a review on dSph, see,e.g., [22]). The mass distribution generating the gravitational potential of a collisionless system like a stellar population could be inferred solving the Boltzmann equation. It requires position and velocity of several stars and it is not usually applyable to dSph galaxies. Projecting the 6D phase space density into a set of 3D functions (momenta of the velocity distribution), one can derive the Jeans equation, that is the equation for the first momentum, namely the velocity dispersion. Assuming staticity and

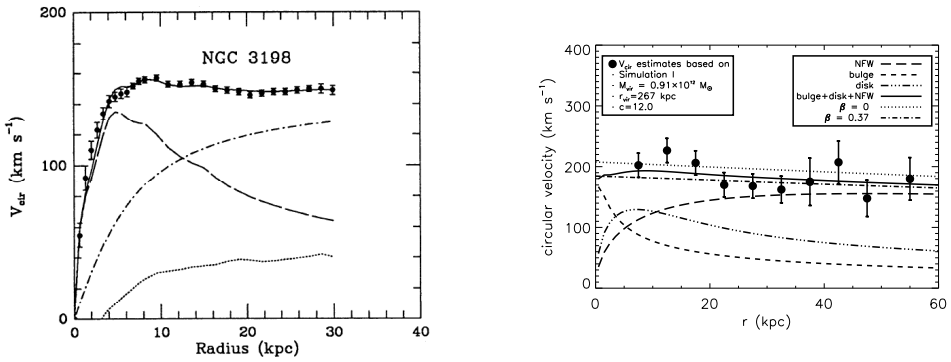

Figure 1.2: *Left Panel:* Rotation curve of the spiral galaxy NGC 3198. Contributions from gas, disk and DM halo are shown with dotted, dashed and dash-dotted lines, respectively. From Ref. [24]. *Right Panel:* Milky Way RC at large radii: The solid line is the best-fit circular velocity curve constructed by a combination of stellar bulge, disk and NFW DM profile. The large symbols are the circular velocity estimates. For details, see Ref. [25].

spherical symmetry, it takes the form:

$$\frac{G\,M(r)}{r}\nu(r) + 2\beta(r)\nu(r)\sigma_r^2 + r\frac{\partial}{\partial r}[\nu(r)\sigma_r^2] = 0 \ , \tag{1.2}$$

where σ_r is the radial velocity dispersion (obtained from the observed line-of-sight velocity dispersion), ν is the stellar density profile and $\beta = 1 - \sigma_\theta^2/\sigma_r^2$ is the velocity anisotropy, with σ_θ being the tangential velocity dispersion. Having measured σ_r and traced the stellar population, the determination of the mass distribution still requires a guess for the anisotropy of stellar velocity. It is very weakly constrained by other observations and simulations. The simplest choice is to assume β to be a constant parameter. The sketched procedure leads to a compelling evidence for a mass discrepancy in dSph galaxies and the conclusion is not crucially affected by the uncertainty on β.

Further, gravitational lensing and X-ray observations provide evidences for DM on galactic scale, and we refer the interested readers to, e.g., Ref. [23] (and references therein).

Milky Way

Our location within the Galaxy allows to probe some properties of the Milky Way in a unique way, including its mass content and the shape of the DM halo. On the other hand, the position complicates some measurements, such as, for example, the extended rotation curve of gas in its disk.

The methods exploited in order to quantify the halo mass profile include the velocity dispersion profile of the tracer populations, the escape velocity and the circular velocity curve. Very recently, the RC at radii between

7.5 and 60 kpc was mapped by the SDSS collaborations [25], using blue horizontal-branch halo stars as kinematic tracers. For the inner RC, we refer to the CO-survey reported in [26]. Such RCs (and escape velocity data as well) cannot put, however, very stringent constraints or definitively discriminate between halo models.

As shown in Fig. 1.2b, the circular velocity estimated in [25] varies mildly with radius, dropping from ~ 220 km s^{-1} at 10 kpc to ~ 170 km s^{-1} at 50 kpc. Assuming a halo profile following the Navarro-Frenk-White (NFW) [27] form (see Eq. 1.10), the mass enclosed within 60 kpc, constrained quite directly by the data, is found to be $M(< 60\text{kpc}) \sim 4.0{\cdot}10^{11} M_\odot$. Applying the virial theorem, one can estimate the virial mass $M_{vir} = \frac{4\pi}{3}\Delta_{vir}\Omega_m\rho_c r_{vir}^3 = 0.8{-}0.9{\cdot}10^{12} M_\odot$ (with $\Delta_{vir} \simeq 340$ being the virial overdensity [28]), the virial radius is $r_{vir} \sim 260$ kpc and the concentration parameter $c = r_{vir}/r_{-2} \sim 12$ (with r_{-2} being the radius at which the effective logarithmic slope of the profile is -2).

The issue related to the presence of sub-halos in the Galaxy is controversial. We postpone the discussion to Sec. 1.3.2.

1.2 Dark matter or modified gravity?

The first clear and incontestable evidence for a discrepancy between the measured mass and gravitational acceleration was pointed out on galactic scales [4, 5]. The orbital speed of stars v_r provides an estimation for the mass interior to r in spiral galaxies, as we have already seen in Eq. 1.1. During the 80's a lot of data on spirals with increasing precision pointed towards a gravitational anomaly. The debate on the two possible solutions, namely a modification of the Newtonian dynamics and the prediction of an invisible halo of matter, had initially focused on galactic scale. Subsequent compelling evidences for a mass discrepancy at cluster and cosmological scales, ask for updates and revisions of models with modified gravity. The debate, between supporters of DM and of modified gravity, started half of a century ago, is still going on. The number of proposed theories of gravity is very large. I will mention a few examples.

1.2.1 MOND

In the regime of strong gravitational fields or large velocities, Newtonian gravitation shows many drawbacks. In fact, it is usually considered as an approximation of a more fundamental theory, known as general relativity (see Section 1.2.3 for a class of modification of GR). In galaxies, the speeds are low compared to the light speed, and the gravitational fields are weak, thus in a regime where GR tends to the Newtonian limit. Alternatives to the DM paradigm are thus mere modifications of Newtonian dynamics, in the regime of acceleration below a certain value.

Concrete attempts for construction of such kind of theories have been put forward since few decades. Most of them regarded gravitation as a linear interaction, with the strength of the field proportional to its source mass. They turned out to be incompatible with the Tully-Fisher (TF) relation. The rotation velocity and the blue band luminosity of a galaxy are highly correlated. The TF law states that, for disk galaxies, the luminosity in the near infrared band, a good tracer of stellar mass, is proportional to the fourth power of the rotation velocity in the flat part of the RC, with a universal proportionality constant. It turns out that any linear gravity, even if non-Newtonian, is incompatible with the TF law (without invoking DM) [29].

In 1983, Milgrom [30] proposed a modification of Newtonian dynamics (MOND) with a non-linear character of gravity already at the non-relativistic level. Since the mentioned mass discrepancies are observed when the centripetal acceleration of stars and gas clouds in the outer part of spiral galaxies falls below a fix value, Milgrom's proposal states that gravity does not follow the prediction of Newtonian dynamics for acceleration smaller than a certain value a_0 (now fixed to $a_0 \simeq 1.2 \cdot 10^{-8}$ cm s^{-2}) and the Newtonian acceleration a_N is related to the acceleration of gravity a by:

$$a_N = a\,\mu(\frac{a}{a_0}) \quad . \tag{1.3}$$

The function $\mu(x)$ tends asymptotically to $\mu \to 1$ for $x \gg 1$, restoring Newtonian dynamics, and $\mu \to x$ for $x \ll 1$ in the deep MOND limit. The most popular choices for the μ function are $\mu(x) = x/(1+x)$ and $\mu(x) = x/\sqrt{1+x^2}$ (for a recent review on MOND see, e.g., [29] and references therein).

At large distances, the acceleration a becomes smaller than a_0 and Eq. 1.1 reads: $v(r) \simeq (a_0 G\,M)^{1/4}$, explaining simultaneously the TF relation and the flattening of RC (although the latter is a rough approximation of the real asymptotic behavior of RC, as mentioned above). With one additional parameter giving the mass-to-light ratio across the spiral disk, MOND hypothesis could be even more successful than DM paradigm in fitting spiral RCs for certain classes of galaxies. On galactic scales, including elliptical and dwarf spheroidal galaxies, MOND is in quite a good agreement with observations (for a review see, e.g., [31]). However, all these results rely on galaxies where the (smooth) disk contribution is, in any portion of the system, the dominant luminous component. A potential issue for MOND are galaxies where RCs should be driven by the gas component, which often appears to be highly irregular. The amplification of the related gravitational potential can hardly reproduce the smooth behavior of RCs.

From the observational point of view, the main drawback of MOND is on larger scales. Indeed, modification of Newtonian dynamics are not able to explain the mass discrepancy at cluster scale (see, e.g., Bullet cluster dynamics described in Sec. 1.1.2), where a relevant amount of DM remains

necessary. From the theoretical side, MOND is not completely satisfactory. It is not a fundamental theory, but rather an effective model, which describes the dynamics of accelerated object with an equation, but without any physical motivation. Moreover, the original MOND proposal needs a Lagrangian and relativistic formulation. A derivation from a Lagrangian can automatically overcome the issue of non-conservation of angular momentum and energy present in MOND. On top of theoretical motivations, a relativistic formulation could allow to deal with gravitational lensing, which is commonly regarded as supporting the need for DM. Note, moreover, that a non-covariant model forbids cosmological predictions.

TeVeS

The most popular relativistic formulation of MOND is the so called TeVeS [32], a tensor-vector-scalar theory of gravity. In this theory, a dynamical vector field U_μ and scalar field ϕ are introduced, and a relation between the gravitational metric $g_{\mu\nu}$ and the physical metric $\tilde{g}_{\mu\nu}$ is defined as:

$$\tilde{g}_{\mu\nu} = e^{-\phi/c^2} g_{\mu\nu} - \left(e^{\phi/c^2} - e^{-\phi/c^2}\right) U_\mu U_\nu \tag{1.4}$$

The conventional GR Einstein-Hilbert Lagrangian is used to give dynamics to $g_{\mu\nu}$, which then induce dynamics for $\tilde{g}_{\mu\nu}$. The matter Lagrangian is built exclusively with $\tilde{g}_{\mu\nu}$; this guarantees that the weak equivalence principle will be satisfied. The postulated actions for ϕ and U_μ are shown in Ref. [32] and involves the presence of three free parameters. For certain limits of the free parameters, TeVes reproduces standard GR and thus it usually considered as a viable approximation to standard gravity theory. In the non-relativistic limit TeVeS exactly predicts MOND equations. It also implies some deviations from GR, without violating the elementary post-Newtonian tests. Going into the details of the TeVeS formulation is beyond the scope of this brief review and, moreover, the theory is still under development. On the other hand, we have to mention that it solves the momentum conservation problems of MOND and alleviates the mismatch with observations based on gravitational lensing of clusters. Moreover, it is the first MOND-like theory allowing to formulate cosmological models. Nevertheless, DM is still needed on cluster scale [33] (considering only standard neutrinos), and to explain the third peak of CMB data. Then, the introduction of ϕ and U_μ (and other free parameters) has to be embedded in a more fundamental theory, in order to be theoretically justified.

1.2.2 f(R) GRAVITY

In the contemporary literature, there are numerous proposal for modifying GR. They are mainly motivated by the puzzling evolution of the Universe,

which requires dark energy and dark matter. Strong efforts have been devoted to a class of theories, called $f(R)$ theories of gravity (for a recent review, see [34]). They are generalization of the Einstein-Hilbert action, considering a generic function of the Ricci scalar R, instead of R itself:

$$S = \frac{1}{16\,\pi\,G}\int d^4x\sqrt{-g}\,f(R)\ . \tag{1.5}$$

Three versions of $f(R)$ gravity (metric, Palatini and metric-affine) have been explored, and features and constraints (given by, e.g., post-Newtonian limit and evolution of primordial perturbations) are model dependent. Most of the constructions of $f(R)$ gravity models try to address the dark energy issue at cosmological scales. Nevertheless, there are many attempts concentrating on galactic and cluster scales, with metric $f(R)$ gravity as a substitute for DM. The most investigated model is $f(R) = R^n$. However, n turns out to be related to the mass of each individual galaxy, implying a different n, namely a different form for $f(R)$, for each galaxy. This sounds implausible. Moreover, the best fit value for n obtained from RCs of galaxies contradicts other bounds [34]. Further developments in this field are needed in order to offer a reliable alternative to the DM paradigm.

1.3 Candidates

1.3.1 Baryonic dark matter

The amount of baryonic matter diffusely distributed as gas inter/intra clusters has been found compatible with the BBN estimates, as previously discussed. A dissipative form of matter would condense and cannot form extended halos in galaxies. For these reasons, the most plausible baryonic DM is in the form of massive astrophysical compact halo object (MACHO). They are macroscopic objects which do not produce a significant amount of observable radiation through astrophysical processes. The MACHO acronym originally referred to faint stars and stellar remnants (like, e.g., black holes, neutron stars, brown, white and red dwarfs).

In order to explain CMB anisotropies through the gravitational instability theory, the DM density perturbations have to start evolving at the time of matter-radiation equivalence, when the standard baryonic fluid, made of light elements, is still coupled to photons, and this implies that the dominant DM component cannot be in the form of standard thermally-produced baryons. Nevertheless, the most stringent constraint on the cosmological amount of baryonic DM comes from the BBN limit. Indeed, to reconcile with the observed abundance of light elements synthesized in the early Universe, one should state either the presence of non-baryonic DM or that baryons were hidden in some non-standard component at the time of BBN.

Among "exotic" candidates which could avoid the BBN bound, primordial black holes (PBH) are the most investigated case [35]. If they formed before BBN, they would not affect the light element abundances. In a radiation dominated epoch, the biggest mass for PBH (i.e., the mass of the entire horizon collapsing into a BH) can be estimated as: $M_{PBH} \simeq M_{\odot}(100\,\mathrm{MeV}/T)^2(10.75/g_*)^{1/2}$, where g_* are the degrees of freedom of the Universe. It cannot be neither too large ($M_{PBH} < 10^3 M_{\odot}$), since the BBN limit (T > MeV), nor too much small ($M_{PBH} > 10^{-16} M_{\odot}$), due to the limit on the Hawking radiation from diffuse gamma ray background data.

A useful technique for detecting MACHOs is the gravitational microlensing [36]. If a MACHO crosses the line-of-sight to a star, a magnification in the star brightness could be detected. The rate of gravitational microlensing of stars in the Small and Large Magellanic Clouds constrains the mass fraction of MACHOs in the Milky Way halo to be $< 20\%$, in case of masses between $6 \cdot 10^{-8} - 15\, M_{\odot}$ [37].

In [38], using very long baseline interferometry, they searched 300 compact radio sources for multiple imaging produced by gravitational lensing; a null result in the angular range expected for intergalactic supermassive compact objects with mass $10^6 - 10^8 M_{\odot}$, leads to $\Omega_{CO} < 0.01$ (95% C.L.) for such MACHOs.

In Ref. [39], by simulating the evolution of halo wide binaries in the presence of MACHOs, they estimated the upper limit on the mass fraction of MACHOs in the Milky Way halo with masses $\gtrsim 10^2 M_{\odot}$ to be $< 20\%$.

Comparing the distribution of high redshift type Ia SN brightnesses to the low redshift sample, in [40] they conclude that no more than 88% (95% C.L.) of the DM in the Universe can be in form of MACHO with mass greater than $10^2 M_{\odot}$.

The bottom line of these results is that, assuming Newtonian gravity, a significant amount of non-baryonic DM seems to be unavoidable.

1.3.2 Non-baryonic dark matter

Following standard requirements, a non-baryonic DM candidate has to be stable, neutral and weakly interacting.

In order to explain the estimated cosmological amount of DM (see Section 1.1.1), a viable DM candidate must have the correct relic density and a lifetime longer than the age of the Universe today, namely $\tau_{DM} \gtrsim 14 Gyr$. In DM model building, the latter constraint is often automatically satisfied, by mean of a symmetry preventing the DM decay.

It's not completely excluded that a tiny fraction of the whole DM content of the Universe can be made by electrically charged [41] or millicharged [42, 43] DM particles and that DM can possess electric or magnetic dipole moment [44]. Nevertheless, very strong constraints on all these possibilities are imposed by experimental data from, e.g., star cooling, distorsion of the CMB

energy spectrum, relativistic degrees of freedom at BBN, precision tests of SM and cosmic gamma-rays.

In principle, a DM candidate could also be colored. This possibility is severely restricted by the search for rare anomalous isotopes. Moreover, a class of DM candidates, called strongly interacting massive particles (SIMP), with interactions to ordinary matter significantly stronger than interactions mediated by weak force (but not $SU(3)_s$ charged), have been widely studied and can be constrained by many methods (e.g., direct searches, integrity of spiral galaxy disk, CMB distorsion, cosmic gamma-rays and Earth's heat flow). Both cases are excluded [45], unless considering exotic very massive ($m_{DM} \gtrsim 10^{20}$ GeV) candidates.

In the literature, there is a zoo of mechanisms for the production of the DM abundance in the Universe. The most famous one is the decoupling of thermal relics, that we are going to discuss more extensively. Out of equilibrium mechanisms will be mentioned when referring to specific examples.

Most of the constituents of the primordial Universe were in thermal equilibrium. Their phase space distribution function $f(p^\mu, x^\mu)$ obeys the Boltzmann equation:

$$\mathbf{L}[f] = \mathbf{C}[f] \quad , \tag{1.6}$$

where $\mathbf{L}$ is the Liouville operator, describing the time evolution of the phase space distribution function, and $\mathbf{C}$ is the collision operator, describing the dynamics of the system (in this case driven by annihilation processes). Considering an homogeneous and isotropic fluid, $f = f(E,t)$ and $\mathbf{L}$ highly simplifies. For the operator $\mathbf{C}$, we assume CP invariance and thermal equilibrium for all the species involved (other than DM). The DM species is stable (or very long-lived), thus the dominant processes for changing the number of DM particles are pair annihilations and inverse pair annihilations. In terms of number density of the DM species $n(E,t)$, Eq. 1.6 becomes:

$$\frac{dn}{dt} + 3\,H\,n = - < \sigma_a |v| > (n^2 - n_{eq}^2) \quad . \tag{1.7}$$

The left hand side (lhs) follows from the Liouville operator, with the second term describing the dilution associated to the expansion of the 3D space of the Universe. The right hand side (rhs) comes from the collision operator, with $< \sigma_a|v| >$ being the thermally averaged pair annihilation cross section times the relative velocity, and n_{eq} is the equilibrium number density. Clearly if the DM particle is at chemical equilibrium (i.e., $n = n_{eq}$), annihilation and creation have the same probability, and the number density will be not altered by interactions, but just diluted by the expansion. The equilibrium number density of a particle is obtained by integrating its distribution function; neglecting for simplicity the chemical potential, it takes the form:

$$n_{eq} = \int d^3p \, \frac{g}{(2\pi)^3} \frac{1}{e^{E/T} \pm 1} = \begin{cases} \frac{\zeta(3)}{\pi^3} g_{eff} T^3, & T \gg m \\ g \left(\frac{mT}{2\pi}\right)^{\frac{3}{2}} e^{-m/T}, & T \ll m \end{cases} \tag{1.8}$$

where g and m are, respectively, the degrees of freedom and the mass of the particle, $g_{eff} = g$ for bosons (- sign in the second member) and $g_{eff} = 3/4\, g$ for fermions (+ sign in the second member).

Defining $x = m_{DM}/T$ and the number density per comoving volume $Y = n/s$, with s being the entropy density ($s \propto a^{-3} \sim T^3$, i.e., adiabatic evolution), and considering a radiation dominated epoch (see Sec. 2.2), Eq. 1.7 recasts into:

$$\frac{dY}{dx} = -\frac{x\, s}{H(m_{DM})} < \sigma_a |v| > (Y^2 - Y_{eq}^2) \quad . \tag{1.9}$$

For a relativistic species $Y_{eq} = const$, since temperature provides enough energy for both pairs annihilation and creation. A non-relativistic particle, on the other hand, decreases with a Boltzmann dump $Y_{eq} \propto e^{-x}$, since annihilations have much more probability to happen with respect to creations of DM particles from lighter states, being the energy of the latters (i.e. the temperature of the bath) much smaller than the DM mass. As the temperature decreases, the mean path length for annihilation becomes larger and larger, and when it is roughly comparable to the size of the Universe, annihilations and creations stop. At this stage, the DM species freezes-out from the thermal bath and remains as a relic. If such process occurs at $x_f \gg 1$ (i.e., for a relativistic species), it is insensitive on the details of freeze-out ($Y(x = x_f)$ depends on x_f just through the temperature dependence of the thermal bath degrees of freedom) and the DM density today is $Y_o = Y_{eq}$. In the opposite case, $x_f \ll 1$ (i.e., for a non-relativistic species), the solution of Eq. 1.9 at x_f is not straightforward (we will come back to it in Sec. 2.3).

Hot dark matter

The adjective "hot" refers to the class of DM candidates being relativistic at the time when galaxy structures could start to form, namely, at redshift $z \sim 10^6$, when the cosmic horizon encompassed the mass of a large galaxy. Assuming a hot dark matter (HDM) with mass $\sim$ eV, the first scales to collapse would correspond to the mass inside the cosmic horizon when the temperature drops to eV and DM particles become non-relativistic. Indeed, a collisionless species tends to erase fluctuation below its free-streaming length, which for hot thermal relic is $\lambda_{FS} = 600 \frac{1\, eV}{m_{DM}}$ Mpc. For $m_{DM} \sim 1$ eV, this size turns out to be of the order of the largest cosmic structures, i.e., superclusters. HDM paradigm leads to a top-down hierarchy in structure formation. Therefore, galaxies and clusters would form through a process of fragmentation.

In the late 70's, when the evidence for DM in galaxies became compelling, HDM candidates were the most investigated explanation for DM. The fact that galaxies are much older than superclusters, contrary to HDM predictions, however, disfavoured this scenario in favour of CDM. Structure formation is commonly conceived to begin by small adiabatic fluctuations

in density in the initial conditions, that then grow by gravitational instability. Other mechanisms for the generation of such fluctuations, like e.g., cosmic defects, could in principle restore the HDM paradigm, but they are inconsistent with CMB observations.

Today, the question is how much HDM is allowed by cosmological data. The analysis performed by the WMAP team on data from CMB surveys, combined with distance measurements from SN and observations of BAOs in the distribution of galaxies, leads to: $\Omega_{HDM}h^2 < 0.007$ [10].

Cold dark matter

The ΛCDM scenario is a much more successful picture for structure formation. In this context, cold means that the DM candidates have negligible velocity well before matter-radiation equivalence (i.e., during the epoch at which matter density perturbations can start growing) and small-scale structure can form. As already mentioned, the standard picture for structure formation requires amplification of quantum fluctuations of an inflaton field producing a nearly scale-invariant power spectrum of adiabatic Gaussian density perturbations. This agrees well with the inferred matter power spectrum in the linear to mildly nonlinear regime of cosmological structure formation (and with models of the nonlinear clustering of galaxies) . Within this framework, ΛCDM leads to a bottom-up hierarchy and erases structure only on very small scales. For example, the neutralino in supersymmetry (SUSY) (see Section 2.5) has a small but non-zero velocity dispersion, and damps structures below Earth mass scales.

The ΛCDM model is a very successful model, in particular on large scale. As described in Sec. 1.1.1, it is in an amazing concordance with the inferred cosmological parameters, which are derived putting together cosmological (i.e., CMB, SN and Hubble parameter) and LSS measurements. It is consistent with the power spectrum from Lyα forest. N-body simulations predict the correct abundances of clusters nearby and at $z \gtrsim 1$.

The bottom-up approach explains the cluster formation and why most stars are in galaxies like the Milky Way. Indeed smaller galaxies merge to form larger structures; however, gas takes too long to cool and to form very big galaxies, and, indeed, the largest structures in the Universe are not such putative galaxies, but rather groups and clusters.

The spatial distribution of galaxies both on large and small scale agrees with ΛCDM N-body simulations. Note that it was considered an issue for the CDM paradigm, before developing simulations of sufficiently high resolution to identify the DM halos.

Despite of the mentioned great successes, the consensus on the ΛCDM model among the cosmological community is not uniform. This fact is driven by the appearance of some potential problems.

N-body simulations predict configurations with very large overdensities,

consistent with singular density halo profiles [27, 46, 47] and a universal spherical profile for virialized DM halos, which can be parametrized as:

$$\rho(r) = \frac{\rho_0 (r_h/r)^\gamma}{(1+(r/r_h)^\alpha)^{(\beta-\gamma)/\alpha}} \ , \tag{1.10}$$

where ρ_0 is the profile normalization and r_h is the scale length. The prototype of CDM profile is the so-called NFW profile [27], where $\gamma = 1$, $\alpha = 1$, $\beta = 3$. It implies a cuspy behaviour in the innermost region. In ΛCDM simulations, a correlation between ρ_0 and r_h is generally obtained. In the simulation leading to the NFW profile, the effect of baryons was not considered. Their role in the formation of DM halos is still under debate. In the case of galaxies like the Milky Way, an adiabatic compression on the DM distribution of the stellar component leads to a steepening of the halo profile from $\rho \propto r^{-1}$ into $\rho \propto r^{-1.5}$ [48]; such a steepening and ignoring a back–reaction on the DM profile tout–court stands as a limiting case among the series of results that have been obtained for the back–reaction effect in the literature, starting from different assumptions and using either analytic treatments or numerical simulations [48, 49, 50]. Although, the simulations lack resolution to map the distribution of DM on the very small scales, the extrapolation of the cuspy profile of Eq. 1.10 generates some tensions between the simulation results and observations.

Observations of RCs and velocity dispersions in LSB seem to indicate the presence of a central density core in DM distributions [51, 21]. In spirals, this evidence seems to be statistically quite compelling. Indeed, cuspy profiles can poorly fit the RCs of the selected sample of galaxies in [51]. The goodness of the fit is given by the ability in reproducing the RC and by the consistency of best fit parameters with constraints. The DM halo is usually described by two parameters: the halo mass M_h and the concentration parameter c (or equivalently by the profile normalization ρ_0 and the halo scale length r_h). The first is bounded by gravitational lensing observation to be $M_h < 10^{13} M_\odot$ and the latter is constrained in the range $c \sim 8 - 14$ by CDM simulations. RCs of spiral galaxies are fitted in a satisfactory way by cored halo profiles, with the core radius comparable to the optical radius [51]. On the other hand, NFW profiles are not excluded, in particular considering specific models for single galaxies (as did, e.g., in [48] for the Milky Way and M31). Being more conservative, we can furthemore restrict the conflict on the smallest scale at which RCs are observed, namely, several hundreds of pc. The presence of a cusp or a core in the innermost region cannot be probed neither by observations nor by simulations.

In Ref. [21], they fitted velocity dispersion of the Milky Way dwarf satellites using Eq. 1.2 and assuming isotropic velocity dispersion (i.e., $\beta = 0$). They conclude that DM forms cored mass distributions, with a core scale length of about 100 pc. However, a degeneracy between the core radius of

the DM halo and the model for β is present. Firm conclusions require an evidence for the latter.

Partially related to the central cusp issue, numerical simulations in the ΛCDM scenario lead to the so called "angular momentum problem" of disk galaxy formation [52]. It is commonly believed that the galactic disks form in the potential wells of DM halos as the baryonic component cools and collapses dissipatively. The disk is expected to possess the observed amount of angular momentum only if the infalling gas retain most of its original angular momentum. When only cooling processes are included, a very dense core, however, would cause baryonic cooling to be too efficient and the infalling gas loses too much angular momentum (by over an order of magnitude). The resulting disks are consequently much smaller than required by the observations.

N-body simulations in the ΛCDM scenario predict DM halos which are not spherical, but approximate triaxial ellipsoids. with a prolate form. In the case of the Galaxy, however, there are hints for a close-to-spherical halo [53].

According to the hierarchical clustering scenario, galaxies are assembled by merging and accretion of numerous satellites of different sizes and masses. Not all of the accreted satellites are destroyed in this process. The ΛCDM model predicts that massive galaxies such as the Milky Way and the M31 should be surrounded by large numbers of DM dominated subhalos, and they should be massive enough to form stars. The predicted amount of these satellites is roughly one order of magnitude more than the ~ 20 luminous dwarfs observed around each galaxy. This is known as the "missing satellite problem" [54, 55, 56].

Moreover, although it has been not quantitatively estimated, the distribution of dwarf galaxies seems more strongly correlated with bright galaxies than in ΛCDM numerical simulations [57]. Indeed, since the smaller halos formed earlier and should not be strongly correlated with later forming, they should fill both the voids and massive structures alike. It is hard to see why inhibition of star formation in dwarf halos would act preferentially in the voids.

Another apparent contradiction is the "anti-hierarchical galaxy formation". Recent observations have pointed out an apparent absence of cooling flows at the centres of rich clusters, a high number of old and red massive galaxies and the presence of much of the stellar mass of bright galaxies at $z > 1$. It could be an issue for hierarchical clustering since massive halos are assembled late according to CDM cosmology. However, it has been shown that this apparent "down-sizing" in the formation is not in contradiction with the hierarchical paradigm [58]. Moreover, considering new models of galaxy formation, which take into account, e.g., AGN feedback [59], the hierarchical CDM model provides a very good match to these observations.

As a general remark, we note that all these sketched issues are problems of numerical simulations, which are supposed to represent the physical picture.

However, this link is not straightforward. Indeed, pure N-body simulations are accurate solution to an idealized picture (e.g., "few" DM particles with mass larger than $10^3\,M_\odot$) and hydrodynamical simulations (which lose the particle nature of DM) are only approximate solution to a slightly more realistic description.

On the physical side, solutions for the small-scale problems of ΛCDM can involve either an astrophysical or a cosmological approach.

Indeed, for any of the mentioned issues, astrophysical ways out have been proposed, referring to astrophysical feedback, major mergers, gas bulk motions, mechanisms for quenching gas accretion and star formation in small halos, etc. (see the overview of these processes in, e.g., [60, 61]).

For example, turbulence driven by stellar feedback during galaxy formation offers a possible solution to the central cusp/core issue [62]. It leads to formation of massive clumps of gas which erase the central cusp for the first DM halos. This picture seems to be consistent with all kinematic observations.

The missing satellite problem can be solved if the Universe reionises shortly after the formation of proto-galaxies and globular clusters (at redshift $z \sim 12$) suppressing further formation of cosmic structure until later epochs [63]. This leads to low efficiency for gas cooling and star formation which in turn decreases the number of luminous satellite in the Galaxy.

The ΛCDM problems can also be faced by suppressing the matter power spectrum on small scales, namely, by considering different DM particles. One attempt led to self-interacting DM (SIDM), namely, to CDM with a large self scattering cross section. In this picture, both the central cusp and subhalos can be destroyed by DM interactions. However strong indication for a collisionless component comes from the analysis of the Bullett cluster [18] described above and from indirect searches [64], which severely constrain SIDM candidates. A different scenario is represented by warm dark matter (WDM) and will be discussed in the next Section.

The issues on large scales are much less worrying. We just mention an evidence for a possible mismatch in the number of superclusters between SDSS data and prediction from ΛCDM simulations [65].

Warm dark matter

In order to alleviate problems of CDM paradigm on small scales, warm dark matter (WDM) has been proposed. The term "warm" label DM candidates with velocity dispersion and free streaming length standing in between CDM and HDM. For this reason, fluctuations on small scales are suppressed, reducing the formation of small structures (roughly smaller than ~ 1 Mpc, i.e. the galaxy scale).

The Lyα observations are a powerful tool for constraining the mass of a WDM particle since they probe the matter power spectrum over a large

range of redshifts (z = 2 - 6), down to small scales ($1 - 80h^{-1}Mpc$). CMB and large scale structure data, on the other hand, can be exploited for this purpose as well, but they are much less constraining since the free-streaming effect of WDM particles is mainly visible on the scales probed by the Lyα power spectrum.

Sterile neutrinos, produced by oscillations of thermal active neutrinos, were among the prime candidates for HDM (see next Section). The limit on WDM posed by structure formation are often expressed in term of its mass. The relation between the masses of a generic thermal WDM and an oscillation-produced sterile neutrino, leading to the same power spectrum, is given by:

$$m_s = 4.43\, keV \left(\frac{m_{WDM}}{1\,\mathrm{keV}}\right)^{4/3} \left(\frac{0.25\,h^2}{\Omega_{WDM}}\right)^{1/3} \quad . \tag{1.11}$$

There are several attempts estimating the lower limit on m_s from Lyα data [66, 67, 68]. Latest results [69] give: $m_s \gtrsim 28$ keV (2σ), i.e., $m_{WDM} \gtrsim 4$ keV. In general, we should say that the allowed window for mass and couplings for WDM is becoming smaller and smaller (see the next Section for quantitative upper limits on m_{WDM} in the cases of the most popular WDM candidates).

Examples

In the following, we sketch some examples of non-baryonic DM candidates.

- **Neutrino**: It is now established that neutrinos have mass, and thus their thermal relic populations, at late times, after becoming non-relativistic, contribute to the DM content of the Universe. Weak interactions maintains SM neutrinos at equilibrium until MeV scale. Tritium β-decay experiments fixed an upper limit on one neutrino mass eigenvalue: $m_\nu < 2$ eV [70]. The mass splitting among the three mass eigenstate is very small, as derived from solar ($\Delta m^2_{21} \simeq 8{\cdot}10^{-5}$ eV^2) and atmospheric ($\Delta m^2_{32} \simeq 1.9 - 3 \cdot 10^{-3}$ eV^2) oscillation experiments [70]. Therefore, neutrinos decouple in the relativistic regime and their relic density is given by:

$$\Omega_\nu h^2 = \sum_{i=1}^{n_\nu} \frac{m_{\nu_i}}{93\, eV} \quad , \tag{1.12}$$

  where $n_\nu = 3$ [70]. These facts imply $\Omega_\nu h^2 < 0.07$, and thus SM neutrinos cannot be the dominant component of non-baryonic DM. Moreover being HDM, the neutrino component Ω_ν is severely constrained by LSS studies, which, through Eq. 1.12, lead to $\sum m_\nu < 0.66$ eV (95% C.L.) [10]. Another argument against neutrinos as the dominant component of non-baryonic DM is the fact that the required phase space density at the center of galaxies would violate Pauli exclusion principle [71].

- **WIMP**: Weakly interacting massive particles (WIMPs) are a class of stable and cold thermal relics with mass close to the electro-weak scale. They are the main subject of this thesis and the WIMP hypothesis will be more careful analyzed in the next Sections.

- **SuperWIMP**: Superweakly-interacting massive particles [72] have very tiny interactions and they were out of thermal equilibrium in the primordial Universe. However, their relic density could naturally match the observed CDM abundance, since they are produced through late decays of metastable WIMPs (or, more generally, of thermally produced massive particles), which are the next-to-lightest particle (NLP). The ratio between the two relic densities simply scales with the mass ratio: $\Omega_{DM} = m_{DM}/M_{NLP}\,\Omega_{NLP}$. Weak-scale gravitinos in supergravity and the first excitation of the graviton in Universal Extra-Dimension models (UED) could be SuperWIMP candidates. They cannot be detected in DM experiments. However, some indications can be derived by observable consequences in BBN and CMB (depending on the epoch of decay), or by missing energy in collider searches. In this context, a solution of small-scale problems of CDM can be achieved, if the DM particles are produced as WDM, namely, with kinetic energies much larger than those of the decaying metastable WIMPs [73]. However, a certain amount of fine-tuning seems intrinsic in scenarios of this kind.

- **Axion**: The QCD Lagrangian violates CP, T, and P due to non-perturbative effects:

$$\mathcal{L}_{np} = \theta \frac{g^2}{32\,\pi^2} G^{a\mu\nu} \tilde{G}^a_{\mu\nu} \ , \tag{1.13}$$

  where $G^{a\mu\nu}$ ($\tilde{G}^a_{\mu\nu}$) is the gluon (dual) field strength tensor, and θ is an arbitrary phase. This leads to a neutron electric dipole moment $d_n \simeq 5 \cdot 10^{-16}\theta$ e cm, constraining θ to be smaller than $3 \cdot 10^{-10}$ in order to not violate the experimental bound. A way to explain such a very small value is to promote θ to be a dynamical variable. The most interesting construction consists in considering it as a pseudo Nambu-Goldstone boson field of a spontaneously broken global U(1) symmetry, introduced by Peccei and Quinn (PQ) [74]. This is the axion and its interaction Lagrangian is given by:

$$\mathcal{L}_{int} = \frac{g^2}{32\,\pi^2} \frac{a}{f_a} G^{a\mu\nu} \tilde{G}^a_{\mu\nu} \ , \tag{1.14}$$

  where a is the axion field and f_a is the PQ scale, related to the axion mass by (neglecting non-QCD effects): $m_a = 6 \cdot 10^{-4} eV\,(10^{10} GeV/f_a)$ Thermal axions are excluded to be a significant component of non-baryonic DM. More interesting production mechanisms include misalignment and axionic string decay. In the first, at the QCD epoch,

the axion field rolls towards its minimum, and starts to coherently oscillate, producing a condensate of axions at rest, i.e. a CDM candidate. In the second scenario, axions would be produced by the decay of topological defects like axion-strings.

The main upper limit to the axion mass is given by "energy-loss argument" in stars. Indeed the properties of stars would change if they emit too much energy in form of axion by nuclear reactions or by thermal processes in the stellar interior. In particular, the duration of the SN 1987a neutrino pulse constrains m_a to be $< 10^{-2}$ eV (for a recent review on axions, see, e.g., [75, 76]). In order to not overclose the Universe, $m_a > 10^{-6}$ eV, and values close to this bound make the axion to be a significant fraction of CDM. However, due to the uncertainties in the calculation of the production, this has to be considered as an order of magnitude estimate. Most of the models predict a coupling between axions and photons. They could be tested by future Axion Dark Matter eXperiment, which will search for Galactic DM axions on Earth in the mass range $m_a = 10^{-6} - 10^{-4}$ eV, by stimulating their conversion to microwave photons in an electromagnetic cavity permeated by a magnetic field.

- **Warm Dark Matter candidates**: The most investigated cases of WDM are the gravitino and the sterile neutrino.

  Stable gravitino in SUSY scenario with R-parity conservation, like gauge mediated SUSY, could account for the DM density in the Universe, providing that the masses of some of the superparticles are sufficiently small, $M < 350$ GeV [77]. This means that the gravitino WDM scenario will be either ruled out or supported by the LHC experiments. Note that WDM gravitinos (mass in the range 1-15 keV) are much lighter than the previously mentioned SuperWIMP gravitinos.

  The sterile neutrino can behave as WDM [78], with masses in the range $\sim 0.1 - 100$ keV. It could explain the pulsar velocity kick through an anisotropic emission of sterile neutrinos[4], help in reionizing the Universe at high redshift, and emerge from many particle physics models (for a recent review, see, e.g., [79]). The case of sterile neutrinos created in a non-resonant production mechanism without lepton asymmetry, namely through oscillations of thermal active neutrinos, is ruled out [66, 67, 68]. Indeed, the same mixing mechanism leading to their production in the early Universe leads to radiative decays. Combining

[4] Differently with respect to the case of active neutrinos, the sterile neutrinos are emitted from the supernova with an asymmetry equal to their production asymmetry. The anisotropy of this emission can result in a recoil velocity of the neutron star remnants, and can explain the pulsar kicks issue, namely the fact that the many of these neutron stars move much faster than their progenitor stars.

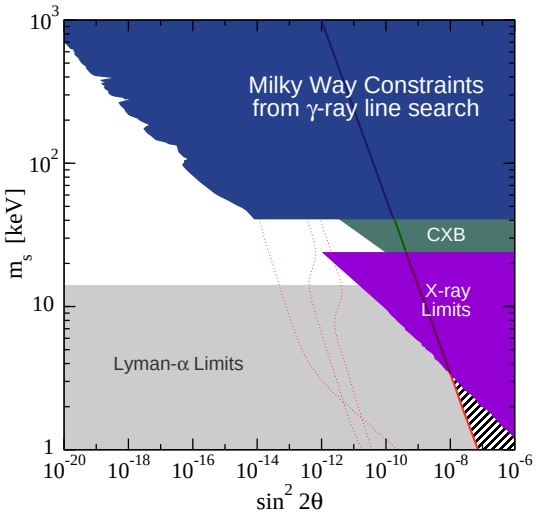

Figure 1.3: Parameter space of the sterile neutrino DM, in terms of the mass m_s and the mixing parameter $sin^2 2\theta$. Shaded regions are excluded. Figure taken from [82].

the upper mass limit from X-ray data (i.e., the cosmic X-ray background [80] and fluxes from the Coma cluster and from the Andromeda galaxy halo [81]) with the lower mass limit from the Lyα forest, only non thermal production mechanisms (like, e.g., resonant oscillations with lepton number violation or coupling with the inflaton) turns out to be allowed. Limits on the sterile neutrino are shown in Fig. 1.3, taken from [82].

- **Decaying DM**: As we have already mentioned, the minimal requirement for the lifetime of a viable DM candidate (i.e., with a cosmological density matching the observed DM abundance) is to be longer than the age of the Universe today. Examples of decaying DM candidates include gravitino in SUSY with broken R-parity [83] and sterile neutrino [80]. In contrast to self-annihilating (i.e., stable) relics, like WIMPs, they can decay into photons and neutrinos. Recently an intense 511 keV emission line due to electron/positron annihilation was detected by INTEGRAL [84] in the Galactic center direction. Among other astrophysical explanation, the decay of heavy DM into a species nearly degenerate ($\sim$ MeV) in mass could be invoked to fit the excess [85]. As a general remark, it's interesting to note that the rate at which decaying DM produce other species scales linearly with the density of DM, not with the square as in the WIMP scenario, with thus different implications for indirect searches.

- **Wimpzillas**: In order to not overclose the Universe, very heavy WIMP

candidates (Wimpzillas) have to be produced out of thermal equilibrium [86]. Their mass lies in the range $10^{12} - 10^{16}$ GeV (close to GUT scale) and several mechanisms of production have been proposed. Most of them (e.g., bubble collisions, amplification of quantum fluctuations at the end of inflation, reheating and preheating) are related with the inflationary phase of the Universe and the mass scale of inflation determines the Wimpzilla mass scale.

Chapter 2

Weakly Interacting Massive Particles

2.1 Standard model of particle physics

Proposed in 1967 by Weinberg [87], Salam and Glashow [88], the Standard Model of particle physics is an extremely successful theory. Many of its predictions have been tested with a very high precision, at energies below a few hundreds of GeV [70]. It describes electroweak (EW) and strong interactions (three of the four forces we believe to permeate the Universe) in terms of a gauge theory in four dimension. Its renormalizability was proved during the 70's by 't Hooft and Veltman [89]. A schematic picture of the fundamental constituents of the SM is shown in Fig. 2.1.

The gauge symmetry is $G_{SM} = SU(3)_s \times SU(2)_w \times U(1)_Y$, which is spontaneously broken at $E_{ssb} \sim 246$ GeV into $SU(3)_s \times U(1)_Q$, where electroweak generators are embedded in $SU(2)_w \times U(1)_Y$, $SU(3)_s$ describes strong interactions, and $U(1)_Q$ is the electromagnetic group.

The symmetry is broken by the VEV of a complex scalar field, named Higgs field, which gives mass also to fermions through Yukawa interactions.

The SM Higgs mechanism is only a description of Electroweak Symmetry Breaking (EWSB) and not an explanation of it since in particular there is no dynamics to explain the instability at the origin. The presence of a big desert between the E_{ssb} and the Planck scale (10^{19} GeV), namely the scale at which one would expect radiative corrections to the Higgs mass, is known as the gauge hierarchy problem. A better understanding of the mechanism of EWSB is one of the strongest motivations to consider models beyond the SM (BSM). The SM can be considered as an effective theory, valid in the low energy limit, and new physics is expected to take place at energy larger (and hopefully around) the weak scale. Essentially all theories BSM predict the existence of new massive particles at this scale; the hierarchy problem implies that the absence of new particles becomes less and less natural as we

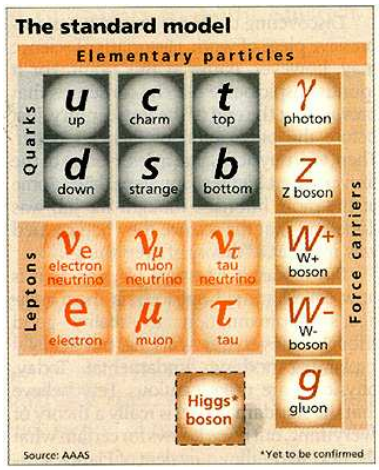

Figure 2.1: A schematic picture of the elementary particles of the SM.

explore higher and higher energy. Some of this extra states can be “dark", i.e. color and electromagnetic neutral, with the weak force (and gravity) as relevant coupling to ordinary matter.

It is indeed tempting to search for a framework embedding, at the same time, naturalness for EWSB and DM candidates with weak scale mass and interactions.

2.2 Standard model of cosmology

The cosmological scenario, on which most cosmologists agree, is described by the so called "Hot Big Bang" model. According to it, the Universe was very small and hot during its infancy, and its time-evolution is accomplished by space-expansion and cooling. It is a very successful model, giving trustable explanations for CMB, abundance of light elements, and LSS formation. On the other hand, in order to fully agree with observations, it requires a dramatically relevant amount of dark matter and dark energy, and a period of accelerated expansion in the past, know as inflation. Both of this three hypotheses have been not completely tested.

The two main pillars of the standard model of cosmology are the general relativity and the assumption of spatial isotropy and homogeneity (also called the "cosmological principle"). The Einstein equation reads:

$$R_{\mu\nu} - \frac{1}{2} g_{\mu\nu} R = -\frac{8\,\pi\,G}{c^4} T_{\mu\nu} + \lambda g_{\mu\nu} \quad , \tag{2.1}$$

where $g_{\mu\nu}$ is the metric tensor, $R_{\mu\nu}$ and R are the Ricci tensor and scalar, respectively, $T_{\mu\nu}$ is the stress-energy tensor, and λ is the cosmological constant.

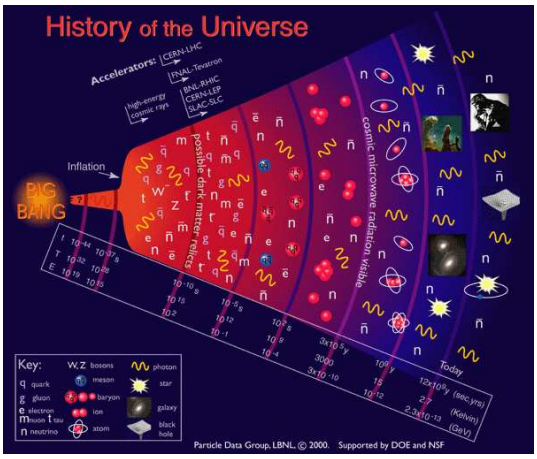

Figure 2.2: A sketch of the history of the Universe.

The l.h.s. relies on the geometry of the Universe and it is completely fixed by specifying the metric. Indeed, in GR, $R_{\mu\nu}$ and R are directly determined by $g_{\mu\nu}$ through the affine connection. The properties of isotropy and homogeneity are mainly motivated by CMB and LSS observations. This assumption implies that the 3D space is maximally symmetric, or in other word, that the geometry of the space can be described only by a S^3 sphere, an hyperplane, or an hyperboloid. For consistency with special relativity, the metric should have a Minkowskian signature. These requirements lead to the Lemaitre-Friedmann-Robertson-Walker metric, whose line element can be expressed as:

$$ds^2 = g_{\mu\nu}x^\mu x^\nu = -c^2dt^2 + a(t)^2\left(\frac{dr^2}{1-k\,r^2} + r^2 d\Omega^2\right) \quad , \qquad (2.2)$$

where $a(t)$ is the scale factor, related to the Hubble parameter through: $H(t) = \dot{a}(t)/a(t)$ and k is the curvature constant specifying the local geometry of the Universe. It can take the value $k = +1, 0, -1$, corresponding to the three allowed spaces.

The r.h.s. of Eq. 2.1 describes the content of the Universe, approximated as a fluid. Homogeneity and isotropy lead to the stress-energy tensor for a perfect fluid: $T_{\mu\nu} = diag(p, \rho, \rho, \rho)$, where $p(t)$ is the pressure and $\rho(t)$ is the total energy density of the Universe. They are connected by the equation of state: $p = \omega\rho$.

The cosmological principle highly simplify Eq. 2.1, which reduces to two independent algebraic equations. The first is the so-called Friedmann equation:

$$\Omega(t) - 1 = \frac{k}{H(t)^2 a(t)^2} \quad . \qquad (2.3)$$

Recall that $\Omega = \rho/\rho_c$; the meaning of ρ_c appears now evident. Indeed,

$\rho = \rho_c$, implies $k = 0$, i.e. a flat Universe, $\Omega < 1$ denotes a closed Universe ($k = -1$), and $\Omega > 1$ is associated to an open Universe ($k = 1$). Plugging in the conservation of the stress energy tensor and assuming ω =const, the evolution of the energy density, in a Universe dominated by one form of energy, is given by: $\rho \propto a^{-3\,(1+\omega)}$. In case of radiation domination ($\omega = 1/3$), $\rho \propto a^{-4}$, for matter domination ($\omega = 0$), $\rho \propto a^{-3}$, and for vacuum domination ($\omega = -1$), $\rho \propto$const. As follows from these scalings, the Universe was dominated by radiation during its infancy, then experiences a phase of matter domination and, at late times, the cosmological constant can take over.

The second independent equation is the Raychaudhuri equation:

$$q = \frac{\Omega}{2}(1 + 3\,\omega) \ , \tag{2.4}$$

where $q = -\frac{\ddot{a}}{a}H^{-2}$ is the deceleration parameter. An accelerated expansion implies $\omega < -1/3$ and cannot be determined neither by matter nor by radiation, while possibly by a cosmological constant.

2.2.1 Thermal history of Universe

An evolving Universe cannot be strictly considered in thermal equilibrium, but, actually, it has been very close to this condition during most of its history. The latter can be described as the evolution of a thermal bath in an expanding and cooling Universe, where each species leaves the equilibrium at a certain phase of the evolution. The departure happens roughly when the mean free path of the species becomes larger than the size of the Universe, i.e. $\Gamma \gtrsim H$, where $\Gamma = n < \sigma\, v >$ is the interaction rate. Phase transitions are another crucial effect in determining the evolution. In the following, we report a brief schematic summary of the thermal history of the Universe [90] (see also Fig. 2.2):

- Today$\sim$ 14 Gyr (10^{-4} eV): Measurement of the CMB radiation at 2.7 K.
- 10^5 yr (0.4 eV): Decoupling of matter and radiation. Relic photons form the CMB and the recombination of matter leads to formation of atoms.
- 10^4 yr (1 eV): Equivalence between matter and radiation. Structure formation starts.
- 1 min (1 MeV): Neutrino decoupling.
- $10^2 - 10^{-2}$ s (0.1-10 MeV): Big Bang Nucleosynthesis: formation of light elements.

- 10^{-5} s (0.3 GeV): QCD phase transition. Confinement of quarks and gluons lead to formation of baryons.
- 10^{-7} s (5 GeV):[1] WIMPs decoupling. DM relic abundance forms.
- 10^{-10} s (10^2 GeV): EW phase transition $G_{SM} = SU(3)_s \times SU(2)_w \times U(1)_Y \rightarrow SU(3)_s \times U(1)_Q$
- 10^{-36} s (10^{15} GeV):[1] Phase of inflation. An exponential expansion isotropizes and flattens the Universe.
- 10^{-43} s (10^{19} GeV): Planck epoch. Quantum corrections to GR become sizable and we would need a fully consistent physical theory linking quantum mechanics and gravity. This fact prevents an extrapolation beyond the Planck epoch.

The thermal history of the Universe has been tested accurately until the BBN epoch, as we discussed in the previous Chapter. The rest of the listed events are theoretical predictions of the standard cosmological model. Many other mechanisms (like, e.g., supersymmetry or GUT-symmetry breaking) could be included in the list and drive the evolution of the Universe during its infancy.

2.3 WIMP paradigm and Relic density

The DM is one of the open questions of the standard cosmological model. Theories beyond the SM typically predict new particle at the EW scale and WIMP candidates are a class of thermal CDM particles, with mass and couplings related to EW physics. Their stability is guaranteed by a discrete symmetry, which prevents the decay. WIMPs are very well motivated since they arise in a number of extensions of the SM, including, e.g., supersymmetry, UED and Little Higgs. WIMPs were in thermal equilibrium in the early Universe, with the comoving number density altered only by pair annihilations or inverse annihilations (see Eq. 1.9). Their decoupling is described in Sec. 1.3.2. As the Universe expands and cools down, the energy of particles in the thermal bath (i.e. the temperature) drops below the WIMPs production threshold (i.e. the WIMP mass). On the other hand, WIMP annihilations still take place and, consequently, the number density rapidly decreases, following the behaviour of Eq. 1.8 for a non-relativistic species. Then, when the annihilation rate becomes comparable to the expansion rate of the Universe, i.e., $\Gamma_a \sim H$, annihilations stop and WIMPs freeze out, remaining as relics. This can be seen writing the Boltzmann equation 1.9 in

[1] The epoch is model-dependent. We report a typical example.

the form:

$$\frac{x}{Y_{eq}}\frac{dY}{dx} = -\frac{\Gamma_a}{H(M_\chi)}\left(\frac{Y^2}{Y_{eq}^2} - 1\right) \quad , \tag{2.5}$$

where $\Gamma_a = n_{eq} < \sigma_a|v| >$ and M_χ is the WIMP mass (recall that $x = m_\chi/T$ and $Y = n/s$, with s being the entropy density and n the particle number density).

In the non-relativistic regime and far from resonances and thresholds, the thermally averaged cross section times velocity can be expanded, considering only s- and p-wave: $< \sigma_a|v| >= a + 6\,b/x + \mathcal{O}(x^{-2})$. The s-wave term is typically dominant for a boson or a Dirac fermion candidate, while the p-wave term becomes important in the case of Majorana fermions. In a radiation dominated Universe with adiabatic expansion, the freeze-out temperature can be derived by solving iteratively an approximate analytical form of the Eq. 1.9 during the decoupling [90]:

$$x_f \simeq \ln\left(\frac{5}{4}\sqrt{\frac{45}{8}}\frac{g}{2\pi^3}\frac{M_\chi\, m_P(a + 6\frac{b}{x_f})}{\sqrt{g_*(x_f)x_f}}\right) \quad , \tag{2.6}$$

where $m_P = G^{-1/2}$ is the Planck mass. The relic density today is $\rho_0 = m\,n_0 = m\,Y_0 s_0$. Inserting Eq. 2.6 to solve Eq. 1.9 after the decoupling, one can find:

$$\Omega_{DM}h^2 \simeq \frac{1.04\cdot 10^9}{m_P}\frac{x_f}{\sqrt{g_*(x_f)}}\frac{1}{a + 3\frac{b}{x_f}} \ , \tag{2.7}$$

Assuming a DM mass close to EW scale (i.e., $\sim$ 100 GeV), an annihilation cross section driven by weak interactions (i.e., $< \sigma_a|v| > \sim 3\cdot 10^{-26} cm^3 s^{-1}$) and the number of effective degrees of freedom of the SM (i.e., $g_* \sim 100$), the freeze-out parameter turns out to be $x_f \simeq 20 - 30$. Evaluating Eq. 2.7, $\Omega_\chi h^2 \sim 0.1$, namely, the observed amount of DM in the Universe. Note that x_f depends only logarithmically on the parameters and moderate variations of the latters do not affect the result; g_* enters with a power 1/2 in Eq. 2.7 and, thus, the key assumptions driving the result are the weak annihilation cross section and mass. This simple calculation shows that extensions to the SM of particle physics can offer a suitable DM candidate. This motivated a huge effort in developing a detailed analysis of the WIMP paradigm.

An intuitive and model-independent argument provides an order of magnitude estimate for the upper limit of the WIMP mass. Indeed, the unitarity bound implies $< \sigma_a|v| > \lesssim 10^{-22}\mathrm{cm}^3\mathrm{s}^{-1}\,(1\,\mathrm{TeV}/M_\chi)^2$ [91]. The upper limit for $\Omega_{DM}h^2$ is inferred from WMAP data and Eq. 2.7 leads to $M_\chi \leq 120$ TeV.

Note that the earliest constraints derived so far on the thermal history of the Universe, rely on the BBN epoch. Some non-standard pictures, like, e.g., entropy production due to a phase transition, taking place before the BBN, could actually dilute (or enhance) the density of WIMPs computed in Eq. 2.7.

2.3.1 Including coannihilation

In presence of particles nearly degenerate in mass with the DM particle, but slightly heavier, the calculation shown above can be incomplete. Indeed, in the case of mass splittings of the order of the bath temperature, these particles are thermally accessible by the DM. If the DM particle can be turned into these species and viceversa by inelastic scatterings over background particles (note that these interactions tend to be much faster than pair annihilation processes because they are triggered by relativistic background states), the annihilations of the nearly degenerate states will play an important role in determining the DM relic density. This phenomenon is called coannihilation [92]. It involves a set of coupled Boltzmann equations [93, 92, 94], describing simultaneously the density evolution of coannihilating particles. Noting that the DM density is $n = \sum_{i=1}^{N} n_i$ (i.e., the heavier particles decay into the DM candidate after the freeze-out), with N being the number of particles i involved in the coannihilaton, a Boltzmann equation for n can be restored:

$$\frac{dn}{dt} = -3Hn - < \sigma_{eff} v > (n^2 - n_{eq}^2) \ , \tag{2.8}$$

with

$$\begin{aligned} \sigma_{eff}(x) &= \sum_{ij}^{N} \sigma_{ij} \frac{g_i g_j}{g_{eff}^2} (1+\Delta_i)^{3/2} (1+\Delta_j)^{3/2} e^{-x(\Delta_i+\Delta_j)} \ , \\ g_{eff}(x) &= \sum_{i=1}^{N} g_i (1+\Delta_i)^{3/2} e^{-x\Delta_i} \ , \ \Delta_i = \frac{m_i - M_\chi}{M_\chi} \ , \end{aligned} \tag{2.9}$$

where g_i and m_i are the number of internal degrees of freedom and the mass for the species i, respectively, and σ_{ij} is the cross sections for processes $\chi_i \chi_j \rightarrow$ bath states. Since, in the thermal environment, coannihilating states are essentially indistinguishable, particles with a great number of degrees of freedom can highly affect the relic density computation. As mentioned before, the mass splitting is the key quantity for a particle to be thermally accessible by DM. The relevance of a species i in the coannihilation process is driven by the exponential dump involving Δ_i. A solution for Eq. 2.8 can be derived in a similar way as without coannihilation. In the non-relativistic regime, $< \sigma_{eff}\, v >= a_{eff}(x) + 6\, b_{eff}(x)/x + \mathcal{O}(x^{-2})$ with:

$$\begin{aligned} a_{eff}(x) &= \sum_{ij}^{N} a_{ij} \frac{g_i g_j}{g_{eff}^2} (1+\Delta_i)^{3/2} (1+\Delta_j)^{3/2} e^{-x(\Delta_i+\Delta_j)} \ , \\ b_{eff}(x) &= \sum_{ij}^{N} b_{ij} \frac{g_i g_j}{g_{eff}^2} (1+\Delta_i)^{3/2} (1+\Delta_j)^{3/2} e^{-x(\Delta_i+\Delta_j)} \ , \end{aligned} \tag{2.10}$$

where a_{ij} and b_{ij} follow from the expansion of σ_{ij}. Note that if the annihilation rate per degree of freedom of the coannihilating particles is larger

(smaller) than for the DM candidate, coannihilations tend to increase (decrease) the effective cross section, and hence to diminish (enhance) the DM relic density. Eqs. 2.6 and 2.7 recast into:

$$\begin{aligned} x_f = & \ln \left(c(c+2)\sqrt{\frac{45}{8}} \frac{g_{eff}(x_f)}{2\pi^3} \frac{M_\chi M_{Pl}(a_{eff}(x_f) + 6b_{eff}(x_f)/x_f)}{\sqrt{g_*(x_f)x_f}} \right) \\ \Omega_{DM}h^2 \simeq & \frac{1.04 \times 10^9}{M_{Pl}} \frac{x_f}{\sqrt{g_*(x_f)}} \frac{1}{I_a + 3I_b/x_f} , \end{aligned} \tag{2.11}$$

where $I_a = x_f \int_{x_f}^{\infty} a_{eff}(x)x^{-2}dx$ and $I_b = 2x_f^2 \int_{x_f}^{\infty} b_{eff}(x)x^{-3}dx$.

The Boltzmann equation can be solved in a more accurate way than the analytical procedure described above and, in the following, we sketch such a computation [94]. In the Maxwell-Boltzmann regime, the total equilibrium number density, $n_{\rm eq}$, can be written as:

$$n_{\rm eq} = \frac{T}{2\pi^2} \sum_i^N g_i m_i^2 \, K_2\Big(\frac{m_i}{T}\Big) . \tag{2.12}$$

The effective thermally-averaged annihilation cross section $\langle \sigma_{\rm eff} v \rangle$ drives the decoupling and reads:

$$\langle \sigma_{\rm eff} v \rangle = \frac{1}{n_{\rm eq}^2} \frac{g_1^2 T}{4\pi^4} \int_0^\infty dp_{\rm eff} p_{\rm eff}^2 \, K_1\left(\frac{\sqrt{s}}{T}\right) \, W_{\rm eff}\,(s) , \tag{2.13}$$

with all relevant pair-annihilation channels included in the effective annihilation rate:

$$W_{\rm eff}\,(s) = \sum_{ij} \sqrt{\frac{[s-(m_i-m_j)^2][s-(m_i+m_j)^2]}{s(s-4\,M_\chi^2)}} \frac{g_i g_j}{g_1^2} W_{ij} . \tag{2.14}$$

In the expressions above, $K_l(x)$ is the modified Bessel functions of the second kind of order l; $i = 1$ refers to the lightest state. For all pair annihilation processes the kinematics has been written in terms of $p_{\rm eff}$ and $s = 4(p_{\rm eff}^2 + M_\chi^2)$, the center-of-mass momentum and energy squared in the annihilation of a pair of lightest states; the annihilation process with given initial states i and j needs to be included in the effective annihilation rate whenever $s \geq (m_i + m_j)^2$.

Relic abundances can be then computed solving numerically the density evolution equation 2.8. In the techniques developed in [95] and implemented in the DarkSUSY package [96], the first step is to derive the expression for $W_{\rm eff}\,(s)$, taking care of resonances and coannihilation thresholds. The Boltzmann equation is then integrated numerically in the variable Y; thermal equilibrium $Y = Y_{\rm eq}$ is assumed as boundary condition at the temperature $T = M_\chi/2$, and the evolution is followed up to the point, after freeze-out,

when Y settles on a constant value. Contrary to most analyses in the literature, this computation of the relic density is not performed by replacing the thermally averaged annihilation cross–section with a truncated expansion in powers of T/M_χ; such a procedure gives a more accurate result, especially in case of coannihilation and resonance effects.

In some particular cases, non-perturbative corrections might significantly alter the relic density computation. The thermally averaged cross section is commonly estimated in the QFT perurbative approximation. On the other hand, (co-)annihilating particles are non-relativistic, and their annihilation cross sections can be affected by the formation of bound states [97] and by long-range Coulomb interactions [98, 99].

Let us consider this issue in a "standard" picture, where the WIMP stability is guaranteed by a discrete $\mathbf{Z}_2$ symmetry, under which all SM particles are neutral, while the DM candidate is the lightest non-neutral state. Bound states of two (co-)annihilating particles are $\mathbf{Z}_2$-even and, if meta-stable, can decay into SM particles. Therefore, this effect reduces the DM relic density. The key quantity for the formation of bound states is the ratio between the binding energy E_b and the temperature of the bath. Indeed, thermal fluctuations can destroy these bound states.

In QED, a distortion of a charged particle wave-function due to long-range Coulomb forces can occur in scattering processes, when the particle is non-relativistic and the electrostatic potential energy becomes relevant. This effect is called Sommerfeld effect [100]. Corrections to annihilation cross sections dominated by s-wave scattering, can be described by an effective parameter S:

$$S = \left| \frac{\psi(\infty)}{\psi(0)} \right|^2 = -\frac{\pm z}{1 - e^{\pm z}} \quad , \tag{2.15}$$

where ψ is the reduced s-wave-function for the two-body state, $\pm$ refer to repulsive or attractive force, respectively, and $z = \pi\alpha/v$, with α being the coupling constant and v being the velocity of the colliding particles. The perturbative cross section σ is then rescaled to $S\sigma$. From a QFT point of view, this effect can be reproduced by resumming an infinite class of Feynman diagram, which are not negligible for non-relativistic particles. The generalization of the Sommerfeld effect to cases mediated by non Abelian and massive gauge boson vectors, and with non-zero temperature, is performed in [98, 99].

The importance of this two non-perturbative corrections is highly model-dependent, and no general statement can be drawn. In the case of the DM candidate considered in Chapter 4, they turn out to play a subdominant role, as described in Section 4.3.4.

2.4 Kinetic decoupling

Freeze-out from (chemical) equilibrium means that the DM becomes a chemically distinct particle species and its comoving number density remains unchanged, namely, annihilations stop. However, WIMPs can interact with the thermal bath until later time through elastic scattering processes. As the Universe expands, the thermal equilibrium cannot be maintained, and the temperature of kinetic decoupling T_{kd} is roughly set by the condition: $\Gamma_{kd}/N_{coll} \sim H$. N_{coll} is the number of collisions between a light particle of the thermal bath and the WIMP to make the momentum of the latter comparable to the typical momentum for a thermally distributed species ($N_{coll} \sim M_\chi/T$). For a precise analytical determination of T_{kd}, see [101]. The coupling between the CDM and radiation washes out DM density perturbations for temperatures $T > T_{kd}$. Note that WIMPs can produce only adiabatic perturbations, since its abundance is driven by annihilation, implying the same chemical composition everywhere in the Universe[2]. After kinetic decoupling, the DM enters in the free streaming regime, where small-scale fluctuations are suppressed by collisionless damping. Matter density perturbations that grow nonlinear are characterized by masses above the free-streaming mass [101]:

$$M_{\rm fs} \simeq \left(\frac{1 + \ln\left(T_{\rm kd}/30\ {\rm MeV}\right)/19.2}{\left(M_\chi/100\ {\rm GeV}\right)^{1/2} \left(T_{\rm kd}/30\ {\rm MeV}\right)^{1/2}} \right)^3 10^{-6} M_\odot\ . \qquad (2.16)$$

Hence, typical WIMP models lead to a mass for the smallest protohalo comparable to the mass of the Earth. However, T_{kd} may range from tens of MeV to several GeV, depending on the model [102]. The kinetic decoupling provides the initial conditions for growing of perturbations and T_{kd} plays a crucial role in Eq. 2.16. The temperature T_{kd} does not critically affects only structure formation. Indeed, the presence of DM substructures can have detectable effects in direct and indirect DM detection.

2.5 Examples

In this Section, we briefly describe the most popular classes of WIMP DM candidates proposed in the literature. The next Sections will be devoted to potential WIMP signatures. They include WIMPs production at colliders, direct detection through WIMP scattering on targets in a detector, and indirect detection by mean of fluxes of particles produced by WIMP annihilations in astrophysical structures. For comprehensive reviews on WIMP DM candidates and their detection, see, e.g., [103, 104, 23])

[2]This prediction can be avoided in the case of WIMP≠antiWIMP, with an asymmetry between them.

- **Supersymmetry**: If R-parity is conserved, the lightest supersymmetric particle (LSP) is stable.

  In the minimal supersymmetric standard model (MSSM), the LSP is often a mixture of the superpartners of the photon, the Z and the two neutral CP-even Higgs bosons, called neutralino. This Majorana fermion is the most popular candidate for DM in the literature. Depending on the mixing parameters, it can have different behaviours in direct, indirect and collider searches (see, e.g., reviews of [23, 104, 103]).

  Sneutrinos are the scalar partners of neutrinos and in some fractions of the parameter space can be the LSPs. In the MSSM, they are marginally compatible with existing experimental bounds, provided their contribution to the DM density is subdominant. However, they could be a viable alternative to neutralinos in some extensions of the MSSM [105].

  The less appealing property of SUSY DM models is the large number of parameters.

- **Heavy neutrino**: The presence of heavy neutrinos with SM interactions is very constrained. A WIMP Dirac neutrino is ruled out as DM because of its large coupling to the Z. Indeed, it would scatter elastically off nuclei with a large cross section induced by the Z exchange and it should have been detected in direct experiments, unless its mass is larger than several tens of TeV. Moreover, Dirac or Majorana neutrinos with mass below the EW scale are excluded by EW precision tests. Recently, new limits on spin-dependent WIMP-nucleon cross-sections have led to the exclusion of heavy Majorana neutrinos up to mass of 2 TeV (again assuming SM weak interaction).

  In extension of the EW SM group to $SU(2)_L \times SU(2)_R \times U(1)$, a different type of Dirac neutrino coupled with the Z'-boson of the $SU(2)_R$ group, but with suppressed coupling to the Z-boson of $SU(2)_L$ could be a viable WIMP candidate [106].

- **Extra Dimensions**: Viable WIMPs can arise in frameworks with flat extra dimensions (e.g., UED [107] and the model presented in [108]) and in some warped geometries [109, 110, 111]. This class of DM candidates will be discussed in Chapter 4.

- **Little Higgs**: In Little Higgs models, the Higgs is a pseudo-Nambu-Goldstone boson, corresponding to a global symmetry spontaneously broken at a scale around 1 TeV. The divergences to the Higgs mass remain present only at two-loop level, and therefore the weak scale is stabilized up to the cutoff scale, $\sim$ 10 TeV. Above the cutoff scale, the model needs to be embedded in a more fundamental theory. The

introduction of a discrete symmetry, called T parity improves the consistency of Little Higgs models with EW precision data, and makes the lightest T-odd particle (LTP) stable. It is typically the T-odd heavy photon, which is weakly interacting and can play the role of DM (for a review, see [112]). The direct detection rates are quite low, while the picture for indirect searches can be more promising.

2.6 Detection

2.6.1 Direct detection

As highlighted in the first Chapter, the DM is not only a cosmological issue, but rather it is needed down to galactic scale. Therefore a significant WIMP population is expected in the Milky Way, including at our location. In the WIMP paradigm, the annihilation cross section is driven by weak interaction. By crossing symmetry, we can guess a weak interaction strength, also for the scattering cross section. The direct detection of WIMPs consists in looking for their interaction with ordinary matter on Earth, by recording the recoil energy of target atomic nuclei on which the WIMPs elastically scatter. Indeed, the most important direct detection process is elastic scattering on nuclei, although inelastic processes and scattering on electrons have also been suggested in the literature. The recoil energy of the nucleus in the laboratory frame is given by non-relativistic kinematics, $E_r = |\mathbf{q}|^2/2M_\chi$. where $|\mathbf{q}|^2 = 2\mu^2 v^2(1-\cos\theta)$ is the momentum transfer, θ is the scattering angle in the center-of-mass system, v is the WIMP-velocity relative to the target, $\mu \equiv m_N M_\chi/(m_N + M_\chi)$ is the reduced mass, and m_N is the nucleus mass. For typical nucleus mass and WIMP properties, the mean recoil energy deposited in a detector is $< E_r > \simeq 30$ keV. The event rate per unit mass in a detector with nuclear mass number A is $dR = N_A/A\,\sigma_{\chi N} v\,dn$, where $\sigma_{\chi N}$ is the cross section for the WIMP scattering on the nucleus and N_A is the Avogadro number. The differential WIMP density is taken in the form $dn = n_0 f(\mathbf{v}) d^3v$, where $n_0 = \rho_{DM}/M_\chi$ is the WIMP number density and f is the velocity distribution function. To fully determine $f(\mathbf{v})$, one should estimate the WIMP velocity with respect to the galactic frame, the relative motion of the observer on the Earth to the sun (i.e., the annual modulation), and the mean relative velocity of the sun relative to the Galactic center ($\sim$ 220 km/s). The differential scattering rate per unit recoil energy is given by:

$$\frac{dR}{dE_r} = \frac{N_A}{A}\frac{\rho_{DM}}{M_\chi}\int_{v_{min}}^{v_{max}} d^3v\, v\, f(\mathbf{v})\frac{d\sigma_{\chi N}}{dE_r} \quad , \tag{2.17}$$

where $v_{max} \simeq 544$ km/s is the local galactic escape velocity and $v_{min} = \sqrt{E_r M/(2\mu^2)}$ corresponds to $\theta = \pi$. WIMPs scatter on nuclei, which have a finite size. Therefore, the differential cross section can be expressed in

terms of the cross section at zero momentum transfer σ_0 times a nuclear form factor:

$$\frac{d\sigma_{\chi N}}{d|\mathbf{q}|^2} = \frac{\sigma_0}{4\mu^2 v^2} F^2(|\mathbf{q}|) \ . \tag{2.18}$$

The cross section σ_0 describes the effective WIMP interaction with nuclei, and can be derived by evaluating the matrix elements of the nucleon operators in a nuclear state. This in turn is determined by WIMP interactions with quarks (and gluons) evaluated in nucleon states. WIMP-nucleon scattering can occur through scalar and axial-vector (and vector, but highly constrained) interactions leading to a spin-dependent and a spin-independent terms, which rely on two different form factors. The spin-dependent contribution is usually sub-dominant with respect to the scalar interaction, since the latter can take place coherently with all the nucleons in the nuclei.

Predictions depend strongly on the DM local density and its velocity distribution. From RCs of the Milky Way, the local energy density is inferred to be $\rho_0 = 0.1 - 0.7$ GeV cm^{-3}, and the standard reference value is $\rho_0 = 0.3$ GeV cm^{-3}. The standard assumption for the the WIMP velocity distribution with respect to the galactic frame is an isothermal sphere with $v \sim 270$ km/s as the WIMP velocity dispersion. WIMP mass and cross section are commonly treated as free parameters, constrained by the experimental results.

The nuclear recoil produced by the WIMP scattering can be measured by detecting the induced light, charge or phonons. Many methods have been exploited in this respect (for a recent review, see [113]). The detection of the scintillation light produced in various materials is a consolidate technique in particle physics and can convert the kinetic energy of the particle into light with high efficiency (the list of experiments which have used or are using this technique include: DAMA/LIBRA [114], ZEPLIN [115], XENON [116], NAIAD [117], KIMS [118]). Experiments using semiconductors, like, e.g. Germanium, can convert about one third of energy of a nuclear recoil into ionization (HDMS [119], GENIUS [119], IGEX [120], MAJORANA [121], DRIFT [122], GERDA [123], CRESST [124]). Cryogenic noble liquids are suitable materials for detection of ionizing tracks (CLEAN [125], XMASS [126], DEAP [127]). In the double phase, combining liquid and gas, both ionization and scintillation can be exploited (SIGN [128], WARP [129], ZEPLIN, ArDM [130], XENON). Bubble chambers as WIMP detectors look for single bubbles induced by nuclear recoils with high energy loss rate in heavy liquid bubble chambers by means of acoustic, visual or motion detectors (COUPP [131], PICASSO [132]). Cryogenic experiments focus on quanta of lattice vibrations (phonons) and they have the advantage of increasing the energy resolution, with a low threshold (CDMS [133], CRESST, EDELWEISS [134], ROSEBUD [135]). The WIMP direction can be detected by tracking the nuclear recoil in a low-pressure gas (DRIFT). The experimental setup acts as a WIMP telescope and the WIMP wind would produce

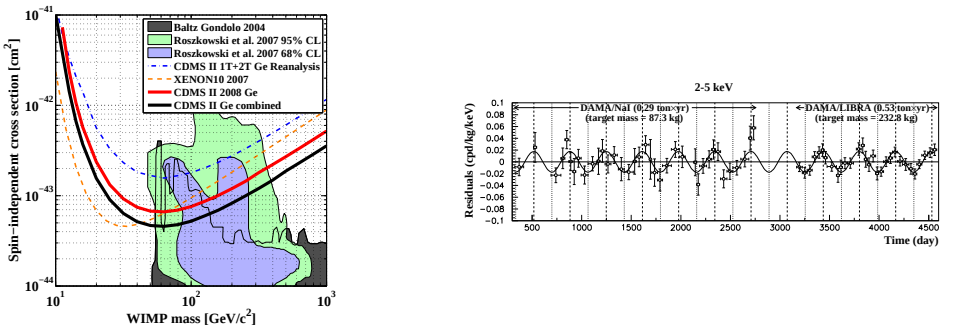

Figure 2.3: *Left Panel:* Experimental bounds from direct searches and theoretical predictions for spin-independent WIMP nucleon cross sections versus WIMP mass, in the case of neutralino. Figure taken from [136]. *Right Panel:* Residual rate measured by the DAMA/LIBRA experiment in the (2 - 5) keV energy intervals for recoil as a function of the time. The superimposed curve represents a cosinusoidal function with $\omega = 2\pi/1\text{yr}$ and $t_0 =$ June 2nd (see text) and the modulation amplitude is obtained by the best fit. See [158] for details.

a strong evidence.

Current limits on the WIMP parameter space are summarized in Fig. 2.3, for the spin-independent case.

2.6.2 Indirect searches

- **γ-rays**: Prompt emission of photons in the DM halo proceeds through the production and decay of neutral pions, final state radiation and direct production at loop level. In all these cases, the photons are injected with energy in the gamma-ray band. A monoenergetic spectral signature is often considered as a "smoking gun" for a gamma-ray signal originated from WIMP annihilations. Trajectories of photons are very slightly affected by the interstellar medium. Therefore, γ-ray searches can reproduce spectrum and morphology of the injection source. Indirect detection of WIMPs through γ-ray signals will be extensively discussed in the next Chapters.

- **Radiative emission**: Electrons and positrons can be directly or indirectly produced by WIMP annihilations in the DM halo. They act as sources for radiative processes generating a multi–wavelength spectrum. The radiative losses affecting the $e^+ - e^-$ propagation are synchrotron emission, inverse Compton scattering on CMB and starlight, bremsstrahlung, ionization, and Coulomb scattering. Secondary electrons/positrons mainly originate from the production and decay of charged pions. These processes are very fast and the $e^+ - e^-$ are basically injected at the same position where WIMP annihilations take

place. The computation of their final distribution requires, however, a model for the spatial diffusion, for the radiative processes and for the possible advection/convection effects in the astrophysical site where they travel after injected. The treatment of this subject will be described in the next Chapter.

- **Neutrino**: Depending on the WIMP model, neutrinos can be produced either directly or indirectly in DM annihilations. They can be detected through the Cherenkov light emitted by secondary muons propagating in water or ice. The Super-Kamiokande detector [137] is a water Cherenkov detector, located in Japan with 1000 m rock overburden. This project analyzed data over 1680 live days. At the South Pole, the AMANDA high-energy neutrino telescopes [138] have been operative in the recent past and the IceCube detector [139] is currently under construction (1 km^2 of effective area). The first stage of ANTARES telescopes [140] in the deep Mediterranean Sea has been recently completed.

  The DM overdensities at the Galactic center (GC), the Sun and the Earth have been investigated as sources of WIMP-induced neutrinos. Southern telescopes are not sensitive to the emission from the GC, and cannot put bounds on such emission. Moreover, the GC seems to be more promising for indirect searches of DM as a source for γ- or multi-wavelength photons, rather than neutrinos. When WIMPs scatter elastically with the Sun or the Earth, they can be deflected on gravitationally bound orbits and accumulate at the center of the massive body, with a density leading pair annihilations to become efficient. The annihilation rate is maximized when it reaches equilibrium with the capture rate. Among the various annihilation products, only neutrinos can escape from the body. The neutrino flux depends strongly on the WIMP elastic cross section with light nuclei, rather than to the annihilation cross section as in the previous cases. The spin-independent term is severely constrained by direct DM searches. Prospects for detecting neutrinos from the Sun are more promising than from the Earth, being the spin-dependent coupling suppressed in the latter. Upper bound on WIMP-induced neutrino flux have been derived by the null searches in AMANDA and Super-Kamiokande, see Fig. 2.4a. Prospects for detection in a km-size neutrino telescope, such as IceCube, are intriguing [142].

- **Antimatter**: Positrons, anti-protons and anti-deuterium, produced by WIMP annihilations in the galactic halo, can be detected as an exotic contribution in the spectra of cosmic-ray fluxes. Being charged, their propagation can be sketched as a random walk under the influence of the random component of the galactic magnetic field. Diffusion

isotropizes the distribution and the observed fluxes do not provide information on the location and the morphology of the sources. The identification as a DM-induced component and the disentanglement from other astrophysical sources is thus harder for this type of indirect signals.

After the injection by DM annihilations, the propagation of particles can be described through the transport equation (see next Chapter for the positron case). Both analytic and numerical (see, e.g., [143] and references therein) treatments have been developed to solve it. One of the largest source of uncertainty in the theoretical prediction is related to the poor knowledge of the astrophysical parameters entering in the transport.

The balloon flights of the High-Energy Antimatter Telescope (HEAT) experiment [144] measured the cosmic positron spectrum between 1 and 30 GeV, indicating the presence of an exotic excess at energies above 7 GeV, as shown in Fig. 2.4b. The PAMELA satellite [145] has been launched in 2006 and it is sensitive to positrons in the energy range 50 MeV - 270 GeV. Together with the future AMS-02 [147] on board the international space station could test the hypothesis of a DM-induced contribution in the spectrum. Note that, in order to be detected, a positron flux should require quite a large local DM overdensity in the Galaxy, since positron do not travel long distances ($\sim$ few kpc) in the diffusive halo.

On top of the continuum spectrum, in some models, WIMPs can produce a monochromatic signature in the positron flux, depending on the presence of a tree-level coupling between WIMPs and positrons.

Antiproton flux from DM annihilations has been investigated, focusing on a possible contribution at low energies, mainly because first measurements seemed to indicate an excess of antiprotons below 1 GeV. However, the data collected by several experiments, in particular BESS [148], CAPRICE [149] and BESS-Polar [148], agree with the calculations of the production by cosmic rays, showing no evidence for primary antiprotons. For heavy WIMPs (TeV scale), the annihilation flux can become comparable to the antiproton background at high energies and the new generation of space-based experiments, i.e. PAMELA and AMS-02, can probe this scenario [150]. In the case of AMS-02, the anti-proton spectrum will be tested up to energies of around 1 TeV.

Antideuterons have not been measured so far, and the present experimental bounds are still far from the expected flux of secondary anti-deuterons in cosmic rays. The antideuteron spectrum induced by DM annihilations is predicted to be much flatter than the standard astrophysical component at low kinetic energies [151]. In the future,

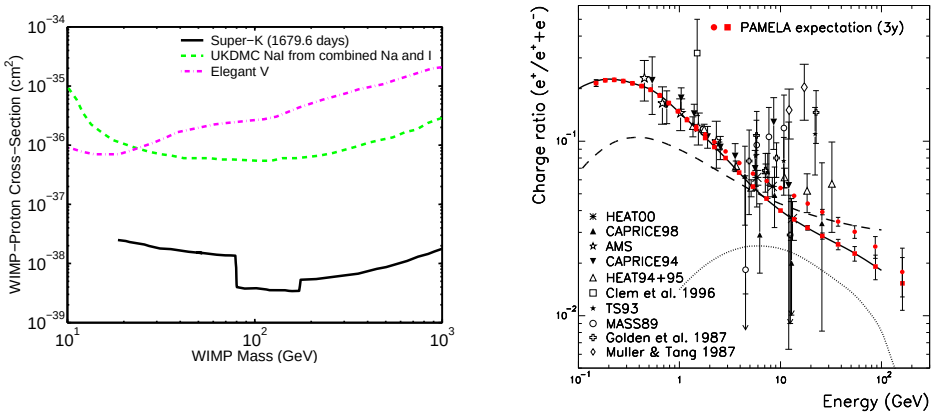

Figure 2.4: *Left Panel:* Super-Kamiokande 90 % CL exclusion region in WIMP parameter space for spin-dependent coupling. For details, see [141]. *Right Panel:* Cosmic positron fraction as a function of energy. Two models for the secondary positron fraction (dashed and solid lines) and the contribution from annihilations of neutralinos with mass of 336 GeV (dotted line) are shown. The figure is taken from [146].

for low and intermediate WIMP masses, this could be tested by the GAPS detector [152] in a ultra long duration balloon flight.

2.6.3 Collider signals

In the WIMP hunt, the different techniques, namely, direct, indirect, and collider searches, are highly complementary. Unambiguous discrimination among the plethora of WIMP candidates through direct or indirect evidences may not be easy. On the other hand, the constraints that can be placed on a DM candidate from collider experiments are highly model dependent, and do not allow for a simple description of the reach of colliders in DM searches. If the DM is in form of WIMPs, namely of massive neutral particle with a mass of the order of 100 GeV and weak interactions, it should be produced in reactions at the next generation of high-energy accelerators [153]. Production of WIMP particles in colliders can be inferred by the rate of missing energy events. Indeed WIMPs escape unseen from the detector, leading to an apparent non-conservation of the measured momentum.

Many other observables can be exploited in order to place indirect constraints on DM candidates, namely to test the extensions of the SM embedding the WIMP. They includes the width of the invisible Z decay, the search for new charged or colored particles and for the Higgs, constraints on flavor changing neutral current, on the decays $b \to s\gamma$ and $B_s \to \mu^+\mu^-$, the

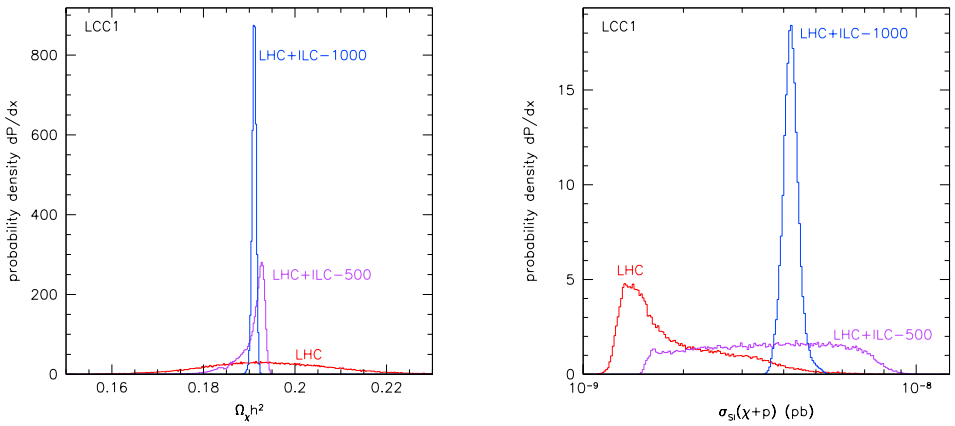

Figure 2.5: Collider estimates of the WIMP relic density (*Left Panel*) and elastic scattering cross section (*Right Panel*) for a specific benchmark SUSY model (LCC1). See [153] for details.

measurements of the anomalous magnetic momentum of the muon, and the EW precision tests [23].

Collider measurements of new physics can allow to discriminate among models beyond the SM and thus to discriminate among WIMP candidates (see, e.g. Ref. [154] for UED and SUSY). Moreover, collider observations can be cross-correlated to direct or indirect evidences of WIMPs in order to help in estimating its cosmological abundance, as shown in Fig. 2.5a.

- **Tevatron**: Physics beyond the SM could be discovered at Tevatron [155], although it is much less probable than at LHC. The experiment consists in proton-antiproton collision with center-of-mass energy of ~ 2 TeV. Signals for WIMPs are again related to missing energy. In the case of heavy neutralino, the best channel is through a tri-lepton plus missing energy decay due to an interaction between chargino and neutralino. In the data collected so far, no evidence for SUSY has been found [156].

- **LHC**: The LHC first beam has been injected on 10 September 2008 at CERN [6]. The related experiments will look for products of proton-proton collision at an energy of 7 TeV per beam. New particles with QCD interaction and TeV mass are often predicted by models beyond the SM. They will be pair-produced at LHC and can decay into the lightest particle of the new sector, namely the WIMP candidate. The rate of missing energy events associated to WIMPs strongly depends on the mass of this colored particles. LHC can also help in determining the WIMP-nucleon elastic scattering cross section and can be correlated with direct searches, as shown in Fig. 2.5b.

- **ILC**: The planned International Linear Collider [157], an $e^+ - e^-$ linear collider with 500 or 1 TeV centre-of-mass energy, will be very powerful for precision measurements. Quantum numbers of any particles with electric or weak interaction and with pair-production energy under the threshold can be precisely tested. The complementarity of LHC and ILC in looking for physics beyond the SM is crucial (see [153] for WIMP searches). Indeed, LHC will reach larger energies and more states of the new particle spectrum are accessible. On the other hand, ILC will provide more precise measurements of the properties of the particles energetically available and can play a very important role in DM searches.

2.6.4 Observational excesses with a possible DM interpretation

- **DAMA**: To convincingly disentangle a WIMP signal with direct detection experiments, the searches have to focus on a specific signature. One possibility is offered by the annual modulation of the WIMP signal, which arises because of the Earth's motion: $v_E = v_{sun} + v_{orb} \cos\gamma \cos[\omega(t - t_0)]$ where v_{sun} is the Sun velocity in the galactic frame, v_{orb} denotes the Earth's orbital speed around the Sun, the angle γ is the inclination of the Earth's orbital plane with respect to the galactic plane, $\omega = 2\pi/1\text{yr}$, and $t_0 =$ June 2nd. The expected time dependence of the count rate of Eq. 2.17 can be approximated by $S(t) = S_0 + S_m cos[\omega(t - t_0)]$, where S_0 and S_m are the constant and the modulated amplitude of the signal, respectively. The DAMA/NaI experiment claimed a model independent evidence for the presence of DM particles in the galactic halo. Recently, the same collaboration confirmed the result at $8.2\,\sigma$ C.L., with the data taken from the highly radiopure 250 kg NaI DAMA/LIBRA setup [158]. The modulation of the signal is shown in Fig. 2.3b. However, this claim is highly controversial. Indeed, other experiments with better sensitivities, like, e.g., KIMS, CDMS, and XENON10, excluded the WIMP scattering cross section required to explain the DAMA results. On the other hand, the counterarguments of the DAMA collaboration include the fact that all the other experiments have looked for a different signature (not the annual modulation), have used different materials (not NaI), and some models predicting extremely light WIMPs (with mass $\lesssim 10$ GeV) could be not excluded [159]. Current experiments (KIMS, GERDA) are taking data in this respect to definitively rule out or confirm the DAMA claim.

- **Positrons**: In 1994, the HEAT experiment has observed an exotic excess at high energy in the positron fraction, i.e. the ratio between

positron flux and positron plus electron flux (see Fig. 2.4b). Although astrophysical explanations have been proposed, the standard propagation model of cosmic rays cannot account for it. The excess has been confirmed by the AMS-01 collaboration, but with a rather poor statistics. Recent preliminary results of the PAMELA collaboration [160] confirm the anomalous behaviour of the flux at high energy with a much higher significance. On the other hand, the rest of the spectrum turns out to be incompatible to the previous surveys, probably indicating that solar modulation is a significant effect and has to be properly considered. The detected positron fraction is definitively not consistent to the expectation of Fig. 2.4b.

The positron spectral shape induced by WIMP annihilation is able to fit this excess. However, for a smooth DM halo and typical annihilation cross section (i.e., $\sigma_a v \sim 3 \cdot 10^{-26} cm^3 s^{-1}$), the contribution is a factor $\gtrsim 50$ lower with respect to the measured flux. Enhancement of the annihilation rate could be restricted by bounds on other indirect signals, and a boost factor of 50 related to fluctuations of the local DM density seems unnatural. WIMP candidates with a large branching ratio in leptons leads to harder positron spectrum, and can be exploited more easily to fit the excess.

- **511 keV emission line**: The INTEGRAL collaboration detected a 511 keV line from a region of size ~ 8 degrees centered around the GC. This line has been identified with a high level of confidence as originating from electron-positron annihilations. The observation of a relatively high fraction of low energy positrons in the bulge and a low fraction in the disk is considered as the most puzzling aspect of this emission and conventional astrophysical scenarios cannot reproduce it. DM annihilations can act as a positron source and it has been claimed as an explanation for the excess. However, in this case, WIMPs would overproduce γ-rays from pion decays, violating experimental bounds. More exotic scenario, like, e.g., light DM [161], decaying DM [85] or exciting DM [162] maybe, instead, more successful in this respect.

- **Galactic center source**: The EGRET team has reported the observation of a GC source in the energy range 100 MeV–20 GeV [163]. The angular resolution of EGRET was rather poor, about 1 degree at 1 GeV, encompassing a large portion of the GC and not allowing for a clean identification of the emitter. In Ref. [164], the authors argue that the improvement of the instrument angular resolution at multi-GeV energies should be taken into account in the data analysis, and conclude that the EGRET source might be slightly offset with respect to the GC. The detection of TeV gamma-ray radiation from the GC has been reported by HESS [165, 166, 167]. Such a measurement has been

confirmed, with a consistent spectrum, by MAGIC [168] and supersedes previous results by CANGAROO [169] and Whipple [170], whose significantly different spectra is likely due to a miscalibration of the detector and poorer statistics rather than variability of the source. HESS has discovered a point source, whose position is coincident with Sgr A* within 7.3 arcsec $\pm$ 8.7 arcsec (stat.) $\pm$ 8.5 arcsec (syst.) [171], excluding the identification with the nearby supernova remnant Sgr A East, but not with other candidates, such as a pulsar wind nebula recently discovered by Chandra [172] which is only 8.7 arcsec away from Sgr A*. The luminosity spectrum of the HESS point source is a rather featuresless flux, $\phi_\gamma \propto E^{-\alpha}$ with spectral index $\alpha \simeq 2.25$, extending from 160 GeV up to above 20 TeV. Even on the basis of the spectral characteristics only, without any consistency checks at other wavelength, it has been shown that it is rather implausible that such a source is due to WIMP annihilations only [173, 174, 175, 176].

- **Diffuse Galactic gamma-ray background**: The EGRET data shows an excess in each direction of the sky, pointing toward the presence of a bump in the Galactic gamma-ray emission at few GeV. It has been tentatively interpreted in terms of DM annihilations of a WIMP with mass around 60 GeV [177]. This possibility is not excluded, but the model of [177] likely leads to a DM distribution in the shape of a ring around the GC. This is in contrast to the result of ΛCDM numerical simulations. Moreover, more standard astrophysical explanation can be invoked to fit the excess, like, e.g., a spectrum of injection for cosmic rays which is mildly different with respect to the conventional scenario [178].

- **WMAP haze**: The foreground estimate in CMB experiments is not a completely established issue. In the analysis of the WMAP data in Ref. [179], an excess of microwave emission in the inner 20 degrees around the center of the Galaxy is claimed. It has been called WMAP "Haze". Contrary to the WMAP team, they argue that the anomalous emission cannot be entirely explained by a spinning dust component. The derived angular profile can be reproduced by a synchrotron emission induced by WIMP annihilations, with a rather steep ($r^{-1.2}$) DM profile [180]. It should imply an associated gamma-ray signal detectable by the Fermi gamma-ray space telescope [181]. On top of the uncertainties on the existence of the Haze, polarization maps seem to indicate that the anomalous emission is unpolarized [182], namely, incompatible with a synchrotron signal.

Chapter 3

Multi-wavelength signals of WIMP annihilations

In the previous Chapter, we introduced the WIMP DM scenario. The framework is elegant and simple: stable WIMPs can be embedded in most extensions to the standard model of particle physics. In thermal equilibrium in the early Universe, they decouple from the primordial bath in the non-relativistic regime. Their relic abundance scales approximately with the inverse of their total pair annihilation rate into lighter particles: the weak-interaction coupling ensures that, within the standard cosmological scenario, such relic density is of the order of the mean density of DM in the Universe today, as determined in cosmological observations.

In principle, one of the routes to test the hypothesis of WIMP DM stems from the bases of the framework themselves[1]. Supposing that WIMPs are indeed the building blocks of all structures in the Universe, there is a (small but finite) probability that WIMPs in DM halos, including the halo of the Milky Way, annihilate in pairs into detectable species. As already mentioned, indirect detection of WIMPs in the DM halo has mainly been focused on the search for a WIMP-induced component in the local antiproton, positron, and antideuteron cosmic-ray fluxes and for an excess in the high-energy gamma-ray galactic or extra-galactic flux (relevant constraints on the WIMP parameter space have been derived from such analyses; for recent results, see, e.g., [184, 185, 186, 187]).

A very promising strategy for testing WIMP models is the simultaneous analysis over the whole electromagnetic spectrum of the photon emissions induced by WIMP annihilations. This multi-wavelength approach has been exploited for different astrophysical objects, like galaxy clusters [188], dwarf satellites [189], galactic DM clumps [190], the Large Magellanic Cloud [191], and the GC [183].

[1] The analysis reported in this Chapter mainly follows the line of Ref. [183].

3.1 DM WIMPs as a multi–wavelength source

The emission associated to WIMP annihilations is expected to extend from the radio band up to gamma-ray frequencies. The peak of the gamma-ray luminosity stands at the energy corresponding to a fraction (say one-third to one-twentieth) of the WIMP mass, which is in turn in the few (tens of) GeV – few TeV range; it is mostly associated to the chain of decays and/or hadronization processes initiated by two-body final state particles[2] from WIMP pair annihilations, leading to the production of neutral pions and their subsequent decays into two photons. In an analogous chain, with analogous efficiency, high-energy electrons and positrons are produced by charged pions. Emitted in a region with magnetic fields, they give rise to synchrotron emission covering radio frequencies up to, possibly, the X-ray band (in the case of large magnetic fields, as typical, e.g., for accretion flows around supermassive black holes). The inverse Compton (IC) scattering of ultra-relativistic electrons and positrons on the CMB and on starlight can fill the gap from X-ray to soft gamma-ray frequencies.

The DM WIMP source scales with the number density of WIMP pairs locally in space, i.e. assuming a smooth (i.e. without substructures), spherically symmetric, and static dark matter distribution, with $\rho^2/2\,M_\chi^2$, with $\rho(r)$ being the halo mass density profile at the radius r, and M_χ the mass of the dark matter particle[3]. Emitted stable species are nearly monochromatic if they are direct products of the annihilation (since the annihilating particles are essentially at rest); they have much broader spectra if they are generated in cascades with decays and/or hadronization processes of unstable two-body final states. For a given species i, the source function takes the form:

$$Q_i(E,r) = (\sigma v)\,\frac{\rho(r)^2}{2\,M_\chi^2} \times \frac{dN_i}{dE}(E)\ , \tag{3.1}$$

where σv is the annihilation rate at zero temperature, and dN_i/dE is the number of particles i emitted per annihilation in the energy interval $(E, E+dE)$, obtained by weighting spectra for single annihilation channels over the corresponding branching ratio.

The species which are relevant in a multi–wavelength analysis are photons, as well as electrons and positrons which act as sources for radiative processes. For most WIMP models, branching ratios for monochromatic emission in these channels are subdominant; in our analysis, we will concentrate on the components with continuum spectra. In the case of monochro-

[2]The contribution from final state radiation [174, 192], which is a highly model-dependent feature of the gamma-ray spectrum, is not included in the analysis of this Chapter. It will be considered for the specific DM candidate described in Chapter 4.

[3]If the subhalo population component significantly contributes to the signal, the expression for ρ has to be replaced and requires a model for both the large-scale smooth and the clumpy distributions (see, e.g., [193])

matic emissions, the spectrum dN_i/dE in Eq. 3.1 will be replaced by a delta function peaked at energy M_χ (for $\chi\chi \to \gamma\gamma$ or $\chi\chi \to e^+e^-$) or at $M_\chi(1 - m_Z^2/4M_\chi^2)$ (for $\chi\chi \to Z\gamma$) times the branching ratio of the related annihilation channel.

For reference and to make transparent the connection with the notation introduced below for radiative processes, the γ–ray emissivity can be written as :

$$j_\gamma(E, r) = Q_\gamma(E, r)\, E \ . \tag{3.2}$$

In the energy range of interest for this analysis absorption is negligible, and fluxes or intensities can be straightforwardly derived summing contributions along the line of sight. E.g., the differential γ–ray flux is:

$$\phi_\gamma(E, \theta) = \frac{1}{E} \int_{l.o.s.} ds\, \frac{j_\gamma(E, r(s, \theta))}{4\,\pi} \tag{3.3}$$

where the coordinate s runs along the line of sight and θ is the angular off–set with respect to the center of the observed system.

For a radiative process i, with associated power P_i, the photon emissivity is given by folding the e^+/e^- number density n_e with the power [194]:

$$j_i(\nu, r) = 2 \int_{m_e}^{M_\chi} dE\, P_i(r, E, \nu)\, n_e(r, E) \ , \tag{3.4}$$

where m_e is the electron mass and the factor 2 takes into account electrons and positrons (in WIMP annihilations, as well as during propagation, there is perfect symmetry between particles and antiparticles). Electron and positron populations originate from the DM annihilations and, accordingly to the properties of the medium in which they are injected, their distribution functions evolve. The determination of n_e requires the solution of a transport equation. In Section 3.3, we will consider in a detailed analysis the case of the GC.

For any given emission mechanism, the associated luminosity at frequency ν is

$$L_i(\nu) = \int d^3r\, j_i(\nu, r) \ , \tag{3.5}$$

while the intensity measured by a detector can be estimated as

$$S_i(\nu, \theta, \theta_d) = \int d\Omega' \exp\Big(- \frac{\tan^2\theta'}{2\,\tan^2\theta_d} \Big) \int_{l.o.s.} dI_i(\nu, s, \tilde{\theta}) \ . \tag{3.6}$$

Here θ labels the direction of observation and we are performing an angular integral assuming a circular Gaussian resolution of width θ_d for the detector. dI_i is the differential of the intensity of radiation I_i: within the increment ds along a line of sight, there is a gain in intensity $j_i/(4\,\pi)\, ds$, while a decrease

$\alpha\, I_i\, ds$ could be due to absorption, where α is the absorption coefficient. I_i follows from the solution of the differential equation:

$$\frac{dI_i(\nu, s, \tilde{\theta})}{ds} = -\alpha(\nu, s, \tilde{\theta})\, I_i(\nu, s, \tilde{\theta}) + \frac{j_i(\nu, s, \tilde{\theta})}{4\pi} \tag{3.7}$$

where $\tilde{\theta}$ is the angular off-set from the center of the system of the line of sight along which I_i is calculated, as selected by θ and the angular variables of integration θ' and ϕ'. If absorption is negligible, the second integrand of Eq. 3.6 reduces to $dI_i(\nu, s, \tilde{\theta}) = ds\, j_i(\nu, s, \tilde{\theta})/(4\,\pi)$.

At low and intermediate frequencies, i.e. in the radio band up to (possibly) the soft X-ray band, the DM signal is mostly due to synchrotron radiation. The power for synchrotron emission takes the form [194]:

$$P_{syn}(r, E, \nu) = \frac{\sqrt{3}\, e^3}{m_e c^2}\, B(r) F(\nu/\nu_c)\ , \tag{3.8}$$

where B is the magnetic field, the critical synchrotron frequency is defined as $\nu_c \equiv 3/(4\,\pi) \cdot c\, e/(m_e c^2)^3 B(r) E^2$, and $F(t) \equiv t \int_t^\infty dz K_{5/3}(z)$ is the standard function setting the spectral behavior of synchrotron radiation.

The emission through inverse Compton scattering of the ultra–relativistic electrons from WIMP annihilations on cosmic microwave or starlight background photons, could be relevant as well. This emission spans the X-band up to the (soft) γ-ray band. The inverse Compton power is given by

$$P_{IC}(r, E, \nu) = c\, h\nu \int d\epsilon\, \frac{dn_\gamma}{d\epsilon}(\epsilon, r)\, \sigma(\epsilon, \nu, E) \tag{3.9}$$

where ϵ is the energy of the target photons, $dn_\gamma/d\epsilon$ is their differential energy spectrum, and σ is the Klein–Nishina cross section. Finally, a very faint emission is expected in case of bremsstrahlung, ionization, and Coulomb scattering; we will not consider them in our analysis.

3.2 The case for Galactic Center

Since the gamma-ray signal scales with the square of the WIMP density along the line of sight, the Galactic center has been often indicated as the prime target. In any self-consistent model for the distribution of DM in galactic halos, the DM density is found to be maximal at the center of the system. As discussed in Chapter 1, numerical N-body simulations of hierarchical clustering in ΛCDM cosmologies find configurations with very large overdensities, consistent with singular density profiles [27, 46, 47]. (notice, however, that the simulations lack resolution to map the distribution of DM on the very small scales which are relevant for WIMP signals). The recent Aquarius simulation [195] (which is the one considering the greatest number

of particles $\sim 1.5 \cdot 10^9$ in the halo), seems to indicate the GC as the most favorable target in terms of signal to background ratio for the indirect detection of DM. Although there is not a full consensus for this view in the N-body simulation community [196] and the role of baryons, which are not considered in the simulation, can substantially modify the picture, this result could suggest that the observable signal is dominated by the component from the GC, rather than by small clumps or dwarf satellites.

The GC is an extraordinary site from several different points of view. Dynamical observations point to the presence of a supermassive black hole [197, 198, 199], with mass $M_{\rm BH} \sim 3 \times 10^6 M_\odot$, located very close to the dynamical center of the Galaxy, and most likely associated to the compact radio source labeled Sgr A*. Infrared and X-ray counterparts have been identified for Sgr A*; GeV and TeV emissions in the direction of the GC have been detected as well, with the first data with high statistics and fair angular resolution which have been obtained with the HESS air Cherenkov telescope [165]. Sgr A* is an unusual source, certainly very different from typical galactic or extragalactic compact sources associated to black holes. Most notably, under our perspective, it has a very low luminosity over the whole spectrum, at a level at which it is plausible that a WIMP-induced component may be relevant.

Numerous analyses have been dedicated to the study of the GC as a WIMP gamma-ray source, a list of recent references includes, e.g., [200, 201, 164, 202, 203, 173, 174, 175, 204, 176, 205]. A prediction for the synchrotron emission has been discussed in Refs. [206, 207], and refined on several aspects in Ref. [208]; a comparison with X-ray data motivated by a class of heavy WIMP DM candidates is presented in Ref [209]. We consider here the topic within a self-consistent multi–wavelength approach. Referring to a generic WIMP DM scenario, we discuss spectral and angular features, and sketch the correlations among signals in the different energy bands. We illustrate which are the critical assumptions in deriving such conclusions, analyze them in the context of the currently available datasets, and make projections for the testability of the framework in the future.

3.2.1 Overview of data on Sgr A* and the GC region

The radio to sub-mm emission from Sgr A* is characterized by a very hard spectrum: the luminosity above $\nu \sim 1$ GHz scales approximately as $L_\nu \sim \nu^\alpha$ with $\alpha \simeq 0.8$ and cut-off at about $\nu \sim 10^3$ GHz (a compilation of available data and a full list of references is given, e.g.. in Ref. [210]). We will show that such features do not seem to be compatible with the synchrotron emission induced by WIMP annihilations, not even with the observed flux reshaped by synchrotron self-absorption. In general, softer spectra are obtained, and the comparison with observations is useful to infer limits on the WIMP parameter space. The tightest bound follows from the measurement

at the lowest frequency, i.e. the upper bound on the flux density $S_\nu \leq 0.05$ Jy at the frequency $\nu = 408$ MHz, obtained with an interferometer with 4.3 arcsec angular acceptance at Jodrell Bank [211].

Although variations are clearly seen in the radio flux density at different epochs, clean patterns of temporal dependencies have not been identified, see, e.g., [212]; the data plotted in Fig. 3.1 are not time-averaged. At any given frequency, we show, among the available measurements, the one corresponding to the epoch of lowest luminosity.

The angular size of the source depends on the frequency of observation. At 1 GHz, a frequency at which it is expected that scattering in the interstellar medium would wash out the true structure of Sgr A*, it is of the order of 1.5 arcsec [211]. At higher frequencies, the size shrinks proportionally to ν^{-2} up to the measured value of 0.2 mas (about 1 AU in physical size) at about 86 GHz [213], possibly at the level of the intrinsic size of the source. We will show that, at radio frequencies, the angular size of a WIMP-induced component is expected to be much larger than these apparent or intrinsic angular dimensions; we find sizes for which it is actually interesting to compare with wide field images of the GC region rather than Sgr A* alone. Among the available surveys, we will refer again to those at the lowest frequency, namely at 90 cm. An atlas of the diffuse radio emission in the Milky Way was presented in [214]. The evidence for a GC diffuse non-thermal source was enlighted in [215]. Both maps have an angular resolution $\sim 1^\circ$, thus hiding the spatial structure of the diffuse emission in the innermost region. We will consider an image of the GC region constructed from VLA data, covering an area of 4×5 degrees and with angular resolution of 43 arcsec [216].

The near-infrared and X-ray emissions from Sgr A* are characterized by a large variability (on different timescales in the two cases): quiescent values for the luminosity are plotted in Fig. 3.1. The quiescent flux in the near-infrared has been recently detected with the VLT [217, 218] as a point source with a position coincident with the supermassive black hole within an accuracy of 10-20 mas, limited by faintness and by the proximity of one of the stars orbiting the black hole [199]. Launched in 1999, NASA's Chandra X–ray observatory is at present the most powerful X–ray detector, covering the energy range 0.1 kev–10 kev with an angular resolution of 0.5 arcsec. During its observations, it has clearly discovered an X–ray source consistent with the position of Sgr A* [219, 220], whose quiescent emission is well fitted by an absorbed thermal bremsstrahlung plus a Gaussian-line, plotted in Fig. 3.1. The spatial dimension of the X-ray source is 1.5 arcsec. The process involving WIMP annihilations is expected to be steady, i.e. it cannot reproduce any time variability pattern. We will show that a X–ray flux at the quiescent level detected by Chandra can be obtained in the case of large WIMP densities and large magnetic field; moreover the source is predicted essentially as point–like, rather than the extended source seen by the Chandra detector. We will use Sgr A* infrared and X–ray data to set constraints on WIMP models.

Chandra detected also a diffuse emission in several regions within the inner 20 pc of the Galaxy. The reconstructed image covers a field of view of $17' \times 17'$ around Sgr A* [221]. This diffuse emission could be consistently modeled as originating from a two–temperature diffuse plasma. The soft component ($kT \sim 0.8$ keV) could be explained invoking different astrophysical mechanisms, while the origin of the hard component ($kT \gtrsim 3$ keV), spatially uniform, is not clearly understood. In principle it could be explained in terms of inverse Compton scattering on CMB induced by WIMP annihilations; however the detection of several emission lines and the inconsistency with limits at other frequencies make this hypothesis unplausible.

We come finally to gamma-ray observations. We have already mentioned in Section 2.6.4, that the identification of the source detected by EGRET at the GC with Sgr A* is not guaranteed, due to the poor angular resolution of the telescope. As it can be seen in Fig. 3.1, the luminosity of such a source exceeds by about one order of magnitude the luminosity of Sgr A* at any other frequency. In Ref. [164], it is suggested that the comparison to set constraints on WIMP models should be with the diffuse background measured by EGRET in the GC region, rather than with the EGRET GC source.

The detection of TeV gamma-ray radiation from the GC has been reported by HESS [165, 166, 167]. The position of the source is compatible to Sgr A*, within few arsec. We have discussed in Section 2.6.4 that it is rather implausible that this source is induced by WIMP annihilations only [173, 174, 175, 176]. HESS has also reported the detection of a diffuse gamma-ray emission along the central 300 pc of the GC ridge, within about 0.8 degree in longitude and 0.3 degree in latitude with respect to the GC. We will consider the central source and the diffuse emission as maximal background level to understand the potential for a discovery of a WIMP component with upcoming gamma-ray telescopes.

3.3 The transport equation at the GC

The emission through radiative losses involves charged particles, mainly electrons and positrons. Produced in WIMP pair annihilations, they propagate, losing and/or gaining energy. To describe this process, we consider the transport equation, in the limit of spherical symmetry, and for a stationary solution (see for example [143]; diffusive reacceleration is neglected):

$$-\frac{1}{r^2}\frac{\partial}{\partial r}\left[r^2 D \frac{\partial f}{\partial r}\right] + v\frac{\partial f}{\partial r} - \frac{1}{3r^2}\frac{\partial}{\partial r}(r^2 v)\, p\frac{\partial f}{\partial p} + \frac{1}{p^2}\frac{\partial}{\partial p}(\dot{p}p^2 f) = q(r,p) \quad (3.10)$$

where $f(r,p)$ is the $e^+ - e^-$ distribution function at equilibrium, at a given radius r and in terms of the momentum p, related to the number density in the energy interval $(E, E+dE)$ by: $n_e(r,E)dE = 4\pi\, p^2 f(r,p)dp$; analogously, for the WIMP source function of electrons or positrons, we have

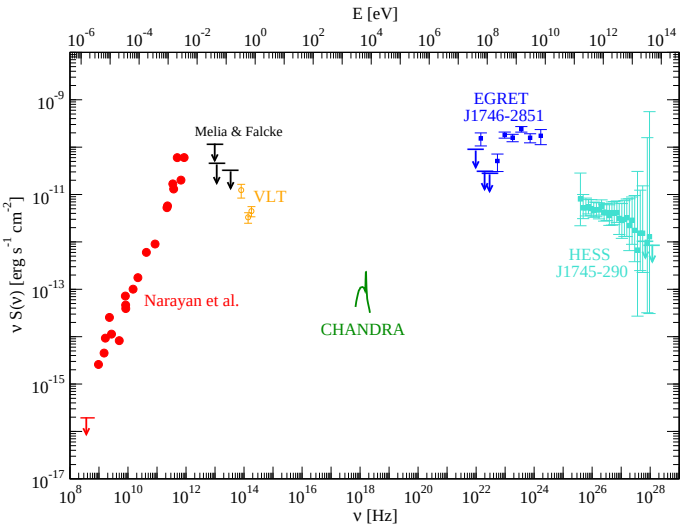

Figure 3.1: Multi–wavelength spectrum of Sgr A*. The radio to X–ray emissions are shown in the quiescent state or at the epoch of lowest luminosity among available observations. The plotted γ–ray sources have positions compatible with Sgr A*; however, due to a poor angular resolution, EGRET cannot clearly identify the source and perhaps neither the HESS telescope. See the text for details about the observations in each band.

$Q_e(r,E)dE = 4\pi\, p^2 q(r,p)dp$. The first term on the left-hand side (l.h.s.) describes spatial diffusion, with $D(r,p)$ being the diffusion coefficient. The second and third terms model an advective (convective) transport with an inflow (outflow) of the electrons and positrons toward (away from) the center of the system, being $v(r)$ the flow velocity of the medium. Finally, the last term on the l.h.s. describes the energy loss of due to radiative processes; $\dot{p}(r,p) = \sum_i dp_i(r,p)/dt$ is the sum of the rates of momentum loss associated to the radiative process i.

We apply Eq. 3.10 to the GC. The radiative losses affecting the $e^+ - e^-$ propagation are synchrotron emission, inverse Compton scattering on CMB and starlight, bremsstrahlung, ionization, and Coulomb scattering. We model the galactic medium as composed by molecular (H_2), atomic (HI), and ionized (HII) gases. The density profiles are extracted from the description of the central molecular zone in [222], approximating their results under the assumptions of spherical symmetry. The synchrotron loss rate is spatially dependent, scaling with the square of the local value of the magnetic field. We plot in Fig. 3.2a the time–scale for the energy loss associated to each radiative process, defined as $t_{loss} = E/\dot{E}$. We show the synchrotron emission for two reference values of the magnetic field, while the two curves for bremsstrahlung, ionization and Coulomb scattering refer to the losses at the GC and at a distance of 100 pc from the GC. We plot one curve for

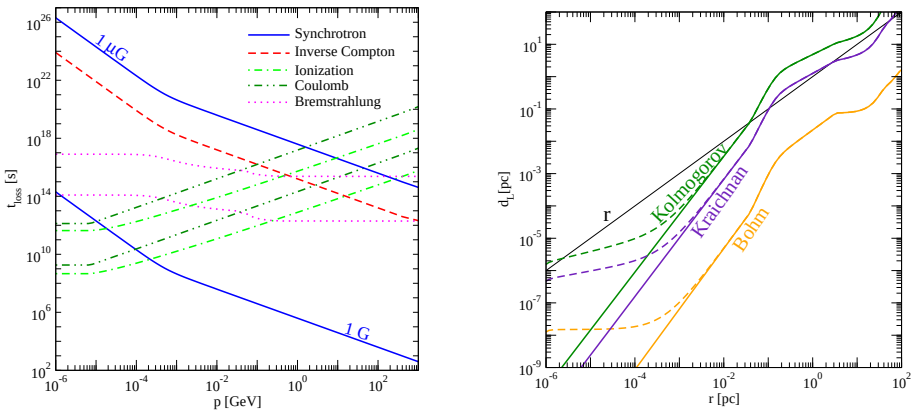

Figure 3.2: *Left Panel:* Timescales for different radiative losses as a function of the $e^+ - e^-$ momentum. Synchrotron losses are shown for two reference values for the magnetic field: $B = 1\,\mu G, 1\,G$. Radiative losses associated to bremsstrahlung, ionization and Coulomb scattering are shown at the GC (lower curves) and at a distance of 100 pc from the GC (upper curves). *Right Panel:* Distance d_L travelled by an electron with an injection energy of 1 GeV before losing most of its energy; three different guesses for the diffusion coefficient are shown, in the case of equipartition and reconnection magnetic field, see Fig. 3.3a (same line styles).

inverse Compton scattering; the time–scale is inversely proportional to the energy density of the background radiation; at the GC the energy density of the starlight component is considerably larger (8 eV cm^{-3} [223]) with respect to the CMB (0.25 eV cm^{-3}). We sum the two components assuming a starlight energy density constant over the whole GC region.

The radial profile of the magnetic field is indeed an important ingredient in our analysis. Based on observations of nonthermal radio filaments, polarization of thermal dust emission, and synchrotron radiation from cosmic rays, the canonical picture of the Galactic center magnetosphere (for a review, see [224]) describes the magnetic field with a dipolar geometry on large scale and as a pervasive field with strength of a mG throughout the central molecular zone (few hundreds of pc). The recent discovery of a diffuse source of nonthermal synchrotron emission [215] suggests, on the other hand, a mean magnetic field of order 10 μG on scales $\gtrsim$ few pc, unless reacceleration processes are invoked. It is important to note that such analyses constrain the mean magnetic field on scales $\gtrsim$ pc and do not exclude strong magnetic field in the innermost region. Following [225, 208], we consider a magnetic field for the GC region satisfying the equipartition condition, namely, with the magnetic energy completely balancing the kinetic pressure:

$$B(r) = 3.9 \cdot 10^4 \Big(\frac{0.01\,\mathrm{pc}}{r}\Big)^{5/4} \mu\mathrm{G}\ . \tag{3.11}$$

From a conservative point of view, this could be regarded as the maximal

allowed magnetic field; we discuss this case together with two further possibilities: We follow [209] and consider the case for a reduced magnetic field due to magnetic field line reconnection in turbulent plasma [226]; as a toy model of an extreme case at the other hand with respect to the equipartition assumption, we allow also for a magnetic field which is constant within the accretion region. Outside the accretion region, assuming spherical infall and flux conservation, the magnetic field scales as $B \propto r^{-2}$ up to the large–scale value $B \simeq 1\,\mu$G [143]. The three different choices for the magnetic field radial profile are shown in Fig. 3.3a.

Note that for magnetic fields B $\gtrsim$ 1 G (as is typical for the innermost region of the Galaxy), the synchrotron losses dominate at all energies. For lower magnetic fields, i.e. at larger scales, inverse Compton scattering (and bremsstrahlung) becomes relevant in the ultra–relativistic regime, while ionization starts to dominate in the non–relativistic limit.

In order to estimate the relevance of spatial diffusion, we compare in Fig. 3.2b the physical scale r with the distance diffused by electrons before losing most of their energy, $d_L \simeq (D\,E/\dot{E})^{1/2}$. In the quasilinear approximation of turbulent diffusion, the form of the diffusion coefficient D can be expressed as $D(r,p) = 1/3 r_g v_p (\delta B_{res}/B)^{-2}$, where $r_g = E/(eB)$ is the gyroradius of the electron, v_p is the electron velocity, and δB_{res} is the random component of the magnetic field at the resonant wavelength $k_{res} = 1/r_g$. On large scales (i.e., larger than about 100 pc) cosmic-ray data seem to indicate that the diffusion coefficient takes the form: $D = D_0\,(E_{GeV}/B_{\mu G})^{\alpha}$ with $\alpha \simeq 0.3 - 0.6$ and $D_0 \simeq 10^{27} - 10^{30}\mathrm{cm}^2\mathrm{s}^{-1}$ [143]; in the innermost region, the picture is much more uncertain. Indirect constraints are derived in the models of [166] and [227], when addressing the origin of the γ-ray source detected by HESS at the GC; in both analyses a significant reduction of the diffusion coefficient in the inner 10 pc region is found. On the modelling side, the relevance of diffusion is strictly connected with unknown variables needed in the description of turbulence, namely, the amplitude of the random magnetic field and the scale and the turbulence spectrum. As an example, one can assume comparable strengths for the regular and the random components of the magnetic field, and a power law, $k^{-2+\alpha}$ for the turbulence spectrum. For Bohm diffusion (typical when the coherence length of the magnetic field is comparable or greater with respect to the gyroradius of electrons), $\alpha = 1$ and the coefficient reduces to $D = 1/3 r_g v_p$; as one can see in Fig. 3.2b, in this case the effect of diffusion can be safely neglected. Assuming a turbulent regime (in a homogeneous medium) with a scale of turbulence $\sim r$, we find that, for $\alpha = 1/3$ ("Kolmogorov", i.e. assuming a random flow of an incompressible fluid) and $\alpha = 1/2$ ("Kraichnan", which is more plausible than the Kolmogorov spectrum in the case of the strong large-scale magnetic field), diffusion can be relevant from the sub-pc scale in the first case, and it is marginally relevant around the pc scale in the second case. Note that the main ingredient here is the very large magnetic field con-

sidered in the innermost region of the Galaxy. In our sample models, we find then that diffusion is either negligible over the whole central region or that it might be relevant only in its outer part, where, however, the DM source is expected to be less strong and have a less steep gradient than close to the central BH (see the discussion below). Therefore, we can foresee negligible to very mild effects from diffusion and, in what follows, for sake of simplicity and to make the discussion clearer, we will disregard the diffusion term.

We describe the accretion flow of gas onto the black hole in the innermost part of the Galaxy following [225, 208], namely, we assume that the supersonic wind entering the BH gravitational potential forms a bow shock dissipating kinetic energy and subsequently falls radially onto the BH. We take a spherical accretion and a steady flow, and estimate the region of the accretion as $R_{acc} = 2GM/v_{flow}^2$, where $v_{flow} \simeq 500 - 700$ km s^{-1} is the Galactic wind velocity and thus $R_{acc} \sim 0.04$ pc [225]. The radial infall velocity of the gas is

$$v(r) = -c\sqrt{\frac{R_{BH}}{r}} \tag{3.12}$$

A particle propagating in such accretion flow gains momentum since it feels an adiabatic compression in the BH direction.

The Galactic center lobe is a radio continuum emission spanning the central degree of the Galaxy with a bipolar structure. Recent mid-infrared observations [228] suggest the idea that the emission associated to the GC lobe is a sign of a GC outflow, in particular, a starburst outflow. The associated large-scale bipolar wind could affect the transport equation Eq. 3.10, convecting electrons and positrons. Assuming a velocity $\sim 10^2$ km/s [228], this effect is negligible in the innermost region, while it can be relevant on larger scales. On the other hand, although the model of [228] is probably the most intriguing, one can resort to other mechanisms explaining the origin of the Galactic center lobe (for a recent review, see, e.g., [229]). In the following we choose to neglect the effect of such a possible wind.

The solution of Eq. 3.10 provides the e^+/e^- number density n_e in the stationary limit. The emissivity associated to a radiative process can be estimated through Eq. 3.4.

3.3.1 The multi–wavelength seed in an approximate approach

In this section we sketch in a simple and analytic form the scalings of the dark matter induced signal depending on various assumptions in the model. Eq. 3.10 does not admit in general an analytic solution. However, when the radiative loss term dominates (and thus the first three terms are negligible), one finds simply:

$$n_e(r, E) = \frac{1}{\dot{E}(r, E)} \int_E^{M_\chi} dE\, Q_e(E, r) \tag{3.13}$$

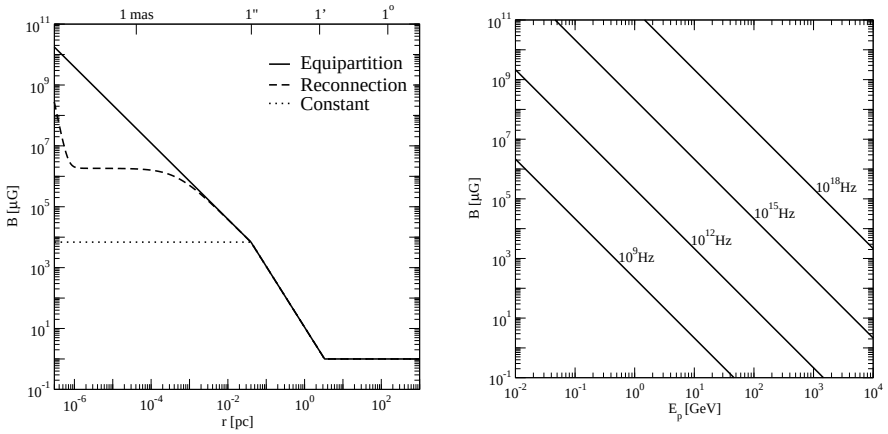

Figure 3.3: *Left Panel:* Models for the magnetic fields in the central region of the Galaxy as a function of the distance from the GC. *Right Panel:* Magnetic field as a function of the synchrotron peak energy for few values of the observed frequencies.

where $\dot{E}$ comes from $\dot{p}$ in Eq. 3.10 mapping momentum into energy. We have already stressed that synchrotron processes are the main effect for energy losses and radiative emissivity. We can focus, for the moment, on this mechanism, and write the energy loss rate as $\dot{E} = \dot{E}_{syn} = 4/9 \cdot (c\, e^4)/(m_e c^2)^4 B(r)^2 E^2$, and the induced synchrotron luminosity as

$$\begin{aligned} \nu L_\nu^{syn} &= 4\pi\nu \frac{\sigma v}{M_\chi^2} \int dr\, r^2 \rho(r)^2 \int_E^{M_\chi} \frac{P_{syn}(\nu, r, E)}{\dot{E}_{syn}(r, E)} Y_e(E) \\ &= \frac{9\sqrt{3}}{4} \frac{\sigma v}{M_\chi^2} \int dr\, r^2 \rho(r)^2 E_p\, Y_e(E_p) \end{aligned} \tag{3.14}$$

where we have defined $Y_e(E) = \int_E^{M_\chi} dE' dN_e/dE'$, and in the last step we have implemented the monochromatic approximation for the synchrotron power, i.e. assumed $F(\nu/\nu_c) \sim \delta(\nu/\nu_c - 0.29)$ [194]. In the monochromatic approximation there is a one-to-one correspondence between the energy of the radiating electron (peak energy in the power) and the frequency of the emitted photon, that is $E_p = \nu^{1/2} (0.29\, B(r)\, c_0)^{-1/2}$ with $c_0 = 3/(4\,\pi) \cdot c\, e/(m_e c^2)^3$, or, introducing values for numerical constants, the peak energy in GeV is $\widehat{E}_p \simeq 0.463\, \widehat{\nu}^{1/2} \widehat{B}^{-1/2}$, with $\widehat{\nu}$ the frequency in GHz and $\widehat{B}$ the magnetic field in mG. Analogously, the induced γ–ray luminosity is

$$\nu L_\nu^\gamma = 2\pi \frac{\sigma v}{M_\chi^2} \int dr\, r^2 \rho(r)^2\, E^2 \frac{dN_\gamma}{dE}\,. \tag{3.15}$$

It is useful to make a few simple guesses on some of the quantities introduced above. Along the line of [200], we assume the γ–ray spectrum per annihilation following the law: $dN_\gamma/dx \simeq \tilde{A}\, x^{-\tilde{B}} e^{-\tilde{C}x}$, with $x \equiv E/M_\chi$. It is

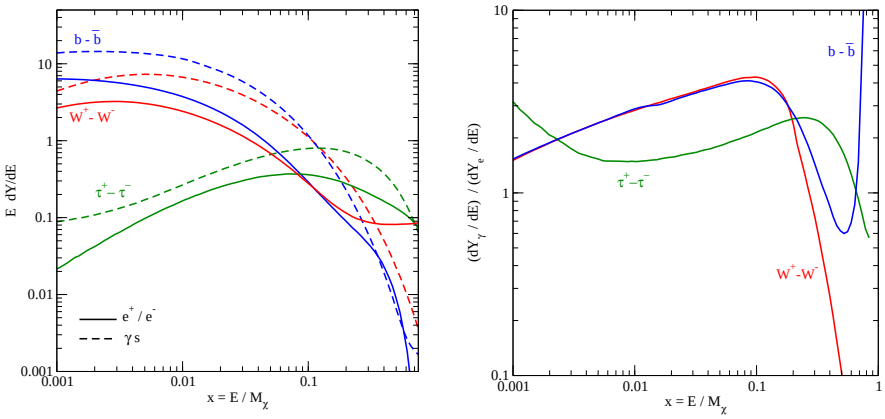

Figure 3.4: *Left Panel:* γ–ray and $e^+ - e^-$ spectra per annihilation for a 1 TeV WIMP. The three annihilation channels $b - \bar{b}$, $W^+ - W^-$, and $\tau^+ - \tau^-$ are taken as references. *Right Panel:* Multiplicity between the electron and photon yields $dN_\gamma/dE \times (dN_e/dE)^{-1}$ for a 1 TeV WIMP with the same annihilation modes as in the left panel.

also a fair assumption to approximate the integrated $e^+ - e^-$ yield as a power law plus an exponential cutoff: $Y_e(E) \simeq A\, x^{-B} e^{-Cx}$. The differential yields of secondary photons and $e^+ - e^-$ are plotted in Fig. 3.4a, for three sample cases of two-body final states from WIMP pair annihilations. These plots are obtained linking to simulations of decay/hadronization performed with the PYTHIA Monte–Carlo package [230] and stored libraries contained in the DarkSUSY package [96]; we will refer to such kind of simulations everywhere in the thesis when making detailed estimates of WIMP induced signals. As the simplest guess for radial dependence for the magnetic field and the DM profile, we consider the single power-law scalings, $B(r) = B_0 (r/r_0)^{-\beta}$ and $\rho(r) = \rho_0 (r/a)^{-\gamma}$. Eqs. 3.14 and 3.15 become:

$$\begin{cases} \nu L_\nu^{syn} = \dfrac{1.8\, A}{0.463^B} \dfrac{\sigma v}{M_\chi^2} \rho_0^2\, a^{2\gamma} \dfrac{\left(\widehat{\nu}/\widehat{B}_0\right)^{(1-B)/2}}{\widehat{M}_\chi^{-B}} \displaystyle\int dr\, r^{2-2\gamma} \left(\frac{r}{r_0}\right)^{\frac{\beta}{2}(1-B)} \\ \qquad \times\ exp\left[-\dfrac{C}{\sqrt{4.66}} \dfrac{\left(\widehat{\nu}/\widehat{B}_0\right)^{1/2}}{\widehat{M}_\chi} \left(\frac{r}{r_0}\right)^{\frac{\beta}{2}} \right] \ \text{GeV} \\ \nu L_\nu^{\gamma} = 2\pi \tilde{A} \dfrac{\sigma v}{M_\chi^2} \rho_0^2\, a^{2\gamma} \dfrac{\widehat{E}^{2-\tilde{B}}}{\widehat{M}_\chi^{1-\tilde{B}}} \displaystyle\int dr\, r^{2-2\gamma} exp\left[-\tilde{C} \frac{\widehat{E}}{\widehat{M}_\chi} \right] \ \text{GeV} \end{cases} \tag{3.16}$$

with $\widehat{M}_\chi$ the WIMP mass in GeV.

The right-hand-sides of Eq. 3.16 show some differences. For the gamma-ray luminosity, the energy cutoff follows simply from energy conservation and

thus scales with the dark matter mass, except for a O(1) factor related to the annihilation mode. For synchrotron emission, at a fixed mass, the frequency cutoff increases with the magnetic field, again except for a O(1) factor related to the annihilation channel. Away from the cutoff, the synchrotron emissivity tends to originate from a larger spatial region with respect to the γ–ray case, due to the additional positive power $\beta/2(1-B)$ in the radial dependence. At fixed mass and frequency, if the magnetic field is large enough to avoid the frequency cutoff, the synchrotron signal is wider than the gamma-ray signal. This is typically the case in the radio band and, to a much smaller extent, in the infrared band. Going to very high observed frequencies, however, the magnetic field (or the energy of the radiating electron or positron) needs to increase to exceedingly large values, which might be met only very close to the central BH (or for extremely massive WIMPs and/or hard $e^+ - e^-$ spectrum, as encoded in the factor C of Eq. 3.16). Scalings of the required magnetic field, as a function of peak radiating energy, for a few values of the observed frequency are shown in Fig. 3.3b: one can see that for the observed frequencies getting into the X-ray band (say 10^{18} Hz) a very small radial interval is selected, corresponding to the largest allowed value for the magnetic field. Hence, in this case the synchrotron signal is actually expected to be originated in a very small region around the central BH, possibly much smaller compared to the gamma-ray flux.

We can now make a sketchy estimate to find which of the limits in the different bands in Fig. 3.1 might be more constraining. We write the ratio between synchrotron and gamma-ray luminosity in the form:

$$\begin{aligned} r &= \frac{\nu L_\nu^{syn}}{\nu L_\nu^\gamma} = \frac{1.8}{2\pi\, 0.463^B} \frac{A}{\tilde{A}} \frac{\widehat{M}_\chi^{1+B-\tilde{B}}\, \widehat{\nu}^{(1-B)/2}}{\widehat{E}^{2-\tilde{B}}} \\ &\times \frac{\int dr\, r^{2-2\gamma} \left[\widehat{B}(r)\right]^{-(1-B)/2} \exp\left[-\frac{CE_p(r)-\tilde{C}E}{M_\chi}\right]}{\int dr\, r^{2-2\gamma}} \,. \end{aligned} \tag{3.17}$$

In Fig. 3.4b we plot the relative multiplicity between photons and electrons for the three benchmark final states from WIMP pair annihilations considered in Fig. 3.4a. This illustrates the fact that, sufficiently far away from the energy cutoff and for a generic WIMP annihilation channel (except, of course, for the case of prompt emission of monochromatic gammas, and/or electrons/positrons we are not considering here), the photon and electron/positron yields are comparable and hence that it is difficult to avoid the correlation between the gamma and the synchrotron signals by selecting a specific WIMP model. In Eq. 3.17 this implies that the ratio $A/\tilde{A}$ is typically O(1). The last term in Eq. 3.17 does critically enter in boosting or suppressing the ratio of luminosities only in case the exponential cutoff (or the upper limit in the radial integral) is playing a role, i.e. at very large observational frequencies for synchrotron emission (the X-ray band) or for

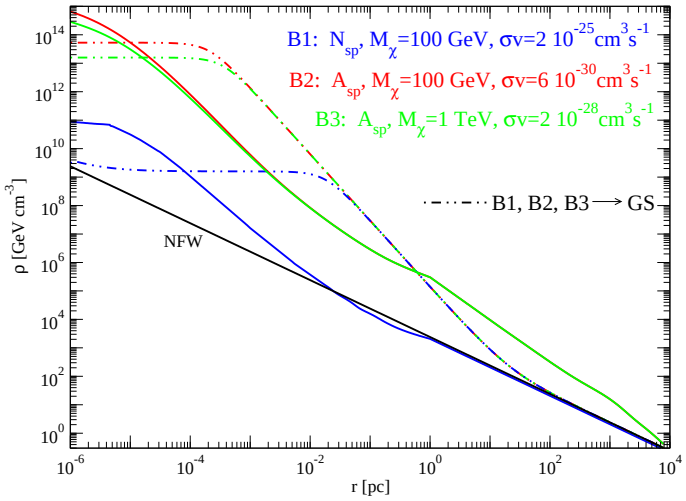

Figure 3.5: Dark matter profiles for the benchmark models B1, B2, and B3. For comparison we plot also the NFW profile and NFW profiles modified by the original prescription by Gondolo-Silk (GS) to account for the growth of the central black hole: the value of the ratio $(\sigma v)/M_\chi$ are the same as in the benchmark models.

shallow density profiles. Restricting to the case of singular halo profiles, and, e.g., synchrotron emission in the radio band, the ratio r is of order O(1) or O(0.1). To see this more precisely, let us take $W^+ - W^-$ as the annihilation channel, as an intermediate case between the soft quark spectra and the hard leptonic spectra. We find that integrated $e^+ - e^-$ yield, for masses in the range $M_\chi = 100$ GeV–10 TeV, can be fairly well approximated by $(A, B, C) \simeq (0.1, 0.7, 3)$; the differential γ–spectrum was fitted in [200], finding $(\tilde{A}, \tilde{B}, \tilde{C}) \simeq (0.73, 1.5, 7.8)$. Since $B \simeq 0.7$, the rescaling factor $\left[\widehat{B}(r)\right]^{-(1-B)/2}$, in the integral in the numerator of Eq. 3.17, varies at most between about 0.09 and 3, hence we can assume as a sample value for the suppression expected from the ratio of integrals a factor of 0.5. Inserting all fit parameters in Eq. 3.17, we get:

$$r_W \sim 9 \cdot 10^{-2} \left(\frac{M_\chi}{100\,\mathrm{GeV}}\right)^{0.2} \left(\frac{\nu}{1\,\mathrm{GHz}}\right)^{0.15} \left(\frac{1\,\mathrm{GeV}}{E}\right)^{0.5} \tag{3.18}$$

We find hence that the radio and γ–ray luminosities are at a comparable level, while as it can be seen in Fig. 3.1, constraints in the γ–ray band are several orders of magnitude weaker than at radio wavelengths. Although the luminosities of Eqs. 3.14 and 3.15 cannot be directly compared with such experimental data, since they are integrated over the whole emission region, which can be significantly larger than within the angular acceptance in the observations, and relevant effects such as advection and synchrotron self-absorption have been neglected, our approximate result in Eq. 3.18 puts

	M_χ	σv	ann. mode	B	ρ
B1	100 GeV	$2 \cdot 10^{-25}\,\mathrm{cm^3 s^{-1}}$	$b-\bar{b}$	Equipart.	N_{sp}
B2	100 GeV	$6 \cdot 10^{-30}\,\mathrm{cm^3 s^{-1}}$	$b-\bar{b}$	Reconnect.	A_{sp}
B3	1 TeV	$2 \cdot 10^{-28}\,\mathrm{cm^3 s^{-1}}$	$b-\bar{b}$	Constant	A_{sp}

Table 3.1: Benchmark models.

us on the track that the strongest constraints on the WIMP parameter space should be related to synchrotron emission.

3.3.2 Benchmarks and complete treatment

A few benchmark scenarios

As discussed in Section 1.1.3, the Milky Way is the galaxy we know in furthest detail, still the determination of its DM halo profile is not a simple task.

One of the uncertainties in implementing results from N–body simulations regards the interplay between dark matter and the baryonic components of the Galaxy; in particular, the formation of the supermassive black hole (SMBH) at the Galactic center could have strongly modified the initial DM profile. The adiabatic growth of a black hole at the center of a singular halo profile leads to the accretion of a very dense DM spike around it [231]. Although this picture requires tuned initial conditions [232] (SMBH seed very close to the center of the dark matter distribution and slow adiabatic growth), it is actually not excluded and, if the spike is formed, it can be completely destroyed only in a major merger event, unlikely in the recent past of the Galaxy. The picture sketched in [231] and [232] has been further refined in [233], where a time-evolution analysis of the cusp formation is performed, including the effects of self annihilations, scattering of dark matter particles by stars, and capture in the black hole.

The presence of relatively large overdensity in the Galactic center region is an essential ingredient for a sizable WIMP dark matter signal at any of the wavelengths we will consider in our treatment. We follow the analysis in [233] and focus our attention on two distributions obtained from the evolution of a NFW profile [27]: in the first (hereafter labeled N_{sp}) we include the formation of a density spike around the SMBH only, while the second profile (hereafter labeled A_{sp}) is obtained by taking into account the deepening in the Galactic potential well generated by the slow adiabatic formation of the stellar component in the inner Galaxy, as well as that of the SMBH. In this second case the stellar component itself leads to a steepening of the halo profile from $\rho \propto r^{-1}$ into $\rho \propto r^{-1.5}$ [48]; this stands as a limiting case among

the series of results that have been obtained in the literature, as mentioned in Section 1.1.3. For both the N_{sp} and A_{sp} profiles the effect of self annihilation triggers the density in the innermost region, with the final shape being fixed by the value of the ratio $(\sigma v)/M_\chi$ [233]. There is therefore in general a non–linear dependence of the WIMP DM source, see Eq. 3.1, on the cross section (we have implemented such dependence in our analysis using scaling laws derived from either results given in [233] or further sample cases kindly provided by the authors of [233]).

Our benchmark DM profiles are shown in Fig. 3.5, together, for comparison, with the NFW profile and the "spiky" profile obtained implementing the original procedure outlined in [231]. Sample values for the WIMP mass and the annihilation cross section are chosen here such that the multi–wavelength constraints are not violated (verified a posteriori in section 3.3.3).

For what concerns the source spectrum in Eq. 3.1, we do not focus our discussion on specific WIMP models, but rather refer to a generic WIMP of given mass M_χ and annihilation cross section σv dominated by one single annihilation mode. If the DM annihilation into fermion is not suppressed, quarks give often the dominant branching ratio. This is the case for a gauge boson WIMP, such as the antiperiodic gauge field in [108], and for a Majorana fermion like the lightest neutralino in supersymmetric extension to the Standard Model. For this reason we choose as a benchmark annihilation mode a quark–antiquark pair, giving raise to soft spectra of secondary particles mainly through the hadronization into pions (charged or neutral) and their subsequent decay, see Fig. 3.4a.

The case of a leptonic final state, such as $\tau^+ - \tau^-$, is rather different since much harder spectrum is produced. We consider the $b - \bar{b}$ and $\tau^+ - \tau^-$ as limiting cases of a much more generic WIMP scenario.

To start our discussion on multi–frequency constraints on the GC as a WIMP DM source we first focus on three benchmark cases. Properties of the model are listed in Table 3.1 and regard the particle physics setup as well as the dark matter profile and its reshaping by the baryonic component in the Galactic center region and the assumptions on the magnetic field profile, whose relevance is illustrated in what follows in the discussion of propagation.

To model the propagation of electrons/positrons at the Galactic center, we need to consider two regimes. Outside the accretion flow, i.e. at radii greater than the accretion radius $R_{acc} \sim 0.04$ pc, the electrons/positrons, injected by dark matter annihilations, lose energy in place through radiative processes and their equilibrium number density is simply given by Eq. 3.13 (we will now include all relevant radiative processes).

For $r \leq R_{acc}$, the physical picture is as follows: The dark matter annihilations inject e^+ and e^- at a given radius of injection R_{inj}; then two competitive processes take place. On top of the momentum loss due to radiative processes, electrons and positrons gain energy in the adiabatic compression due to the plasma flow onto the central BH. The propagation equation Eq. 3.10

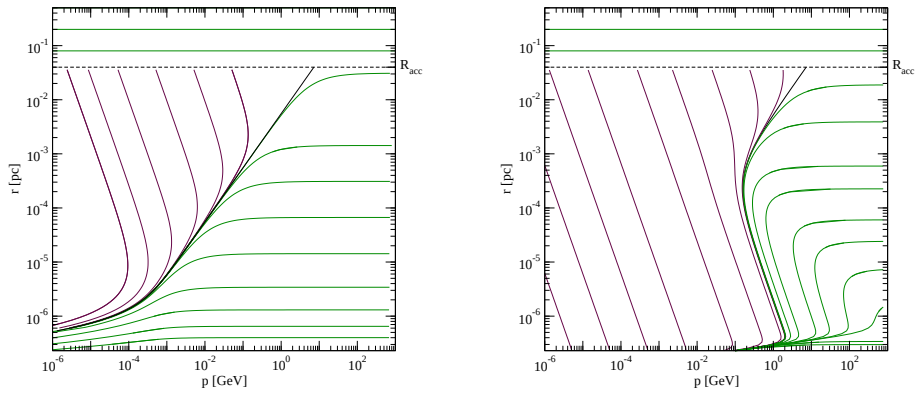

Figure 3.6: Electron/positron trajectories in the plane radius versus momentum for the equipartition (*Left Panel*) and reconnection (*Right Panel*) magnetic fields. Far from the turning points, synchrotron loss is dominant in green trajectories, while adiabatic heating takes over in violet trajectories. The black solid line represents the curve along which the $e^+ - e^-$ accumulate since the two effects balance each other. The dotted line is the accretion radius $R_{acc} = 0.04\,pc$, where advection is assumed to stop.

admits an integral analytic solution only in case synchrotron emission is the dominant radiative loss process and the $e^+ - e^-$ are in the ultra–relativistic (or non–relativistic) regime. The solution takes the form [208]:

$$f(r,p) = \int_{R_{acc}}^{r} dR_{inj} \frac{Q(R_{inj}, p_{inj}(r,p,R_{inj}))}{v(R_{inj})} \Big(\frac{R_{inj}}{r}\Big)^{4C_\alpha} \Big(\frac{p_{inj}}{p}\Big)^4 \tag{3.19}$$

where $C_\alpha = (2-\alpha)/3$ with α being the exponent in the power law scaling of the radial infall velocity $v \propto r^{-\alpha}$, i.e. $\alpha = 1/2$ in case of potential dominated by the central BH, see Eq. 3.12. The momentum p_{inj} is the initial momentum of an electron injected at R_{inj}, arriving at position r with momentum p. Outside of the ultra–relativistic approximation, Eq. 3.10 can be solved numerically through a change of variables that recasts the original partial differential equation (PDE) into an ordinary differential equation (ODE). This is defined by a solution of the associated homogeneous equation; the characteristic curve related to the latter is

$$\frac{dp}{dr} = \frac{\dot{p}_{syn}(r,p) + \dot{p}_{adv}(r,p)}{v(r)} \;\;,\;\; p(R_{inj}) = p_{inj} \tag{3.20}$$

which describes the trajectory of the electrons in the plane radius versus momentum, where

$$\dot{p}_{syn} = \frac{4}{3} c\,\sigma_T \frac{B(r)^2}{8\pi} \frac{E\,p}{(m_e c^2)^2} \quad , \quad \dot{p}_{adv} = -\frac{1}{3r^2}\frac{\partial}{\partial r}(r^2 v)\,p\,. \tag{3.21}$$

The solution of Eq. 3.20 is shown in Fig. 3.6 in the plane (p,r), in the case of equipartition (left panel) or reconnection (right panel) magnetic field (see

Fig. 3.3). In the first case the synchrotron loss dominates at high energies, while the advection gain takes over at low energies; electrons accumulate on the trajectory separating the two regimes (black curve in the figure). Since approaching the BH, the scaling in radius of the synchrotron loss is faster than the advection gain, $\dot{p}_{syn} \propto r^{-5/2}$ versus $\dot{p}_{adv} \propto r^{-3/2}$, the advection dominated region becomes smaller and smaller and disappears for radii very close to the BH horizon. As stated above, in the region with $r > R_{acc}$ we neglect the advection and thus the trajectories are just horizontal lines.

Quite similar is the electron/positron flow in the case of a reconnection magnetic field. Since now the magnetic field is smaller, the advection dominated region becomes larger. The line along which electrons accumulate is modified accordingly to the shape of the magnetic field plotted in Fig. 3.3a.

We would assume a magnetic field which is constant in the accretion region, see again Fig. 3.3a, advection basically dominates throughout the plane and there's no region of accumulation. Moreover electrons could be accelerated at energies greater than M_χ, an effect not possible in the previous cases in which the propagation of electrons with energy ≥ 10 GeV becomes dominated by the synchrotron loss at all radii.

We can then solve the propagation equation Eq. 3.10 on these trajectories, reducing the PDE to a linear ODE that admits a standard integral solution:

$$f(r,p) = \int_{R_{acc}}^{r} dR_{inj} \frac{Q(R_{inj}, p_{inj}(r,p,R_{inj}))}{v(R_{inj})} \exp\Big(\int_{R_{inj}}^{r} dr' \frac{h(r', p_{inj}(r,p,r'))}{v(r')} \Big) , \tag{3.22}$$

where $h(r,p) = p^{-2} \frac{\partial}{\partial p} (\dot{p}_{syn}(r,p) p^2)$. In the ultra–relativistic limit Eq. 3.22 reduced to the form in Eq. 3.19.

Examples of the resulting electron/positron equilibrium number density are plotted in Fig. 3.7a. We can see that the effect of the advection is to drive low energy electrons to higher energies, where synchrotron loss is dominant. Thus there is a peak in the distribution corresponding to the curves of momentum accumulation in Fig. 3.6. Note that in the case of equipartition magnetic field, the accumulation flow is much more efficient with respect to the reconnection case, or, in other words, there is a wider region of the initial condition (p_{inj}, R_{inj}) for a point of accumulation (p, r), and thus more electrons contribute. For this reason the peak in the density are more pronounced in the equipartition case. In Fig. 3.7a we plot for comparison the electron/positron equilibrium number density obtained neglecting the effect of advection. The synchrotron losses dominate until very low energies (and not too small radii) where ionization takes over (see Fig. 3.2a) and the distribution becomes flatter.

Fig. 3.7b gives a feeling for the radial reshaping of synchrotron signals due to advection effects. We plot the synchrotron luminosity, see Eq. 3.5, per unit logarithmic interval $j_{syn}\, r^3$, at the wavelength of 90 cm and for the three benchmark models in Table 3.1. There is a sharp jump in the

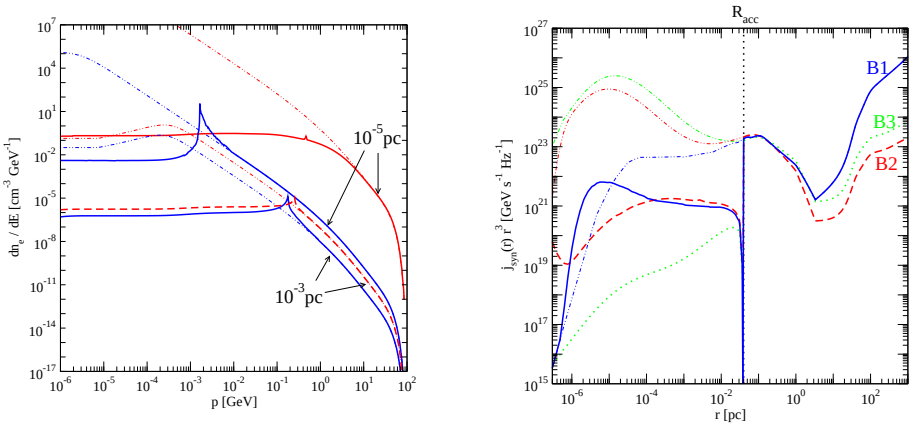

Figure 3.7: *Left Panel:* Electron/positron equilibrium number density at two given radii for the benchmark models B1 and B2 (colors and line-styles as in the previous figures). In the dash–dotted lines the effect of advection is neglected. *Right Panel:* Synchrotron luminosity per unit logarithmic interval $j_{syn}\, r^3$ at 90 cm for the three benchmark models. The sharp transition is in correspondence to the accretion radius $R_{acc} = 0.04\, pc$, where advection starts. In the upper dashed–dotted curves the effect of advection is neglected.

emissivity at the accretion radius R_{acc} since we have assumed a sharp transition between the two propagation regimes; in a more realistic model we would find a slightly smoother behavior without, however, the predictions for signals being significantly affected. At this frequency the source is rather extended, as already pointed out with the approximate scalings in Section 3.3.1. Actually, advection reduces even further the signal from the innermost region. Indeed at large wavelengths the synchrotron power peaks at low energy, while advection shifts electrons from low to high energies. This effect is more evident for constant and reconnection magnetic fields where the region in the plane (p, r) dominated by advection is large. For shorter wavelengths, the advection effect becomes less and less important since the synchrotron power peak shifts to high energies and thus into the region of the plane (p, r) in Fig. 3.6 where the synchrotron losses are dominant.

Points sources or extended sources?

Indirect detection of dark matter through the identification of a photon excess is not a straightforward task. There are essentially two types of signal for such flux: spectral signatures or signatures related to the morphology of the source. Regarding the spectral signatures, prompt annihilation into monochromatic photons is the most favorable case, however it is not guaranteed in a generic WIMP model [200]. On the other hand, signals with continuum energy spectrum could be in general mimicked by standard as-

trophysical sources. The spatial structure of the DM source, in case this is extended, could be an equally powerful way of disentangling the source from an environment in which other astrophysical sources are present. One often has to face the problem that although the WIMP source is extended, it cannot be experimentally resolved. In the following we want to show that this is not the case at the radio frequencies, since as expected from the approximate results in Section 3.3.1 the DM source may be very extended.

At radio frequencies, there are configurations for the parameters in the model for which synchrotron self-absorption is a relevant effect [206, 207, 208] and we include it in our analysis. In [208], it was shown that, on the other hand, we can safely neglect synchrotron self-Compton effects. For the signal in the UV and soft–X band, we need to take into account the photoelectric effect on the interstellar dust; this is an effect taking place mostly outside the region of emission hence we can model it a posteriori through an attenuation factor.

The synchrotron self–absorption effects relies on the fact that the emitted synchrotron radiation could be reabsorbed by the radiating electrons along the line of sight as described by Eq. 3.7. Being $\alpha(\nu, s, \theta)$ the synchrotron self–absorption coefficient, see e.g. [194], the quantity which is useful to estimate the relevance of the absorption effect is the optical depth:

$$\tau_\nu(\theta) = \int_{los} ds\, \alpha(\nu, s, \theta) \ . \tag{3.23}$$

In physical configurations leading to $\tau \gtrsim 1$, the synchrotron self–absorption effects cannot be generally neglected. In Fig. 3.8 we plot the optical depth along three different lines of sight for the benchmark models B1 and B2. As we can see, the absorption effect is relevant only along the lines of sight pointing towards the very central region. This is due to the fact that the probability of the radiation to be reabsorbed is related to the compactness of the source. Thus in general we expect negligible effects for shallow profiles. The scaling of absorption with frequency, in general, takes the approximate form: $\alpha(\nu, s, \theta) \propto j(\nu, s, \theta)\, \nu^{-5/2}$ [194]. More precisely for the benchmark models, we find numerically that absorption modifies by a factor O(1) the flux associated to observations of the inner region in the radio band, while it is irrelevant at larger angles and frequencies.

To study the angular profile of the photon source induced by WIMP annihilations, we define as ideal radiation intensity $I(\theta)$ the signal in a detector with an infinite angular resolution. For γ–rays, the spatial extension is completely fixed by the halo profile, i.e. by the dimension of the DM source. For synchrotron emission, on the other hand, it is affected by many ingredients, both related to the dark matter properties, to the magnetic field shape, and to the frequency of observation, as we can see from Eq. 3.16. In case synchrotron loss is not the dominant radiative loss, also gas and starlight spatial distributions contribute to set the shape of the angular profile of the

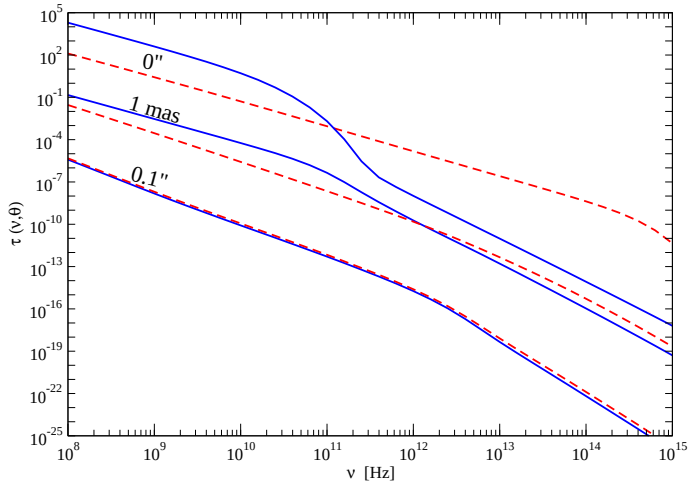

Figure 3.8: Optical depth versus frequency for three different lines of sight, in the benchmark models B1 and B2 (same line styles and colors of previous figures).

signal. We expect from the approximate treatment the radio–band signal to become wider than that in the γ–ray band, while in the X–ray band the need of a very large magnetic field shrinks the signal to a region which is much smaller than the size of the DM source. This is confirmed in Fig. 3.9a, where we plot the intensity as a function of the angular off–set from the GC, for the benchmark models B1 and B2 in Table 3.1 at the radio, X and γ–ray bands, normalizing each of the fluxes to unity to better understand the relative spatial extension. The difference in the spatial extension between the two benchmark models is essentially given by the halo profiles, since the A_{sp} profile leads to a more narrow signal than N_{sp}.

In a real observation, the detected angular profile is a combination of the intrinsic profile shown in Fig. 3.9a and the experimental resolution, as described by Eq. 3.6. In Fig. 3.9b we plot again the WIMP induced emissions for the benchmarks models B1 and B2, now filtered over a typical angular resolution. For the 90 cm signal, we take a typical resolution achievable by VLA, namely FWHM=$20''$ [234]. For the X–rays emission we consider the Chandra point spread function, i.e. PSF=$0.5''$ [219]. Finally in the γ–ray case, the signal is integrated over 0.1° that is a typical PSF for both the Fermi gamma-ray space telescope (FGST), formerly named GLAST, [235] and the current generation of ACT [168, 166]. The synchrotron emission in the X–band is very narrow and thus impossible to be resolved. In case of a very cuspy profile, like A_{sp}, the source could be resolved only by radio observations, while for the N_{sp} profile the source could be detected as diffuse both in the γ–ray and radio bands.

In Fig. 3.10a we plot the radiation intensity for the benchmark model B1 at four different frequencies. As expected, the size of the source becomes

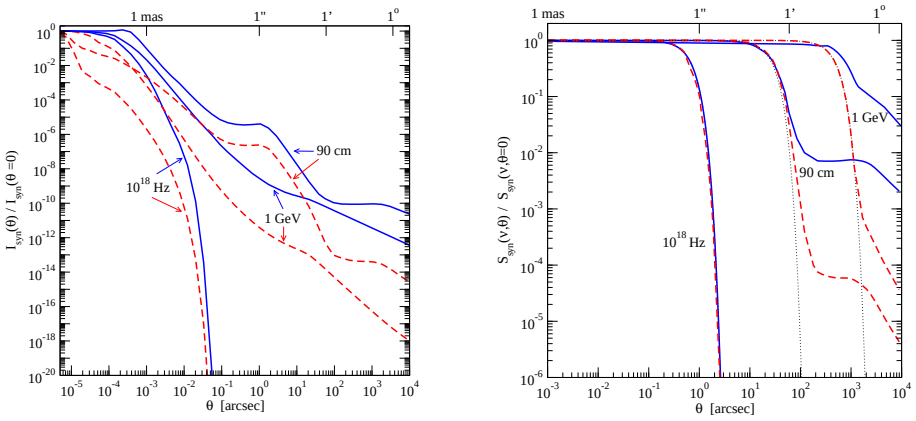

Figure 3.9: Normalized radiation intensity in the radio, X and γ–ray bands for the benchmark models B1 and B2. In the *Left Panel*, an ideal infinite angular resolution is considered, while in the *Right Panel* the intensity is filtered over typical angular resolutions: 20 arcsec at 90 cm, 0.5 arcsec at 10^{18} Hz, and 0.1° at 1 GeV. Dotted lines are the related experimental angular profiles of a point-like source, as modeled by a Gaussian detector response.

smaller going from radio to infrared wavelengths. In Fig. 3.10a, we show also the angular resolution of the current or near–future experiments in the radio (VLA [234] and EVLA [236]), mm and sub-mm (ALMA [237]), infrared and NIR (VLT [238]) bands, relative to the wavelength scale plotted on the right-hand side. In the first two cases the WIMP source appears extended, while going to higher frequencies it becomes a point source.

In Fig. 3.10b, we show the effect of varying the magnetic field on the synchrotron intensity at 90 cm, for the benchmark models B1 and B2, but looping over the magnetic field shapes shown in Fig. 3.3a. Note that the choice of magnetic field differs only inside the accretion region $\theta_{acc} \sim 1''$. The choice of equipartition magnetic filed gives the brightest signal, while the constant magnetic field the faintest. At this wavelength and for typical angular resolution of current detectors, the contribution from the region $\theta < 1''$ is never dominant, hence the choice of the magnetic field is essentially not relevant. The fact that at the intermediate angular scale the prediction of the two models coincides reflects just the choice of normalizing their radio emissivity to the tightest upper bound in the radio band, i.e. $S_\nu \leq 0.05$ Jy at the frequency $\nu = 408$ MHz [211].

For a given magnetic profile, the higher the energy for the radiating electron or positron, the higher the frequency at which the synchrotron power peaks; thus a hard $e^+ - e^-$ spectrum emits more efficiently at short wavelengths, while a soft spectrum at long wavelengths. In Fig. 3.11a we plot the angular intensity of the synchrotron signal in the radio, NIR, and X–bands for benchmark model B1 and B4, i.e. the same of B1 except for assum-

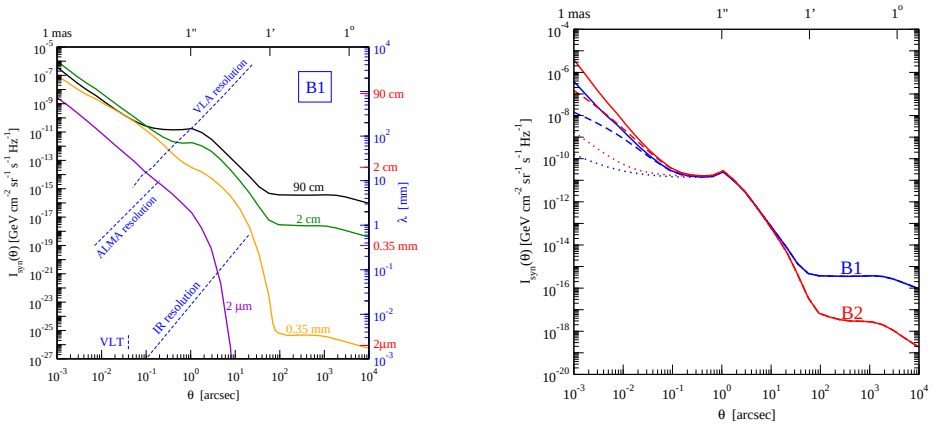

Figure 3.10: *Left Panel:* Angular profile of the synchrotron radiation intensity at different frequencies for the benchmark model B1. Experimental angular resolution in the radio and infrared bands are also shown (blue dashed lines) with the wavelength units displayed in the scale on the right-hand side of the plot. *Right Panel:* Angular profile of the synchrotron radiation intensity for the benchmark models B1 and B2 at 90 cm, but varying the magnetic field according to the three radial profiles in Fig.3.3a (same line styles).

ing $\tau^+ - \tau^-$ as dominant annihilation channel rather than $b - \bar{b}$. We find that B4 is significantly brighter than B1 at high frequencies. Note also that the spatial extension at such frequencies depends significantly on the WIMP annihilation final state.

Finally we turn to the uncertainty on the dimension of the signal stemming from the dimension of the source itself. In the case of signals at radio frequencies the scale at which is relevant to model the DM density profile to derive a definite prediction correspond basically to the angular resolution of the observation itself, i.e. $\theta \gtrsim 1''$. In Fig. 3.11b, we plot the benchmark model B1 at 90 cm, varying the dark matter profile and find how dramatically the signal can change. Note that the reason why the result with the NFW profile or the N_{sp} profile are essentially equivalent is the large value of the ratio $\sigma v/M_\chi$ for the benchmark model under consideration, which is flattening out the N_{sp} profile.

3.3.3 Results: multi–wavelength constraints and perspectives

In the previous Section, we discussed how intensity and spatial extension of the signal depend on parameters involved in the prediction for the multi–wavelength spectra. We implement now this general analysis to derive quantitative constraints. In Section 3.2.1 we listed available data–sets on the GC relevant in our analysis; since it is unlikely that any of them comes in connec-

tion to a DM signal, we will extract upper limits only. It's not straightforward to select a uniform exclusion criterion for all the measurements. We decide to compare the DM induced flux with the most constraining data–point in any given wave–band. To some extent, this is a conservative approach, since each experimental point is considered to be independent and no correlation analysis implemented. In the next decade, new telescopes, as well as new cycles of observations with experiments already operative at present, will allow to place even tighter constraints on WIMP parameter space, or, hopefully, find evidence for a DM signal. We will focus, in particular, on two classes of γ–ray telescopes, namely, the satellite detector FGST [235] which will be in orbit in a few months, and the next-generation air Cherenkov telescope CTA [239], and discuss the relevance of new observations at radio frequencies by the VLA project [234].

Synchrotron emission versus radio, infrared, and X-ray data

As summarized in the Section 3.2.1, rather accurate measurements of the radio and infrared emission of the source associated to the central SMBH are available. Both the spectrum and the pattern in size of this source cannot be associated to synchrotron emission from DM annihilations. Typically, observations of Sgr A* have been obtained with instruments with very good pointing accuracy and small angular acceptance. On the other hand, WIMP annihilations give rise to radio signals on a much larger angular size. It follows that, in general, it is incorrect to directly compare the total radio luminosity of the DM source with the luminosity extrapolated from the available Sgr A* observations. A more accurate way of proceeding is to compute, for each model and each data–point, the DM–induced synchrotron intensity within the region corresponding to the angular resolution of the telescope, i.e. mimicking a Gaussian response of the detector with θ_d in Eq. 3.6 (or a Gaussian elliptical response with two different θ) as appropriate for each measurement.

In Fig. 3.12a we show measured intensities (or upper limits) for Sgr A* ([210], [212], [217]) together with the DM synchrotron luminosity $L(\nu)$ integrated over the whole GC region, say, e.g., a sphere of radius corresponding to an angular size of about 1°, and divided by $4\pi\, d_0^2$, where d_0 is the distance to the GC (solid, dashed, and dotted lines, respectively, for benchmark models B1, B2, and B3, spanning the whole range of frequencies shown in the plot). As we just stated, this is not the quantity which should be compared to radio data; would one make such a connection, i.e. implicitly assuming that the DM source is point-like rather than extended, the inferred upper bounds would be grossly overestimated. We select instead five data-points (plus one in the infrared), each corresponding to measurements with different angular resolutions, and plot, in a small interval around the corresponding frequency, intensities towards the GC, treating now the signal as an extended source

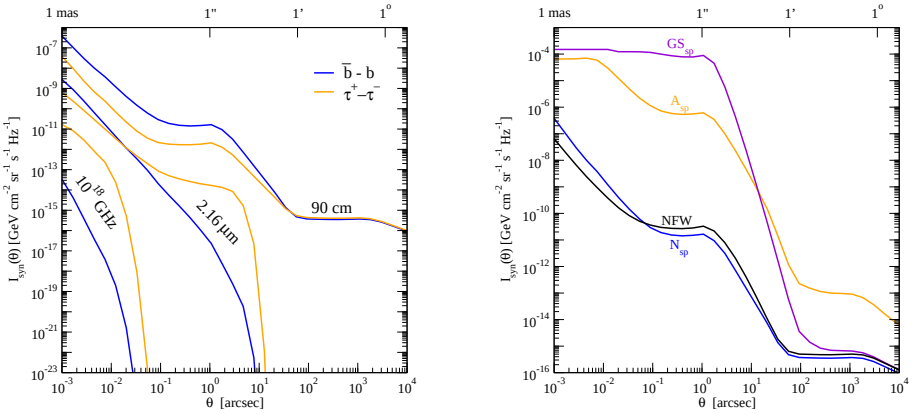

Figure 3.11: *Left Panel*: Angular profile of the synchrotron flux intensity for the benchmark model B1 and B4 (i.e. the same of B1 except for assuming $\tau^+ - \tau^-$ as dominant annihilation channel). We show the signal at different wavelengths, namely, in the radio, NIR, and X–ray bands. *Right Panel*: Angular profile of the synchrotron flux intensity at 90 cm for the benchmark model B1, but varying the DM halo profile.

filtered by the telescope angular response. As expected, the strongest constraint in the radio band comes from the measurement at the lowest available frequency [211] and the value of the cross sections for the benchmark models have been tuned to match this upper limit. This is also the measurement we will refer to, when combining constraints from different frequencies to the multi–wavelength DM spectrum in Figs. 3.15 and 3.16 below.

The intrinsic dimension of the DM synchrotron source at radio frequencies suggests that observations covering a wider field of view could set relevant constraints as well. We consider the map of the Galactic center at λ=90 cm obtained by [216], assembling different VLA observations. It is a $4^\circ \times 5^\circ$ image, with a resolution of 43" $\times$ 24", thus resolving Sgr A, the complex radio–source present at the GC and composed by Sgr A*, the supernova remnant Sgr A East, and the spiral structure Sgr A West, but not Sgr A* itself. The background noise level is about 5 mJy/beam. In Fig. 3.12b we plot the radial profile of the DM signal as it would be reported in a map with the resolution of [216] and detected by an observation with a resolution of 4.3", like in the Sgr A* survey of [211]. The Sgr A source is not spherically symmetric and its angular profile cannot be accurately reduced to a radial profile; in Fig. 3.12b we give just a schematic representation of the angular shape of the signal reported by [216]. We find that the limit on DM models one can deduce from Sgr A data is less stringent than the constraint inferred from Sgr A*. At large angles, however, the DM signal is comparable to the background noise level, in particular, in the case of the N_{sp} profile. As mentioned above, such noise level is extrapolated in [216],

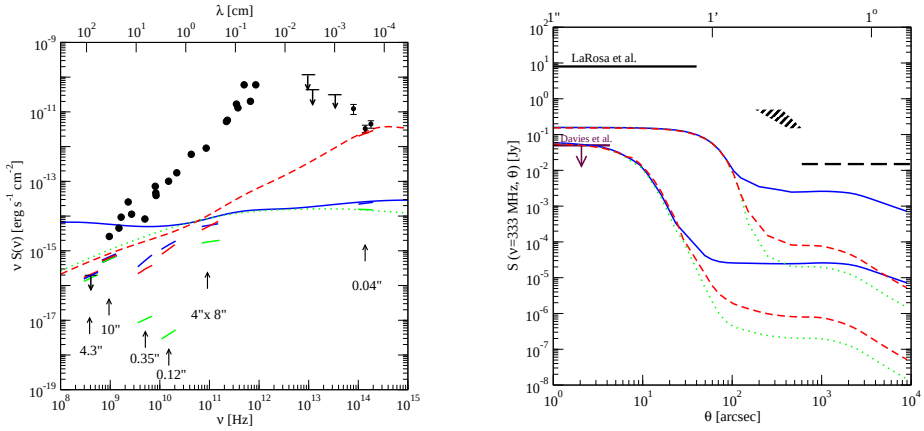

Figure 3.12: *Left Panel:* Sgr A* luminosity in the radio and infrared bands (black points) compared to the synchrotron radiation induced by DM annihilations in the benchmark models B1, B2, and B3. For the latter, portions of spectra integrated over the experimental angular resolutions around six frequencies are shown. The lines spanning the entire range of frequencies are the spectra integrated over the whole GC region. *Right Panel:* Spatial profile of the DM synchrotron signal for the benchmark models B1, B2, and B3. In the upper curves the angular resolution is 43" × 24", while in the lower curves it is 4.3". We show together the experimental limits related to the Galactic center region derived by [216] and to Sgr A* by [211].

assembling observations with different resolutions. It is not the best achievable in VLA observations today, of the order of $\sim 1\,\mathrm{mJy}/\sqrt{\mathrm{hour}}$ at 90 cm [234]. New wide-field observations could indeed lead to tighter constraints on DM models, as we will be discuss below.

In Fig. 3.12a we plot three measurements of the NIR luminosity of Sgr A* in the quiescent state [217], plus three upper limits derived in [212], and the DM–induced signal for the three benchmark models. We discussed in some detail how the angular size of the source shrinks rapidly going to higher frequencies. For the halo profiles we consider in our analysis, already in the NIR the DM source would appear as point–like, even with a detector with excellent angular resolution, such as a size of tens of mas achievable by VLT [240, 241]. Indeed, one can see that the estimate of the signal computing $L(\nu)/(4\pi\, d_0^2)$, or $S(\nu)$ integrated over the appropriate angular size, essentially coincide. Measurements are not far above from the estimated DM luminosities, especially for the benchmark model B2, for which this limit is comparable to the radio limit. We will derive limits on WIMP masses and cross sections considering the tightest NIR limit, namely, the measured emission in the K_s band ($2.16\,\mu m$).

Significant synchrotron emission at even higher frequencies is expected in the case of very large magnetic fields close to the central black hole, as in the equipartition and reconnection magnetic field models we are considering.

For the flux emitted in the UV and soft–X band, we need to take into account the attenuation due to the photoelectric effect on the interstellar dust. We model this effect scaling down the emissivity of Eq. 3.4 by the factor $exp(-N_H\,\sigma_{p.e.})$, where N_H is the electron column density [220] and $\sigma_{p.e.}$ is the photoelectric cross section [242]. In Fig. 3.13a, we plot the DM signal due to synchrotron emission, in the energy range where Chandra [219] has detected an X–ray source with position consistent with Sgr A*. The three benchmark models are considered, as well as the cases in which, keeping all the other parameters in the model fixed, the other choices for the magnetic field radial profile (see Fig. 3.3a) are implemented. To convert flux intensities into counts per unit energy and time, we use the Chandra effective area on axis reported in [243]. For a WIMP with mass of about 1 TeV (upper green curves) the peak in the emissivity is at galactocentric distances at which equipartition and reconnection magnetic fields differ only slightly, and thus the relative signals do not differ dramatically. In the case of the magnetic field flattened to a constant value (dotted green curve), on the other hand, synchrotron emissivity is sharply suppressed. For 100 GeV WIMPs (blue and red curves), the signal originates in a much smaller region, where equipartition and reconnection magnetic fields differ substantially, and the constant magnetic field cannot give a sizable signal. To better understand the dependence on the WIMP mass of the synchrotron signal, we show the X–rays spectrum in Fig. 3.13b for the benchmark models, and consider three WIMP mass scales.

Inverse Compton scattering and the emission in the X-ray and γ-ray bands

At X-ray frequencies and above, the dominant radiative process involving the $e^+ - e^-$ produced by WIMP annihilations can be inverse Compton scattering, rather than synchrotron emission. IC on the cosmic microwave background is peaked in the X–band, while that on the starlight has its peak in the multi MeV or even GeV region. The distribution of starlight in the Galaxy is highly non–uniform; its average energy density in the inner region is about $\epsilon_* \simeq 8$ eV cm^{-3} [223]. As a sample ansatz to make an estimate of the level of IC emission on starlight, we assume that such a value can be representative for the whole GC region and for simplicity we will make also the approximation of the starlight spectrum black–body shape of temperature $T_* = 0.3$ eV [223].

In Fig. 3.14, we plot the IC spectra on CMB and starlight, induced by WIMP–annihilations in the three benchmarks models. It is shown for a typical angular resolution of the current γ–rays experiments, i.e. 10^{-5} sr. We are considering such a large field of view since the IC signals have an angular shape which is significantly broader than the shape of the $e^+ - e^-$ source function. We can intuitively understand this feature from the fact that this

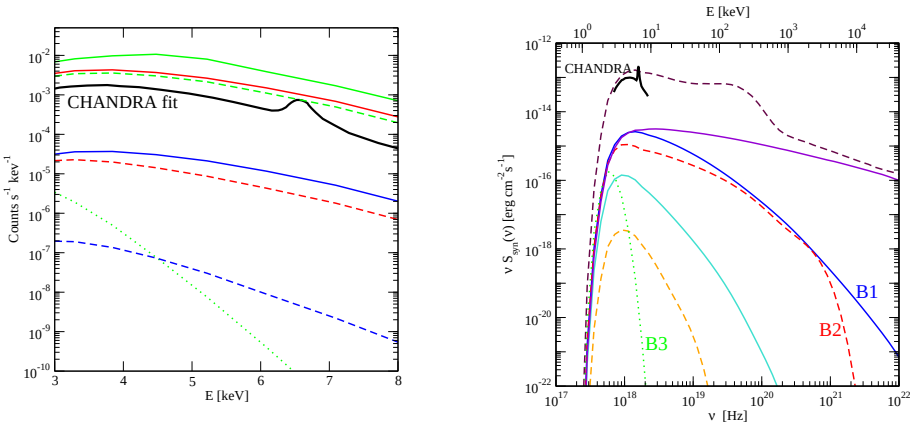

Figure 3.13: *Left Panel:* DM induced synchrotron flux in the Chandra energy range for the benchmark models B1, B2 and B3, but varying the magnetic field among the three different shapes of Fig. 3.3a. The black line is the fit to the Chandra measured spectrum. *Right Panel:* Synchrotron X–ray spectrum originated from dark matter annihilations in the benchmark models B1, B2, and B3, but varying the mass. The three cases considered are (from top to bottom): 1 TeV, 100 GeV, and 10 GeV. For constant magnetic field only the first case is shown since smaller masses cannot give a sizable spectrum.

emission comes mostly in connection to the $e^+ - e^-$ with largest energy at emission, and these in turn lose energy by synchrotron losses much more efficiently close to the GC, where magnetic fields are the largest, than in the outskirts of the GC region. It turns out that the angular shape for the equilibrium number density of high energy $e^+ - e^-$ is much broader than the gamma-ray flux from π^0 decays (which is the same as for the source function), and, of course, even more with respect to the shape of the synchrotron induced X-ray flux. For this reason, although for the plot in Fig. 3.14 the intensity associated to the IC on CMB is larger than the synchrotron intensity, when integrating over the angular resolution of the Chandra detector, the trend is reversed, and only in the case of constant magnetic field, with synchrotron emission in the X-ray band essentially negligible, comparing the IC flux to Sgr A* gives a tighter constraint. Analogously to what we did in the case of radio emission, it is worth checking whether data on a large field of view could be relevant. We compare the IC signal to the diffuse X–rays emission detected by the Chandra observatory: In the $17' \times 17'$ map of [221], some regions are selected and from them spectra of diffuse emission are extracted, removing events near points source and filamentary features. When combining constraints from different frequencies in Figs. 3.15 and 3.16 below, we compute the level of IC emission in such regions and extract upper bounds.

Similar arguments apply for the IC on starlight and the γ–ray limits. In-

deed for what concerns bounds associated to the point–like source detected by Egret at the GC (actually its position is controversial, see the next section), the limit associated to π^0 decay is more constraining than the IC limit. This is not true in general for the diffuse emission on the whole GC region, however we do not find any region in the parameter space in which tighter limits come in connection to this component. Note that the assumption we made on radial profile and energy spectrum for the starlight background are rather crude, and may deserve further study; refining them may lead to a slightly different conclusion, but it is unlikely that the general picture would be affected.

The emission from π^0 decays and the γ-ray band

Recently, observations by atmospheric Cherenkov telescopes detected a gamma-ray source in the direction of the Galactic center. In particular the H.E.S.S. collaboration ([165], [176]) has obtained an accurate measurement of the spectrum of the source as a single power law in the energy range between 160 GeV and a few tens of TeV, making the interpretation of the signal in terms of WIMP DM pair annihilations rather unlikely. H.E.S.S. has found evidence for a GC point–like source, namely, a source with an extension smaller than its PSF=0.1° and position compatible with Sgr A*, on top a diffuse γ-ray component [167]. In the case of cuspy dark matter halo profiles, one needs to compare against the central source only; the shallower the profile, the more efficient it becomes to extend the analysis and include the GC ridge as well (see, e.g., the discussion in [205]). The resulting limits for the benchmark profiles are plotted in Figs. 3.15 and 3.16.

The EGRET telescope mapped the GC in the energy range 30 MeV–10 GeV [163], detecting a flux within 1.5° of the GC. A few hypothesis for interpreting this flux in terms of a standard astrophysical source have been formulated; its spectral shape is even compatible with a component from WIMP DM annihilations [201]. On the other hand, the poor angular resolution of EGRET does not allow for a univocal identification of the source. In Ref. [164], using only energy bins above 1 GeV and a spatially unbinned maximum likelihood analysis, the authors argue that the Galactic center is excluded as the position of the source at 99.9% and the maximum likelihood location is at $l = 0.19$, $b = -0.08$. Thus they derive upper limits on the γ–rays flux from DM annihilations under the condition of no evidence of a point–source at the GC. Whether this is the correct approach is still under debate and only the FGST surveys will give a definitive answer. We derive more conservative but robust limits comparing with the EGRET source; would one follow the line of [164], the limits would be improved up to about a factor of ten. Except for very light WIMPs, the strongest constraint comes from the last data-point in the EGRET measurement, in the energy bin $4 - 10$ GeV.

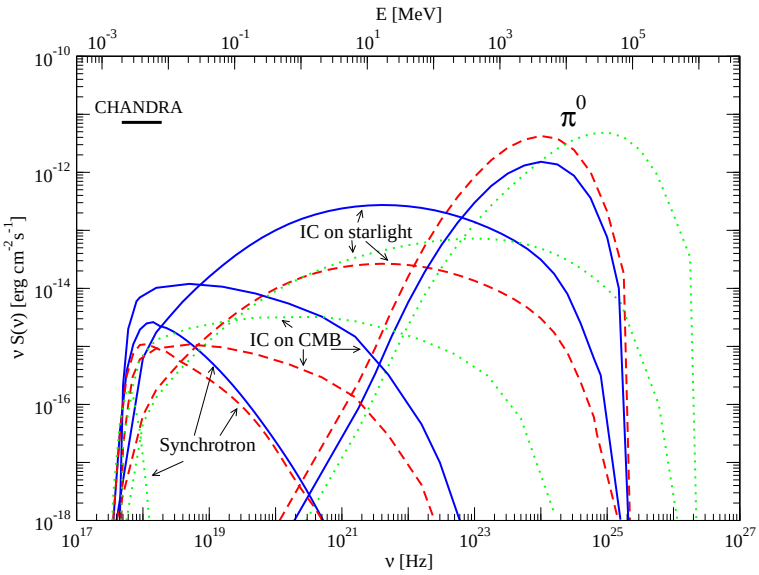

Figure 3.14: X–ray to γ–ray emissions induced by DM annihilations for the benchmark models B1, B2, and B3. All the four mechanisms of photon spectrum production considered in this Chapter give sizable signals. The flux intensities are integrated over a solid angle of 10^{-5} sr. The level of the diffuse emission detected by Chandra is also shown (black line).

Combined constraints on the WIMP parameter space

Having specified how individual constraints are implemented, we are now ready to discuss the global picture. We refer to a model independent scenario in which a WIMP model is labeled by the value of the WIMP mass M_χ and its total annihilation rate σv, both assumed as free and independent parameters. As for the benchmark cases, we discuss as extreme cases for the WIMP source functions, a soft spectrum configuration fixing to 1 the branching ratio in the $b-\bar{b}$ channel, and a hard spectrum setup when $\tau^+ - \tau^-$ is the dominant annihilation mode. Again, having specified the annihilation mode and the WIMP mass, injection spectra are fixed accordingly to simulation results with the PYTHIA package as implemented in DarkSUSY [96]. Reference models for the DM distribution in the GC region are the N_{sp} and A_{sp} profiles (with the second much denser than the first, hence with upper bounds on σv expected to shift dramatically). Finally, we loop over the three reference magnetic field radial profiles given in Fig. 3.3a.

In Figs. 3.15 and 3.16 we consider the four possible combinations of annihilation channels and halo profile. The Davies et al. radio bound does not depend on the magnetic field choice since, as we have seen above, the signal is generated mainly outside the accretion region. The same is of course true for the EGRET and HESS γ-ray limits. It is rather striking to see that the

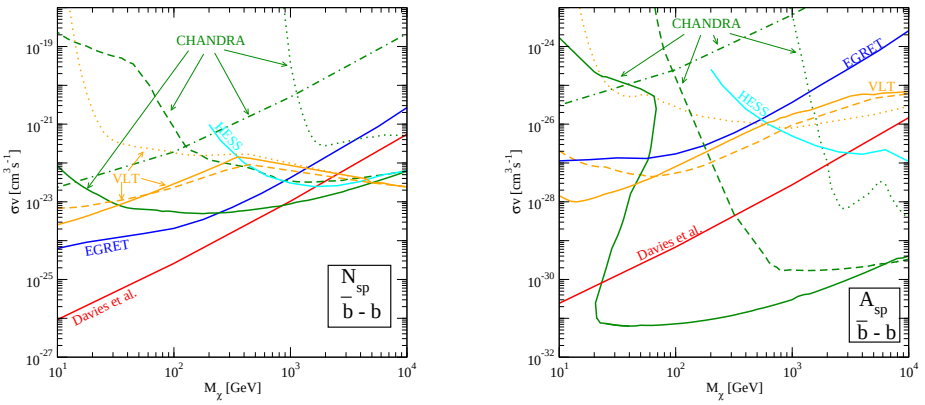

Figure 3.15: Upper bounds on the WIMP pair annihilation cross section as a function of the WIMP mass, assuming $b-\bar{b}$ as dominant annihilation channel. The *Left Panel* and *Right Panel* show the limits for, respectively, the N_{sp} and A_{sp} profiles; note the mismatch on the vertical scale in the two plots. The radio constraints from Davies et al., the limits from EGRET and HESS γ-ray measurements, and the bound from the X-ray diffuse emission as detected by CHANDRA (dashed–dotted line), do not depend on the choice of the magnetic field radial density profile. The constraints associated to the NIR and X-ray observations of Sgr A*, respectively, by VLT and CHANDRA, are shown for the three magnetic field models of Fig. 3.3a (using the same line styles).

radio limit is always tighter than the EGRET limit, with this trend getting enforced even more, the softer the spectra and the more cuspy the halo profile. Were we considering a DM profile obtained by implementing the original simplified procedure by Gondolo and Silk as response for the adiabatic formation of the central SMBH [231], we would find that essentially the whole WIMP parameter space is excluded, as in the original conclusions in Refs. [206, 207] (despite the fact that several ingredients in this analysis are refined and/or treated differently). The HESS limit becomes more stringent for heavy WIMPs, especially in the case of hard emission spectra. Unfortunately this is a regime in which other constraints take over.

VLT NIR limits depend to some extent to the magnetic field choice and show some non–trivial behavior. Consider the case of the $\tau^+-\tau^-$ final state. For very heavy WIMPs, and hence very energetic radiating particles in this hard emission spectra, the value of the magnetic field matching the peak in synchrotron emission is quite small (see Fig. 3.3b), corresponding to the region where we have assumed identical shapes for the profile of the three benchmark cases. Going to smaller masses, the energy at which the e^+-e^- distribution peaks becomes smaller, and thus the required magnetic field higher, approaching the value we assigned (by mere chance) to the central plateau in the constant magnetic field case (limits are coded in magnetic field using the same convention for line-type as in Fig. 3.3a); the emission

is particularly efficient and bounds are more effective with respect to the equipartition and reconnection magnetic field cases. At smaller masses the magnetic field matching the synchrotron peak becomes greater than the constant plateau and constraints are quickly relaxed. The same effect happens for the reconnection magnetic field, at even smaller masses. An analogous effect takes place for the $b - \bar{b}$ channel, but to a smaller extent due to the soft spectrum.

We have already discussed patterns of dependencies of the synchrotron X-ray signal with the magnetic field in many details. For moderate to large values of magnetic fields around the central BH, the limit from the detection of Sgr A* by CHANDRA tends to be the tightest in the WIMP parameter space, except if the WIMP mass is too small, the annihilation channel is too soft, or the density of WIMP very close to the GC is not large enough, i.e. if, in connection to one or more of these issues, we do not have enough high energy radiating electrons and positrons. The signal is generated in a very small region, where the DM profile depends on the ratio $\sigma v/M_\chi$, and hence the scaling of the flux with the cross section is not linear. In the case of the A_{sp} profile, this dependence is so strong that the limit can be double valued.

Finally, the dash-dotted line refers to the limit extracted from detection by CHANDRA of a diffuse X-ray background, when compared to the predicted IC emission on the CMB. It can be the tightest X-ray limit, however, it is never the strongest constraints in any combination of our reference setups.

In general, the request for the WIMP thermal relic abundance to not exceed the value of the mean DM density in the Universe as derived from cosmological measurements, fixes a lower bound on the total annihilation rate at zero temperature (the relic density scales approximately with the inverse of the pair annihilation rate; there are, however, cases when such correspondence is badly violated, the prime example being when coannihilation effects are present). The very tight constraints we have found in case of the A_{sp} profile should make very narrow, or even close, the allowed window in the WIMP parameter space. For the N_{sp} profile, on the other hand, the limits we have derived are much less stringent.

Projected constraints with upcoming observations

Indirect dark matter detection is one of the most ambitious objectives for new observational campaigns or new telescopes getting available in the near future, with the GC often being indicated as the prime observational target. We try to make here a projection on how significant could be the improvement with respect to the region of the WIMP parameter space already excluded in Figs. 3.15 and 3.16.

We mentioned that the radio bounds could become even stronger for wide field 90 cm observations of the GC region reaching a noise level which is significantly reduced with respect to the map constructed in [216], at

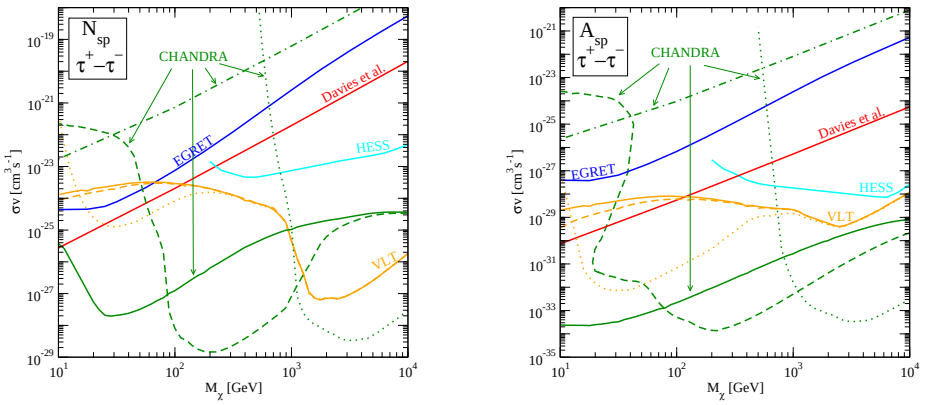

Figure 3.16: The same as Fig. 3.15, but taking $\tau^+ - \tau^-$ as the dominant annihilation channel.

least in case the intrinsic dimension of Sgr A in the radio band is not much larger than what is inferred from present observations. In Figs. 3.17 and 3.18 we sketch the case of a hypothetical observation with the VLA in its configuration with the worst angular resolution for spatial reconstruction, but with the maximal DM-signal to noise ratio, namely with FWHM=200" and a noise level of 0.1 mJy in 50 hours of observations (configuration D in Ref. [234])[4]. We are pointing the telescope at an angle of $50'$ with respect to the GC. The lower curves sketch the improvements in upper bounds which could be obtained in the case of presence of regions with no contamination from astrophysical backgrounds (3 σ noise level). This scenario corresponds to the most favorable case. Indeed a 90 cm diffuse emission at the GC was already detected [214, 215]. However, the poor angular resolution of the surveys (51 and 39 arcmin, respectively) does not allow to derive the spatial structure of the emission in the innermost region. In the GC image of [216], such emission does not seem completely isotropic and hence, from patches of the map with no background, we can extract tighter bounds (upper curves in Figs. 3.17 and 3.18) with respect to [214, 215]. Indeed, although the observations made with the Green Bank Telescope and reported in [215][5] have a comparable sensitivity, the associated image shows a smoother diffuse emission, due to the larger angular resolution, and the comparison between the WIMP signal and the noise level has to be performed at larger angles, where the DM emission is fainter. The real limit is probably standing in between the two extreme cases plotted in Figs. 3.17 and 3.18.

The space satellite FGST was launched June 11, 2008. The energy range

[4] The EVLA project [236], scheduled for 2013, should improve the continuum sensitivity, and consequently the WIMP constraint, by a factor of 2 to 40 with respect to VLA.

[5] Note that the magnetic fields considered in this thesis and plotted in Fig. 3.3 are consistent with the bound derived in [215] by the comparison of the detected diffuse non-thermal source and the expected synchrotron emission from GC cosmic rays.

of detection is approximately 100 MeV–300 GeV, with an expected sensitivity improved by a factor 100 with respect to EGRET. The PSF and the effective area at high energy are respectively 10^{-5} sr and 10^4 cm^2 (in the following we will consider the full energy dependence in these quantities as inferred from [235]; averaging over the angle of observation at which the GC stands with respect to the zenith of the detector are included as well, finding an effective exposure which is essentially reduced by a factor of 0.3). We have also assumed a 10% energy resolution, an exposure time of 5 years, and systematic errors of 5.2% [244]; the latter are relevant only at energies $<$ 10 GeV.

The next generation of ACT, the Cherenkov Telescope Array (CTA) project, is currently under development. The proposed energy range of detection is 10 GeV–100 TeV, thus overlapping and extending on the HESS range. The most dramatic improvement will be in the effective area, up to about 1 km^2 or even larger in extreme configurations, with highly reduced statistical errors. Based on the study in [239], we assume systematic errors to be $\sim$1%, the energy resolution at the level of 10%, and the point spread function equal to 10^{-5} sr. For an ACT, on top of astrophysical backgrounds, one needs to take into account the background from misidentified showers, i.e.:

$$\frac{dN_{sh}}{dE} = \frac{dN_{had}}{dE} + \frac{dN_{el}}{dE} \tag{3.24}$$

where $\frac{dN_{had,el}}{dE}$ are the spectra of the gamma-like showers from hadrons and electrons, respectively. We treat these components following [200], assuming 1% of misidentified hadron showers with respect to the total incident flux. We assume a total of about 250 hours for the exposure time (reasonable in 5 years of operation for CTA).

To estimate the γ–ray projected constraints in the plane DM mass versus annihilation cross section, we make an extrapolation of the point–like and diffuse astrophysical backgrounds detected by HESS over the whole energy range of interest, namely 1 GeV–300 GeV for FGST and 10 GeV–100 TeV for CTA, assuming single power law scaling for the fluxes. We consider two generic power law spectra $A_i E_\gamma^{-B_i}$, with $i = p, d$, one for the point–like GC source and the other for the diffuse gamma–ray emission in the Galactic center region, assumed to have a flat angular profile. We first generate a sample of A_i and B_i coefficients satisfying the condition $\chi^2_{red} \leq 1$ when compared to the data-sets from HESS observations [165] and [167]. Then, we simulate how this flux should be seen by FGST and CTA summing statistical and systematic errors in quadrature (we define the statistical error as the square root of the number of events in any given bin). Finally, we compute the best fits assuming as theoretical flux a dark matter contribution on top of a new two-component background $\tilde{A}_i E_\gamma^{-\tilde{B}_i}$. Among all the $\tilde{A}_i$ and $\tilde{B}_i$ coefficients allowed, we retain the case providing the smallest χ^2 and take as exclusion criterion $\chi^2_{red} > 3$, namely a flux not well fitted by the dark component plus

any viable astrophysical components. The χ^2 analysis is performed both on the energy spectra and on the angular structure of the flux. The angular bin size is fixed according to the PSF. For the A_{sp} profile, this last step is useless, since the dark matter signal is concentrated in the central angular bin (see Fig. 3.9), while for the less cuspy N_{sp} profile this procedure provides additional information. (The method we are implementing leads to analogous conclusions with respect to the treatment in [205], the main differences in the extrapolated limits stemming from the different halo profiles adopted and a different treatment of systematic errors.)

Results are shown in Figs. 3.17 and 3.18. In the same plots, shaded regions identify the models violating at least one of the constraints in Figs. 3.15 and 3.16 considering the weakest limit among the three cases with a different choice of the magnetic field radial profile, i.e. models that are *excluded* (at least within the rather general set of assumptions we are making regarding magnetic fields, treatment of electrons and positrons propagation, dark matter densities in the GC region, and spectral features of the yield from WIMP annihilations). The projected limit for FGST is always lying in a shaded region; those for CTA span modest portions of the parameter space which are not already excluded. One should consider, on one hand, that we may have been over conservative, since we derived these limits relying on extrapolations on both the energy spectra and the angular profile for the background astrophysical components, as well as without assuming any theoretical modeling of such astrophysical sources; with data at hand the picture may look slightly more favorable. On the other hand, this is indeed suggesting that, although the γ-ray band is the regime in which it is most straightforward to make the connection between a given dark matter model and the induced signal, it does not seem to be the energy range with the best signal to background ratios, at least in the case of the GC and of not very cuspy DM profile.

3.4 Other possible multi-wavelength sources

Various astrophysical systems have been analyzed in order to set constraints on the nature of the DM particles. To be exploited for this aim, they should possess an associated relatively high DM-induced flux and the possibility to disentangle the DM source with respect to background sources. The multi-wavelength approach we discussed in the case of the GC can be extended to other objects and, in the following, we sketch the most investigated cases in the literature.

3.4.1 Galaxy clusters

Clusters of galaxies are the largest bound structures in the Universe and their mass is dominated by the DM component. Therefore, they can be

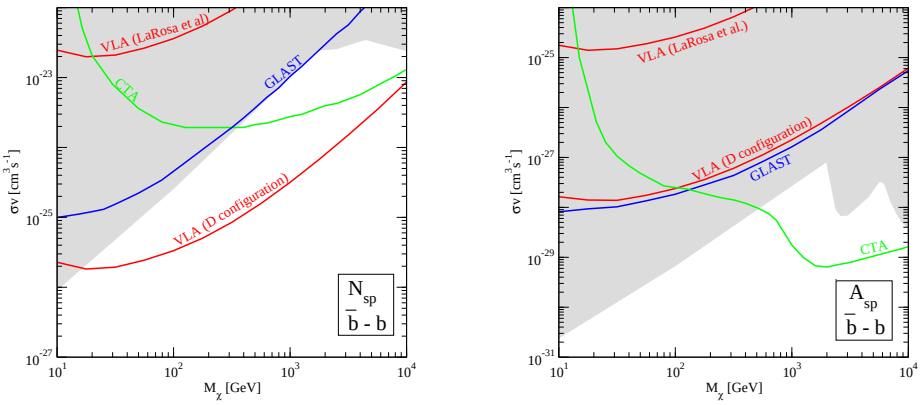

Figure 3.17: Projected exclusion limits from VLA, FGST (labelled GLAST) and CTA, in the plane WIMP annihilation cross section versus WIMP mass, in the case of $b - \bar{b}$ as the dominant annihilation channel. The *Left Panel* and *Right Panel* show the limits for, respectively, the N_{sp} and A_{sp} profile. The FGST and CTA projections are obtained combining an angular and spectral analysis as described in the text. The VLA limit arises from the comparison with the background noise level at 50 arcmin away from the GC. The upper curve is derived assuming a noise level as in [216], while the lower curve is computed considering the minimal noise achievable by VLA (D configuration). Shaded regions identify the models violating at least one of the constraints in Fig. 3.15 (considering the weakest limit among the three cases with a different choice of the magnetic field radial profile).

considered as natural targets for indirect signatures of WIMP annihilations. In the case of few nearby clusters, the DM induced flux could be possibly detected in multi-wavelength studies [188]. The majority of galaxy clusters is, however, too far to be probed by forthcoming experiments.

A detailed analysis of the DM distribution and of the induced multi-wavelength flux in the Coma cluster is performed in [188]. Depending on some assumptions for the structure of the intracluster magnetic field, the spectral and the spatial features of the Coma radio halo can be fitted by a WIMP-induced component. On the other hand, this model produce too faint emissions at other wavelengths. The FGST detector could, however, constrain the gamma-ray part of the spectrum in the next years.

In Ref. [245], they propose an explanation of the non-thermal hard X-ray emission from the Ophiuchus cluster in terms of IC scattering induced by WIMP annihilations. Assuming a quite low magnetic field (of the order of 0.1 μG), both the X-ray and the radio emissions can be reproduced. Again, the FGST surveys will be an important test for such a scenario.

In order to disentangle WIMP-induced signals from other astrophysical emissions, an ideal system would be a cluster with a clear spatial separation between the various matter components. The cluster 1ES0657-556 fits in this scenario (see the discussion at the end of Section 1.1.2). The microwave

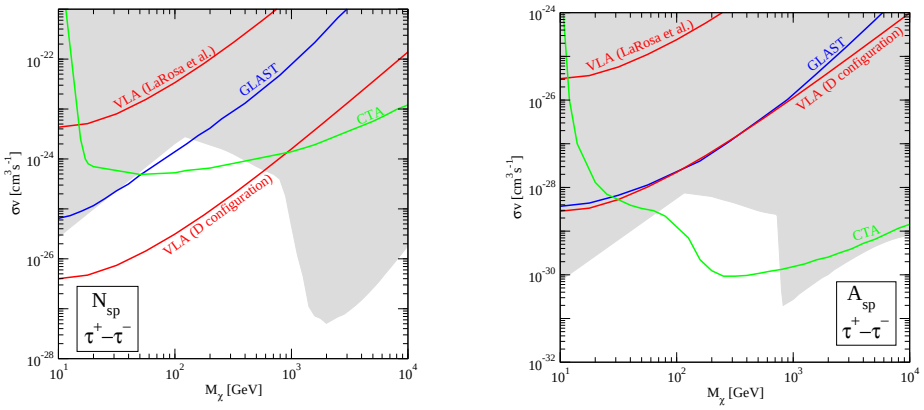

Figure 3.18: The same as Fig. 3.17, but taking $\tau^+ - \tau^-$ as the dominant annihilation channel.

observations of the SZ effect induced by DM annihilations in this cluster (compared to other multi-wavelength signals) can be another complementary way to test WIMP models [246].

3.4.2 Galactic DM clumps

The distribution and size of DM clumps embedded in the smooth large-scale galactic halo have yet to be precisely determined. WIMP clumps as synchrotron sources have been discussed in [247], in connection to their detectability in CMB experiments. A multi-wavelength perspective was adopted by [190], combining synchrotron and IC radiation signals. They conclude that the presence of galactic DM clumps can be significantly constrained through the search for its induced diffuse IC emission by the FGST experiment.

3.4.3 Dwarf spheroidal galaxies

Recently, dSph galaxies, populating the region around the Milky Way and M31, have been extensively investigated as possible targets for the observation of a WIMP-induced signature, with most of the studies dedicated to the gamma-ray component. In this respect, dSph galaxies share several nice features. They are DM dominated systems and the gas, dust and cosmic-ray components are highly subdominant. This implies that the related multi-wavelength spectra appear to be faint. Moreover, the predictions from N-body simulation concerning the DM halo profile can be considered more trustable than in the case of galaxies like the Milky Way, since baryons are not expected to play a crucial role. They are the closest DM dominated objects other than the Galaxy and the WIMP-induced emissions are generally considered brighter and more promising than, e.g., for clusters.

Moreover the known location makes the search well-defined, unlike the more ambiguous case of completely dark substructures.

Investigations of the multi-wavelength signals associated to WIMP annihilations in dSph Draco are performed in [189, 248]. In dSph galaxies, spatial diffusion can play an important role. The DM-induced synchrotron emission in Draco leads to a spatially extended structure, which has interesting consequences in the next-generation of radio telescope [189]. As in the case of the GC, depending upon assumptions on the magnetic fields, the diffuse radio emission from Draco can have a signal-to-background ratio larger than the gamma ray case.

The X-ray signal associated to IC scattering off CMB photons of $e^+ - e^-$ injected by WIMP annihilations in a few dSph galaxies is studied in [249]. They do not observe any excess, constraining the WIMP parameter space at a level comparable to gamma-ray observations of the same systems, although the result depends again on some additional assumptions.

The SDSS collaboration has been discovered a population of extremely low-luminosity satellite of the Milky Way. Recent measurements of the velocities of the stars in this faint objects indicate that they are DM dominated galaxies with a mass $\sim 10^7 M_\odot$ within their inner 0.3 kpc [250]. Their proximity and their large mass make these dSph galaxies as very promising targets for detecting an induced-WIMP signal. The case of the gamma-ray band has been investigated in [251]. One of their conclusions is that the expected flux can be significantly larger than that from previously known dSphs.

Chapter 4

A WIMP candidate from extra-dimensions

The SM cannot be likely considered as the final theory of particle physics. As already mentioned, it suffers of naturalness problems and does not account for the DM content of the Universe. Many extensions have been proposed, including, e.g., Supersymmetry, Little Higgs, and models with extra dimensions (ED). In this Chapter, we will focus on the latter. Models with the number of the space-time dimensions > 4 are non-renormalizable. Therefore, ED models are effective theories valid up to an ultraviolet cut-off scale. They have a strong theoretical motivation in quantum theories of gravity, namely string and M-theories, which consistent formulations requires the presence of extra-dimensions. A more phenomenological perspective has been, on the other hand, widely pursued as well. Indeed, most of the ED models have been introduced in the literature to solve the gauge hierarchy problem connected to EWSB, namely to suppress radiative corrections to the Higgs mass. DM candidates in ED could arise either from new degrees of freedom associated to the introduction of extra dimensions or from the extension of the particle content induced by the gauge group and matter representations of the theory BSM. One of the most investigated class of frameworks, embeds WIMPs as DM constituents of the Universe through a mechanism preventing the WIMP to decay by introducing a new unbroken discrete $\mathbf{Z}_2$ symmetry. All SM particles are assumed to be neutral under this symmetry, while the WIMP DM candidate is the lightest non-neutral state. Higher dimensional theories may fit into this picture: the lightest Kaluza–Klein particle (LKP) is potentially a good DM candidate in the class of ED scenarios in which a discrete symmetry makes the LKP stable.

In the next Section, we discuss possible solutions for the gauge hierarchy problem in ED frameworks. Section 4.2 is devoted to a list of examples of DM candidates embedded in ED models.

4.1 Extra-dimensions and Standard Model issues

Considering extension of the SM with one (or more) extra-dimension, the first question which obviously arises is: why is this ED unobserved?

One possibility is that only gravity propagates along the extra-dimension, while all the SM fields live in a 4D sub-space, i.e., a 3-brane. Models of this sort are generalization of the Arkani-Hamed, Dimopoulos and Dvali (ADD) model [252]. The relation between 4D and $(4+n)$-dimensional Newton constants is given by:

$$G_N^{(4)} = \frac{1}{V_n} G_N^{(4+n)} \quad . \tag{4.1}$$

where $V_n \sim R^n$, R and n are the volume, the size and the number of the extra dimensions, respectively. If the compactification volume is sufficiently large, the fundamental mass scale $M = (M_{Pl}R)^{-n/(n+2)} M_{Pl}$ (where $M_{Pl} = (G_N^{(4)})^{-1/2}$ is the 4D Planck mass) can be reduced down to the EW scale.

Another possibility is given by extra dimensions too small to be accessible so far at colliders. In this context, models with warped extra-dimensions are one of the most investigated framework for addressing the gauge hierarchy problem. The original idea of Randall and Sundrum (RS) [253] involves an exponential hierarchy arising from the background metric. Considering a 5D space-time, the AdS_5 metric considered by RS is:

$$ds^2 = e^{-2ky} \eta_{\mu\nu} dx^\mu dx^\nu + dy^2 \quad , \tag{4.2}$$

where k is the AdS curvature scale, $\eta_{\mu\nu}$ is the Minkowski metric, and y is the fifth dimension compactified on a line segment ($y \in [0, \pi R]$). In the first RS model, SM particles are confined to the IR brane, namely at $y = \pi R$. A generic mass M in 5D, including the Higgs mass, is rescaled down by the warp factor to $M\, e^{-\pi kR}$ on the IR brane, solving the hierarchy problem. This picture, however, leads to generic tensions with proton decay, flavor changing neutral current effects and neutrino mass. Many variants of the original setup have been developed in the last years.

According to the AdS/CFT correspondence [254], 5D warped models have a dual 4D interpretation in terms of a strongly-coupled conformal field theory (CFT). In this framework, EW symmetry can be dynamically broken with the Higgs arising as a composite pseudo-Goldstone boson from the strongly interacting sector (in a similar way as pions in QCD). At low energies it resembles the elementary Higgs, while its behavior at high energy is quite different. The Higgs mass is protected by an approximate global symmetry of the strongly interacting sector and the potential is only generated via quantum effects. Models of this sort can successfully address the flavor structure issue and pass EW precision tests (for a recent review, see, e.g., [255]).

A possible solution of the gauge hierarchy problem is provided by the so called gauge-Higgs unification (GHU) mechanism. If the SM Higgs bo-

son arises from the internal component of a higher-dimensional gauge field, the underlying higher dimensional gauge symmetry protects the Higgs by radiative quadratic divergences. EW breaking proceeds via the Hosotani mechanism (i.e., through a non-local Wilson line effective interaction) and the Higgs potential is finite to all orders (for a review on GHU, see, e.g., [256] and reference therein). From a model building point of view, the GHU mechanism requires to enlarge the SM gauge group.

In Ref. [111], a class of GHU scenarios in warped space is discussed. They consider in detail a realistic model, namely, the minimal composite Higgs model [257], whose gauge group is $SO(5) \times U(1)_X$. They show that, within the GHU construction, the predicted Higgs is heavier than the experimental bound, the EW precision observables can improve, and new vector-like quarks can be detected at LHC.

In flat scenarios, the simplest models are 5D theories with universal extra dimensions [258], namely theories where all the SM particles are promoted to bulk fields propagating in higher dimensions. They are particularly interesting from the DM point of view, as we will discuss in the next Section. Despite the simplicity of these models, however, UED theories do not shed any light on the EWSB mechanism of the SM, whose quantum instability gets actually worse because of the higher (cubic) dependence of the Higgs mass on the UV cut-off of the theory.

A recently-proposed [259, 260, 261], realistic, flat 5D model in the context of GHU will be discussed in detail in Section 4.3.

4.2 Extra-dimensions and Dark Matter

In the following, we summarize some of the various DM candidates proposed in ED scenarios (see e.g. [262] for a review).

- **KK graviton**: In some ED models, the Kaluza-Klein (KK) graviton is coupled to matter with a 4D ordinary gravity strength (i.e., with couplings $\sim G_N^{(4)}$). In this case, its lifetime is longer than the age of the Universe and it is non-thermally produced. In ADD models, the KK graviton has a meV mass and the picture typically requires fine-tuned conditions for the production mechanism. In the UED context, on the other hand, it can play the role of a superWIMP [72], as described in Section 1.3.2, with a mass around the Tev scale.

- **Radion**: The radion is the geometrical modulus of the ED, namely, a scalar degree of freedom associated to the size of the compactified dimensions. As in the case of KK graviton, it can be stable on a cosmological scale [263]. It is typically light (mass $\sim$ meV) and can play a crucial role in cosmology (e.g., modifying the inflationary scenario).

For this reason, it is quite strongly constrained and radion DM models often requires a significant amount of fine tuning.

- **Branons**: In brane-world scenarios, the branons are the Goldstone bosons corresponding to the spontaneous symmetry breaking of the translational invariance produced by the presence of the brane [264]. Translational invariance in the extra dimensions is not necessarily an exact symmetry and a branon mass is expected from such explicit symmetry breaking. Branons interact in pairs with SM particles, thus they are stable. At low energy, they are weakly interacting (depending on the tension scale) and for masses $\gtrsim$ 100 GeV, branons can act as WIMP candidates.

- $B^{(1)}$ **in UED models**: In the UED model, the lightest KK particle is stable, thanks to a discrete symmetry called KK-parity [107], All SM fields propagate in the flat extra dimension and the translation invariance along the extra dimension is only broken by the orbifold compactification (at loop level). The remnant unbroken $\mathbf{Z}_2$ subgroup of the translation group in the extra dimensions is the KK-parity. It inverts the segment of compactification around its middle point. In terms of a coordinate $0 \leq y \leq \pi R$, KK-parity implies the invariance of the Lagrangian under the transformation $y \rightarrow \pi R - y$. Thus, it requires that the boundary Lagrangians at the two orbifold fixed points are symmetric. This symmetry avoids interaction vertices with an odd number of odd-KK states and the LKP is stable.

  In some realizations, the LKP is the first KK excitation of the hypercharge gauge boson $B^{(1)}$. For an extra dimension of TeV^{-1} size, this LKP can act as a WIMP and its phenomenology has been investigated in depth recently (for a review, see [265]).

- **"warped" KK neutrino-like candidates**: A general analysis of a DM candidate in the form of a heavy Dirac neutrino with suppressed coupling to the SM Z boson is performed in [106]. They consider thermal relics in models extending the EW SM group to $SU(2)_L \times SU(2)_R \times U(1)$. Such neutrinos can be viable DM candidates with a mass between 10 GeV and 500 GeV, providing that the coupling to the Z is $\sim$100 times smaller than for SM neutrinos, in order to not violate direct detection bounds.

  In a 5D warped GUT model [109], a DM candidate of this sort arises as a KK state, with the stability guaranteed by a $\mathbf{Z}_3$ discrete symmetry related to the suppression of baryon number violation.

- **"warped" KK gauge bosons**: In Ref. [110], they consider a possible implementation of the KK parity in a warped geometry. This is done by introducing two distinct slices of AdS_5 and imposing a symmetry

interchanging them. The eigenstates can be divided into two classes with different symmetry properties; as in the flat UED case, KK-even modes have profiles symmetric under reflection around the mid-point of the extra dimension, while KK-odd modes have anti-symmetric profiles. Vertices with an odd number of odd-KK states are forbidden and the odd-LKP is stable. For a certain choice of the parameters in the model, it can be a KK Z gauge boson with TeV mass.

An extension to warped extra dimension of the discrete symmetry implemented in the next Section is analyzed in Ref. [111]. They show that such an "exchange" symmetry can generally give rise to realistic DM candidates. In the minimal composite Higgs model [257], for a certain choice of the boundary condition, the lightest $\mathbf{Z}_2$-odd gauge boson can be a viable DM candidates with mass in the 300-500 GeV range. Some of the $\mathbf{Z}_2$-odd colored fermions are nearly degenerate in mass with the DM candidate and co-annihilation effects lead to a DM relic abundance matching the cosmological amount of DM in the Universe today. Direct detection of this candidate is not very promising for the near future experiments, due to suppressed couplings to light quarks. On the other hand, they argue that particular details concerning the spectrum of the decay channels associated to the next-to-lightest odd particle can give a characteristic signature of the model at colliders.

A DM candidate, embedded in a 5D flat model realizing the GHU mechanism, has been recently proposed [108]. We extensively discuss this construction and its implications for DM searches [266] in the next Section. The exposition follows the line of papers [108] and [266].

4.3 A WIMP candidate from an extra non-universal dimension

In this Section, we show that viable DM candidates can be embedded in flat non-universal higher dimensional theories aiming at the stabilization of the EW scale. For such purpose, we will focus on a recently proposed 5D theory in which the Higgs field is the internal component of a gauge field, and Lorentz symmetry is broken in the bulk [261] (see e.g. [256] for a brief pedagogical review of such kind of models and for further references). Within this framework, a $\mathbf{Z}_2$ symmetry (called mirror symmetry) has been invoked to improve the naturalness of the model [261]; as a by-product, this symmetry guarantees the stability of the lightest $\mathbf{Z}_2$ odd particle. $\mathbf{Z}_2$ symmetries of this kind are less restrictive than KK–parity. Their implementation is particularly intuitive if one considers 5D theories on an interval $S^1/\mathbf{Z}_2$. The mirror symmetry acts on a given field and its copy under the symmetry, giving rise to periodic and anti-periodic states along the covering circle S^1,

respectively even and odd under the mirror symmetry. The LKP is then identified with the first KK mode of the lightest 5D antiperiodic field in the model, similarly to the LKP in UED models, but with the important difference that mirror symmetry is not a remnant of a space-time symmetry and hence does not necessarily act on all fields in the model. In particular, the mirror symmetry we propose here can be implemented in flat as well as warped spaces, and does not put any constraint on the relation between the boundary Lagrangians at the two fixed-points, aside the obvious one of being $\mathbf{Z}_2$ even.

We present here a detailed calculation of the thermal relic density of the LKP in the model of [261]. Since Lorentz symmetry in the extra dimension is explicitly broken, there is a certain degree of uncertainty in the model mass spectrum. We focus on the region in the parameter space where the LKP is the first KK mode of an antiperiodic gauge field, roughly aligned along the $U(1)_Y$ direction in field space. Electroweak bounds require this field to be heavier than about 2 TeV, in a range which is significantly more massive than the analogous state in the UED scenario [107], as well as most WIMP DM candidates. Since the mass is so heavy, the pair annihilation rate for our WIMP candidate is small and would tend to lead to the departure from thermal equilibrium at too early times, overproducing DM by one order of magnitude or more. On the other hand, the LKP appears within a set of other extra antiperiodic fields, most often with the next-to-lightest Kaluza–Klein particle (NLKP) being a strongly interacting particle. For reasonable values of parameters in the model, the mass splitting between NLKP and LKP turns out to be small, and the coannihilating NLKP becomes the particle triggering the freeze-out and possibly lowering the LKP relic density within the observed value. In particular, the nature of the EWSB in the model implies that typically the lightest $\mathbf{Z}_2$–odd fermion is the b_-, arising from the KK tower associated to the bottom quark. A strongly-interacting NLKP gauge boson can be found, instead, in case the mirror symmetry acts on the color $SU(3)_s$. For simplicity, we then discuss two classes of viable scenarios:

1. The LKP coannihilates with the b_-, and gluons are periodic on S^1.

2. Gluons are both periodic and antiperiodic on S^1 and the LKP coannihilates also with the first KK mode of the antiperiodic gluon.

Note that in the first scenario there is a further increase in the effective thermally averaged annihilation cross section due to a KK-gluon s-channel resonance in b_- pair annihilations. Values of the relic density in agreement with observations are obtained in both scenarios, with a moderate degree of fine-tuning (of order few percent), comparable or even lower than what one obtains in other cases in the literature when the relic density of the WIMP DM candidate is driven by coannihilation effects.

4.3.1 Mirror Symmetry

The most investigated cases for WIMP DM in ED frameworks arise in the UED model, where the LKP is stable thanks to the KK-parity. As we previously mentioned, such symmetry implies, in particular, the equality of any possible localized Lagrangian terms at $y = 0$ and at $y = \pi R$: $\mathcal{L}_0 = \mathcal{L}_\pi$. Most extra dimensional models which aim to stabilize in one way or another the EW scale, however, requires $\mathcal{L}_0 \neq \mathcal{L}_\pi$ and do not respect KK–parity. In particular, models based on 5D warped spaces [253] manifestly violate this symmetry. It is then desirable to impose some other less constraining symmetry protecting some KK modes from decaying.

The $\mathbf{Z}_2$ symmetry we will consider below has been introduced in [261] and allows for arbitrary localized terms in the Lagrangian. As it will be clear below, it works for both flat and warped spaces. Consider a simple toy model of two interacting 5D real scalar fields ϕ_1 and ϕ_2 and impose on the system a $\mathbf{Z}_2$ symmetry which interchange them: $\phi_{1,2} \leftrightarrow \phi_{2,1}$. Being the Lagrangian invariant under this symmetry, we can impose boundary conditions of the following form for ϕ_1 and ϕ_2 (in the $S^1/\mathbf{Z}_2$ orbifold notation):

$$\phi_1(y + 2\pi R) = \phi_2(y)\,, \qquad \phi_1(-y) = \eta\phi_2(y)\,, \tag{4.3}$$

where $\eta = \pm$. It is convenient to define linear combinations $\phi_\pm = (\phi_1 \pm \phi_2)/\sqrt{2}$ which are respectively periodic and antiperiodic on the covering circle S^1 and with definite orbifold parities: $\phi_\pm(-y) = \pm\eta\phi_\pm(y)$. Equivalently, one can consider in Eq. (4.3) the standard parity projection $\phi_1(-y) = \eta\phi_1(y)$ instead of $\phi_1(-y) = \eta\phi_2(y)$, resulting in a change of parity for ϕ_-. Under the $\mathbf{Z}_2$ symmetry, $\phi_\pm \to \pm\phi_\pm$, so we can assign a multiplicative charge $+1$ to ϕ_+ and -1 to ϕ_-. The localized Lagrangian terms $\mathcal{L}_0$ and $\mathcal{L}_\pi$, which can include boundary fields as well, can be arbitrary and in general different from each other, provided they respect the above $\mathbf{Z}_2$ symmetry. We denote such $\mathbf{Z}_2$ symmetry as "mirror symmetry" in the following. It can also be implemented on gauge fields. For Abelian gauge groups, it works as before and one is left with two gauge fields, one periodic and one anti–periodic. For non-abelian gauge groups, mirror symmetry can be easily implemented only when the orbifold twist (or the boundary conditions on the segment) are trivially embedded in the gauge group. In such a case, starting from two identical gauge groups $G_1 \times G_2$, the boundary conditions (4.3) leave unbroken in 4D only the diagonal subgroup G_+.[1] Mirror symmetry changes the sign of all half–integer KK modes, associated to the antiperiodic field ϕ_-, leaving invariant the integer KK modes of ϕ_+. As such, the first half-integer $n = 1/2$ KK mode of ϕ_- cannot decay and is stable. Mirror symmetry acts on these fields as KK–parity, provided one rescales $R \to R/2$, but with the

[1] Notice that the antiperiodic gauge fields A_- are *not* connections of the gauge group G_-. The latter is not a group, but the symmetric quotient $(G_1 \times G_2)/G_+$.

important difference, as already pointed out, of allowing more freedom in the 5D theory and on the localized 4D Lagrangian terms.

It is straightforward to generalize the action of mirror symmetry for more extra dimensions. For instance, for complex scalars ϕ_1 and ϕ_2 compactified on a T^2/Z_2 orbifold one can have

$$\phi_1(z+1) = \phi_2(z)\,, \qquad \phi_1(z+\tau) = \phi_2(z)\,, \qquad \phi_1(-z) = \eta\phi_2(z)\,, \quad (4.4)$$

with z properly normalized dimensionless coordinates on T^2 and τ its modular parameter. As in the 5D case, the lowest KK mode of ϕ_- is absolutely stable.

The mirror symmetry can be also easily extended to warped models. The implementation proceeds in a similar way as described above. The role of the periodic states in flat ED is played in warped space by fields obeying (+,+) or (-,-) boundary conditions and antiperiodic states are replaced by fields obeying (+,-) or (-,+) boundary conditions. The sign +(-) denotes Neumann (Dirichlet) boundary conditions and the first/second entry in the parenthesis refers to the UV/IR brane, respectively. A model-independent implementation of this symmetry in warped scenarios is performed in [111] (where it is called "exchange symmetry"). They show how this mechanism can generally lead to a stable DM candidate.

From a model-building point of view, it is of course desirable not to impose mirror symmetry *ad hoc* for the only purpose of getting a stable particle, possibly with the correct properties of being a good DM candidate. This is not mandatory but makes the symmetry "more natural". In Supersymmetry, for instance, R–symmetry is typically imposed not only to have a stable supersymmetric particle but also to avoid baryon–violating operators that would lead to a too fast proton decay. In the following, in the same spirit, we will consider a model [261] where mirror symmetry has been introduced to reduce the fine-tuning needed to stabilize the electroweak scale.

4.3.2 The Model

The model we consider is a model of gauge-Higgs unification on a flat 5D space of the form $R^{1,3} \times S^1/\mathbf{Z}_2$. It is well known that in models of this sort is hard to get sufficiently heavy masses for the Higgs field and the top quark, due to various symmetry constraints, including 5D Lorentz symmetry. The latter symmetry, in particular, links gauge and Yukawa couplings between each other and does not easily allow to get the correct top Yukawa coupling. Due to the radiative origin of the Higgs potential, a large Yukawa coupling will also tend to increase the Higgs mass. It has been shown in [260, 261] that by explicitly breaking 5D Lorentz symmetry in the bulk (leaving the 4D Lorentz symmetry unbroken), one can easily overcome the two above problems of too light Higgs and top fields, having now no constraint linking gauge and Yukawa couplings. In the following, we review very briefly the

main features of the model — referring the interested reader to [259, 260, 261] for further details — and then consider in some detail the mass spectrum of the lightest non-SM states.

The gauge group is taken to be of the form $G \times G_1 \times G_2$, with a certain number of couples of bulk fermions $(\Psi_1, \widetilde{\Psi}_1)$ and $(\Psi_2, \widetilde{\Psi}_2)$, with identical quantum numbers under the group G and opposite orbifold parities. We require that the Lagrangian is invariant under the mirror symmetry $1 \leftrightarrow 2$. The couples $(\Psi_1, \widetilde{\Psi}_1)$ are charged under G_1 and neutral under G_2 and, by mirror symmetry, the same number of couples $(\Psi_2, \widetilde{\Psi}_2)$ are charged under G_2 and neutral under G_1. No bulk field is simultaneously charged under both G_1 and G_2.

We can make two different choices for G and $G_{1,2}$, depending on whether we double the color group or not. We can either take $G = SU(3)_w \times SU(3)_s$ and $G_i = U(1)_i$ or $G = SU(3)_w$ and $G_i = SU(3)_{i,s} \times U(1)_i$ $(i = 1, 2)$.[2] As we will see, both choices can give rise to a DM candidate with the correct relic density. For definiteness, we focus in the following on the case in which $G_i = SU(3)_{i,s} \times U(1)_i$; the other case can be trivially derived in analogy. In total, we introduce (for each SM generation) one pair of couples $(\Psi^u_{1,2}, \widetilde{\Psi}^u_{1,2})$ in the anti-fundamental representation of $SU(3)_w$ and one pair of couples $(\Psi^d_{1,2}, \widetilde{\Psi}^d_{1,2})$ in the symmetric representation of $SU(3)_w$. Both pairs have $U(1)_{1,2}$ charge $+1/3$ and are in the fundamental representation of $SU(3)_{1,2,s}$. The boundary conditions of these fermions and gauge fields follow from Eqs. (4.3) and the twist matrix introduced in [259]. The unbroken gauge group at $y = 0$ is $SU(2) \times U(1) \times G_+$, whereas at $y = \pi R$ we have $SU(2) \times U(1) \times G_1 \times G_2$. We also introduce massless chiral fermions with the SM quantum numbers and $\mathbf{Z}_2$ charge $+1$, localized at $y = 0$. Mirror symmetry and the boundary conditions (4.3) imply that the localized fields can (minimally) couple only to A_+ and mix with the bulk fermions Ψ_+.

Before EWSB, the massless bosonic 4D fields are the gauge bosons in the adjoint of $SU(2) \times U(1) \subset SU(3)_w$, $U(1)_+$, gluon gauge fields g_+ and a charged scalar doublet Higgs field, arising from the internal components of the odd $SU(3)_w$ $5D$ gauge fields. The $SU(3)_{+,s}$ and $SU(2)$ gauge groups are identified respectively with the SM $SU(3)_s$ and $SU(2)_L$ ones, while the hypercharge $U(1)_Y$ is the diagonal subgroup of $U(1)$ and $U(1)_+$. The extra $U(1)_X$ gauge symmetry surviving the orbifold projection is anomalous and its corresponding zero mode gauge boson gets a mass of the order of the cut-off scale Λ of the model ($\Lambda \simeq (3 \div 4)/R$ [261]). The massless fermionic 4D fields, identified with the SM fermions, are the zero modes of a coupled bulk–to–boundary fermion system. Differently from the bosonic massless fields above, which all have a constant profile along the fifth dimension, fermions have a profile which depends on the bulk–to–boundary mixing terms. To a reasonable approximation, one can consider all SM fermions localized at

[2] The doubling of the $U(1)$ factor is necessary and motivated by naturalness [261].

$y = 0$, with the exception of the bottom quark, which shows a small wave-function tail away from $y = 0$ and the top quark, which is nearly totally delocalized. All SM fields are even under mirror symmetry with the lightest $\mathbf{Z}_2$ odd state in the model absolutely stable. Since the bulk fermions $\Psi_\pm$ have 5D Dirac mass terms, in a (large) fraction of the parameter space of the model, as we will see below, the lightest $\mathbf{Z}_2$ odd state is the first KK mode of the antiperiodic $U(1)_-$ gauge field, denoted by A_-.

4.3.3 Mass Spectrum

Electroweak constraints fix the compactification scale in the multi-TeV regime. More precisely, it has been found in [261] that $1/R \geq 4.7$ TeV at 90% C.L. to pass all flavour and CP conserving bounds. The lightest non-SM particles turn out to be in the 1 TeV range and thus for all practical purposes we can neglect EWSB effects and consider the mass spectrum in the unbroken phase.

Let us first consider $\mathbf{Z}_2$ even gauge bosons. Aside from the massless SM fields considered before, we have a standard tower of KK states for all gauge fields, with the exception of X, the gauge field of the anomalous $U(1)_X$ symmetry, which becomes effectively a field with Dirichlet/Neumann boundary conditions at $y = 0/\pi R$ and of Y, the gauge field of the hypercharge $U(1)_Y$, which can mix with X. We have then ($n \geq 1$),

$$m_{W_+}^{(2n)} = \frac{n}{R}\,, \tag{4.5}$$

$$m_{g_+}^{(2n)} = \rho_s \frac{n}{R}\,, \tag{4.6}$$

where $m_{W_+}^{(2n)}$ and $m_{g_+}^{(2n)}$ denote the masses of all $SU(3)_w \times U(1)'$ and $SU(3)_{+,s}$ gluon KK gauge fields except X and Y. Since Lorentz invariance is broken in the bulk, we have in general introduced the Lorentz–violating parameters ρ and ρ_s, which are the coefficients for the gauge kinetic terms of the form $F_{\mu 5}^2$ for $U(1)'$ and $SU(3)_s$ respectively (see [261] for further details). In the following, we will mostly consider the case in which $\rho \sim \rho_s \simeq 1$, the Lorentz–invariant value. When $\rho \simeq 1$, the mixing between Y and X is negligible and their KK masses are given by

$$m_{Y_+}^{(2n)} \simeq \rho \frac{n}{R}\,, \tag{4.7}$$

$$m_{X_+}^{(2n)} \simeq \rho \frac{(n-1/2)}{R}\,. \tag{4.8}$$

The mass spectra of $\mathbf{Z}_2$ odd gauge bosons is easily derived, since no anomalies arise here. We have

$$m_{g_-}^{(2n-1)} = \rho_s \frac{(n-1/2)}{R}\,, \tag{4.9}$$

$$m_{A_-}^{(2n-1)} = \rho \frac{(n-1/2)}{R}\,. \tag{4.10}$$

The mass spectra for periodic $SU(2)_L$–triplet fermions and for all antiperiodic fermions is also easily computed, since they cannot mix with boundary fermions. One has

$$\begin{cases} m_{i+}^{(2n)} = \sqrt{M_i^2 + k_i^2 \left(\frac{n}{R}\right)^2} & n \geq 0 \\ m_{i-}^{(2n-1)} = \sqrt{M_i^2 + k_i^2 \left(\frac{(n-1/2)}{R}\right)^2} & n \geq 1 \ , \end{cases} \tag{4.11}$$

where k_i are the Lorentz-violating factors entering in the covariant derivative of the fermions and M_i are bulk mass terms (notation as in [261]).

The mass spectra for $SU(2)_L$ doublet and singlet periodic fermions is more complicated and given by the roots of transcendental equations which do not admit simple analytic expressions. These equations depend on the bulk–to–boundary mixing terms $\epsilon_{1,2}^i$, the parameters k_i and the bulk mass terms M_i. After EWSB, the SM fermion masses are function of these parameters, so that the subspace of the parameter space spanned by (ϵ_i, k_i, M_i) is not totally arbitrary. In addition, the electroweak constraints, perturbativity and an estimate of the size of possible Flavor Changing Neutral Currents (FCNC) favor a given regime for such parameters. For all quarks and leptons, except the top and bottom quarks, $\epsilon_{1,2}^i \simeq 0.1$, $k_i \simeq 1$. For the bottom quark we have $\epsilon_{1,2}^b \simeq 0.2$, $k_b \simeq 1$ and for the top quark $\epsilon_{1,2}^t \simeq 1.2$, $k_t \simeq 2.5$[3]. Having fixed $\epsilon_{1,2}^i$ and k_i, the bulk mass terms M_i are derived by the known values of the SM fermion masses.

We summarize in Fig. 4.1 the masses of the lightest KK states for the typical values of the parameters considered above. We report the tree–level mass spectra for both $\mathbf{Z}_2$ odd and even states for completeness, although the latter do not play an important role in the thermal relic density computation. We denote by $b_-^{(1)}, c_-^{(1)}$, etc. the first $n = 1$ KK mode of the corresponding antiperiodic fermions Ψ_-^b, Ψ_-^c and so on. Similarly, for the $n = 0$ KK modes $b_+^{(0)}$, $c_+^{(0)}$, etc. of the $SU(2)_L$ triplet fermions. The fields in the fourth and fifth column in Fig.4.1 (perturbed doublet and perturbed singlet) are the first periodic massive resonances of the corresponding SM fields. For $\rho_s \gtrsim \rho$, the lightest $\mathbf{Z}_2$ particle is the first $n = 1$ mode of A_-, denoted by $A_-^{(1)}$, which will be our DM candidate.[4] As can be seen from Fig. 4.1, it does not coincide with the lightest non-SM particle in the model, the latter being given by two $\mathbf{Z}_2$–even fermions, $SU(2)_L$ triplets, which are almost degenerate with an other $\mathbf{Z}_2$ even fermion, $SU(2)_L$ singlet. They all come from the KK tower associated to the bottom quark and have a mass $\sim 1/(5R)$.

[3] This is the only needed and relevant Lorentz violating coupling in the model.

[4] As mentioned in Section 4.2, the DM candidate might also be identified with the radion. In our scenario, most likely, the radion physics will be entangled with the microscopic mechanism inducing the 5D Lorentz breaking, which might also provide a stabilization mechanism for the radion. The radion physics should then be revised with respect to the case of [263]. This analysis is beyond the aims of our treatment and may deserve further study.

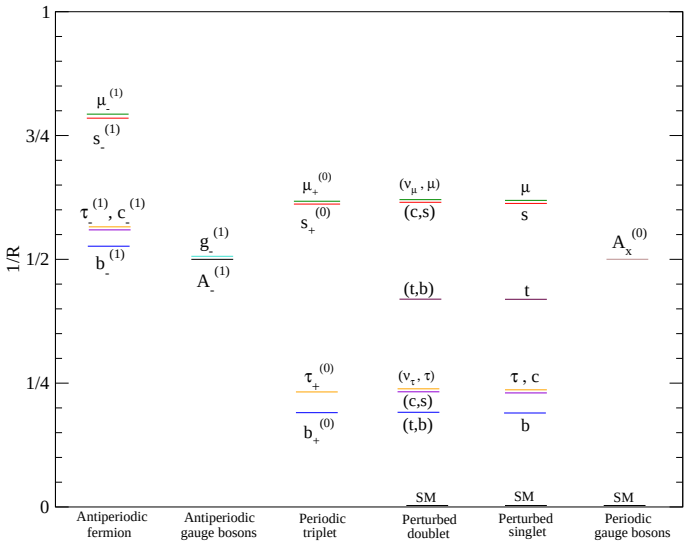

Figure 4.1: Tree–level spectrum for all states with mass $< 1/R$. The DM candidate is $A_-^{(1)}$.

Having various free parameters governing the masses of the relevant KK modes, it is pointless to compute the mass corrections induced by the EWSB and radiative corrections. They can all be encoded in the effective parameters ρ, ρ_s and k_i.[5] There is however a case in which radiative corrections are relevant and need to be computed. When the $n = 1$ KK gluons $g_-^{(1)}$ (or KK fermions $b_-^{(1)}$) coannihilate with $A_-^{(1)}$, the s–channel diagram in which a $g_+^{(2)}$ is created in the $g_-^{(1)}$–$g_-^{(1)}$ (or $b_-^{(1)}$–$b_-^{(1)}$) annihilation might be in resonance and amplify the annihilation in question, decreasing the relic density. Although the absolute radiative correction to the mass of $g_-^{(1)}$ or $g_+^{(2)}$ is irrelevant, being reabsorbed in ρ_s, the *relative* correction matters and it is this the relevant quantity to study — together with the decay width of $g_+^{(2)}$ — for quantifying the effect of the resonance. They are also the relevant quantities for the $b_-^{(1)}$ annihilation, once the relation between ρ_s and k_b is fixed. We have then computed the mass splitting $\Delta m_g \equiv 2m_{g_-}^{(1)} - m_{g_+}^{(2)}$ at one–loop level. Details on such a computation can be found in the Appendix B. For the parameter range taken above, the result of the splitting is the following:

$$\Delta m_g = m_{g_+}^{(2)} - 2m_{g_-}^{(1)} \simeq -1.4\,\alpha_s\, m_{g_+}^{(2)} \ , \tag{4.12}$$

where α_s is the strong coupling constant, evaluated at the energy scale ρ_s/R.

[5] As we will see in the following, the region in parameter space where $\rho_s \simeq \rho$ is the most interesting as far as DM is concerned. Strictly speaking, then, we are considering tree-level values of ρ_s and ρ which differ by the correct amount to compensate the splitting induced by quantum corrections.

The value (4.12) is comparable with the total decay rate Γ_g of $g_+^{(2)}$, which at tree–level is purely given by the processes $g_+^{(2)} \to \bar{q}_{L,R}\, q_{L,R}$. For each quark, we get $\Gamma_{g,L/R} = \frac{1}{12}\,(c_{L/R,g}^{(2,0,0}})^2 \alpha_s m_{g_+}^{(2)}$, where the couplings $c_{L/R,g}^{(2,0,0)}$ are given by Eqs.(A.7) and (A.8). Summing over all SM quarks:

$$\Gamma_g = \tilde{c}^2 \alpha_s m_{g_+}^{(2)} \simeq 1.5\, \alpha_s\, m_{g_+}^{(2)}\,, \tag{4.13}$$

where $\tilde{c}^2$ is the mean value of the couplings $c_{L/R,g}^{(2,0,0)}$ squared. As can be seen, $\Gamma_g \simeq |\Delta m_g|$.

4.3.4 Relic Density

The setup we have introduced is typical for frameworks embedding a cold dark matter candidate. There is a tower of massive states which are in thermal equilibrium in the early Universe, and a symmetry, the $\mathbf{Z}_2$-parity, preventing the lightest of these states to decay. We have also shown that it is natural for such stable species to be the $A_-^{(1)}$, i.e. a particle which is electric- and color-charge neutral and hence, potentially, a good dark matter candidate. As a rule of thumb, the thermal relic density of a massive particle (i.e. a particle non-relativistic at freeze-out) scales with the inverse of its pair annihilation rate into lighter SM species. In case of the $A_-^{(1)}$, we need to take into account that its mass splitting with other antiperiodic states can be small: there is a full set of coannihilating particles, whose density evolution needs to be described simultaneously through a set of coupled Boltzmann equations as discussed in Section 2.3.1. The picture is analogous to what one finds for UED models [267, 268], or sometimes encounters in the supersymmetric frameworks, see e.g. [94, 269, 270]: In our case, the annihilation rate per degree of freedom of the coannihilating states is larger than for $A_-^{(1)}$; therefore, coannihilation processes delay the decoupling of the latter and diminish its thermal relic component.

Relic abundances are computed solving numerically the density evolution equation (2.8) with the technique described in Section 2.3.1.

Minimal DM framework

We consider first the framework in which the mirror symmetry does not act on the colored $SU(3)_s$ group, and all gluons are periodic states on S^1. In this case, for the typical set of fermionic parameters introduced in Section 4.3.2, the DM candidate $A_-^{(1)}$ shares large coannihilation effects with the lightest antiperiodic fermion $b_-^{(1)}$ (see Fig.1); the latter are actually two degenerate fermions in the **6** of $SU(3)_w$ (see Table C.2 for an account of the degrees of freedom of $b_-^{(1)}$ and other relevant particles). The antiperiodic fermions $c_-^{(1)}$ and $\tau_-^{(1)}$ will also be included in the numerical computation of the relic

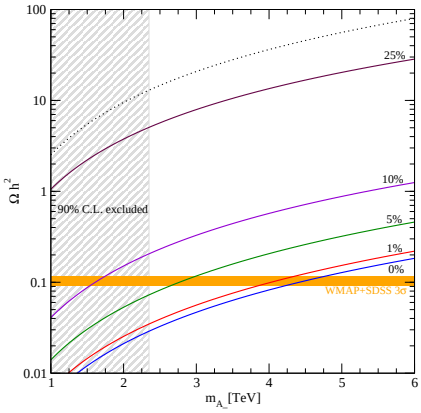

Figure 4.2: Relic density versus the $A_-^{(1)}$ mass, for a few value of the relative mass splitting between $A_-^{(1)}$ and $b_-^{(1)}$, and in the case of the $g_+^{(2)}$ on resonance in $b_-^{(1)}$ pair annihilations.

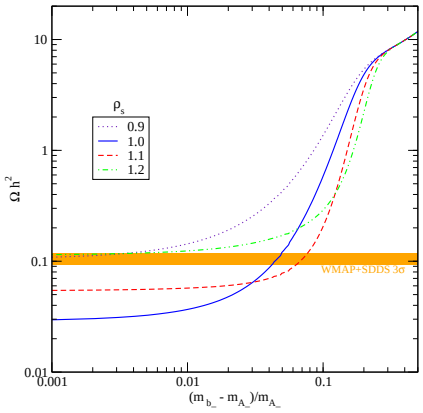

Figure 4.3: Relic density versus the mass splitting between $A_-^{(1)}$ and $b_-^{(1)}$ for a few values of Lorentz breaking parameter ρ_s and assuming as compatification scale $1/R = 4.7$ TeV.

density, although their contribution is very small. As in all coannihilation schemes, our results will be most sensitive to the relative mass splitting between the DM candidate and the heavier state. In what follows we treat the mass of $A_-^{(1)}$ as a free parameter, or, having fixed the Lorentz violating parameter $\rho = 1$, use it interchangeably with the compactification scale $1/R$, (recall that $m_{A_-^{(1)}} = \rho/(2\,R)$). We also take the mass of $b_-^{(1)}$ as a free parameter; this is equivalent to introducing a slight departure of the Lorentz breaking parameter k_b from its unbroken value $k_b = 1$, having assigned $\epsilon_{1,2}^b = 0.2$, $k_t = 2.5$ and $\epsilon_{1,2}^t = 1.2$; for all other antiperiodic fermions we assume $k_i = k_b$ and $\epsilon_{1,2}^i = 0.1$.

Since electroweak precision tests set a lower bound on the compactification scale at about $1/R > 4.7$ TeV (90% C.L., see [261]), the attempt here is to introduce a dark matter candidate with a mass of 2.3 TeV or larger. Moreover, $A_-^{(1)}$ does not minimally couple to the localized fermions, which are the main components of SM fields. The only diagrams giving a significant contribution to the $A_-^{(1)}$ pair annihilation rate are those with a third generation quark in the final state and a third generation antiperiodic fermion in a t- or u-channel; this follows from the fact that only for the third generation the antiperiodic fermion and gauge boson wavefunctions can have a order one overlap with SM fields. We list the set of Feynman rules relevant for this process and the others introduced below in Appendix A, while the full list of the diagrams which are needed in the relic density calculation is given in Appendix C. In the region of interest for our model, we find that, whenever $b_-^{(1)}$ coannihilations are not effective, the thermal relic abundance of $A_-^{(1)}$

greatly exceeds the cosmological limit, see the dotted curve in Fig. 4.2.

On the other hand, pair annihilation rates for the $b_-^{(1)}$ are much larger and do enter critically in the effective thermally averaged cross section: there is a full set of strongly interacting final states mediated, in the s-channel, by either the SM gluon or by the first periodic KK-gluon $g_+^{(2)}$. In general, it is not relevant to include in our computation states with KK number greater than 1; in this case, however, since $m_{g_+}^{(2)}$ is about twice $m_{b_-}^{(1)}$ (recall that $m_{g_+}^{(2)}$ is of order $1/R$, while $m_{b_-}^{(1)}$ of order $1/(2\,R)$), the annihilation diagrams with $g_+^{(2)}$ in the s-channel become resonant and tend to give the dominant contribution to the cross section (the effect of resonances induced by second KK particles was first pointed out in [271] within the UED context). The enhancement is maximized for splittings $\left|2m_{b_-}^{(1)} - m_{g_+}^{(2)}\right|$ which are below the $g_+^{(2)}$ decay width, see Eq. (4.13), which is indeed much smaller than the energy flowing in the s-channel. We find that, on top of the two mass parameters $m_{A_-}^{(1)}$ and $m_{b_-}^{(1)}$, the mass of $g_+^{(2)}$ is the third unknown entering critically in our analysis; we take it as a free parameter, again in connection to a possible mild variation of ρ_s around its non-violating Lorentz value $\rho_s = 1$.

Finally, there is another relevant issue concerning strongly interacting states we wish to mention before going to the illustration of results: we are considering processes taking place at a center of mass energy $\simeq 1/R$ which is about twice the mass of the annihilating DM particle. The QCD coupling constant α_s should be evaluated at this relatively high scale and hence renormalization group effects cannot be neglected, in principle. Indeed, the DM abundance is highly sensitive to α_s which enters quadratically in annihilation rates: roughly $\Omega_{DM} \propto \alpha_s^{-2}$. We have computed the one–loop β-function for α_s within our framework (see Appendix D of [108] for details) and implemented the running numerically in our Boltzmann code; at 5 TeV, α_s turns out to be approximately 0.097.[6]

As mentioned in Section 2.3.1, non-perturbative corrections can affect the relic density computation.

The formation of bound states could in principle alter the importance of coannihilation effects. Indeed, if meta-stable bound states $b_-^{(1)} - \bar{b}_-^{(1)}$ can form before the decay of the $b_-^{(1)}$ into $A_-^{(1)}$, the DM abundance would be modified. The binding energy of such bound states can be estimated in analogy to positronium [111], leading to $E_b \lesssim 6 \cdot 10^{-3} m_{A_-}^{(1)}$. The freeze-out temperature is $T_f \sim m_{A_-}^{(1)}/25$ and, thus, they would form well after the freeze-out. On

[6] The running of α_s was apparently overlooked in Refs. [267, 268] when estimating the effect of coannihilations of the LKP with strongly interacting KK states within the UED framework. As explained in Appendix D of [108], the effect in UED is larger than for our model; since annihilation cross sections scale approximately as $\alpha_s^2 \times (1/R)^{-2}$, we expect that the values of $1/R$ inferred from the cosmological limit should be correspondingly rescaled down.

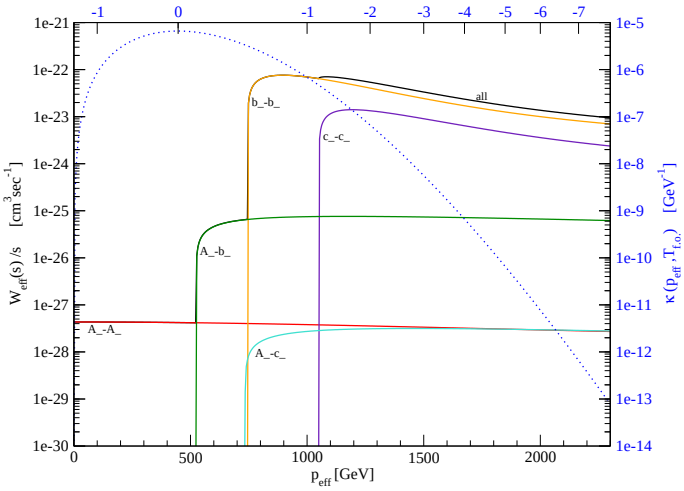

Figure 4.4: Effective annihilation rate $W_{\rm eff}$ over the center of mass energy squared s, plotted versus the effective center of mass momentum $p_{\rm eff}$. Contributions from single annihilation and coannihilation channels are displayed. Also shown (dotted line) is the thermal weight function κ (units of GeV^{-1} as displayed with the scale on the right-hand side of the plot).

the other hand, the time-scale associated to the decay is much shorter than these time-scales and the $b_-^{(1)}$ decays into $A_-^{(1)}$ immediately after the freeze-out. This correction can be safely neglected.

In the case of strongly-interacting particles, the Sommerfeld effect is typically sizable. Being $b_-^{(1)}$ in the fundamental representation of $SU(3)_s$, it can annihilate through singlet or octet $SU(3)_s$ configurations. The long-range Coulomb-like forces distort in a different way the two related wave functions. The computation can be performed analogously to the case of Ref. [111]. The sizable enhancement of the $b_-^{(1)}$ annihilation cross section in the (attractive) singlet channel is compensated by the opposite effect in the (repulsive) octet channel. The non-perturbative corrections to the DM relic density turns out to be highly subdominant.

In Fig. 4.2 we show the results for the relic density as a function of $m_{A_-}^{(1)}$, for a few values of the relative mass splitting $(m_{b_-}^{(1)} - m_{A_-}^{(1)})/m_{A_-}^{(1)}$, and taking $g_+^{(2)}$ on resonance, i.e. $m_{g_+}^{(2)} \equiv 2m_{b_-}^{(1)}$. From the case with zero mass splitting one can read out the cosmological upper limit on $m_{A_-}^{(1)}$ within this framework, namely $m_{A_-}^{(1)} \leq 4.5$ TeV, or equivalently the bound on the compactification scale $1/R \leq 9$ TeV: this scale is comparable to those favored by electroweak precision tests [261]. As expected, the prediction of the relic density scales rather rapidly to larger values when the mass splitting among the coannihilating states is increased, and, consequently, the value for the

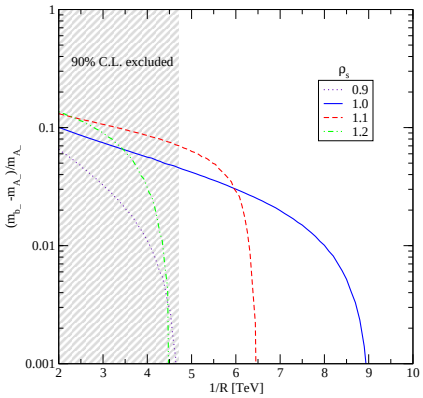

Figure 4.5: Correlation between the $A_-^{(1)} - b_-^{(1)}$ mass splitting and compactification radius in models with Ωh^2 matching the best fit value from cosmological observations, for a few values of ρ_s.

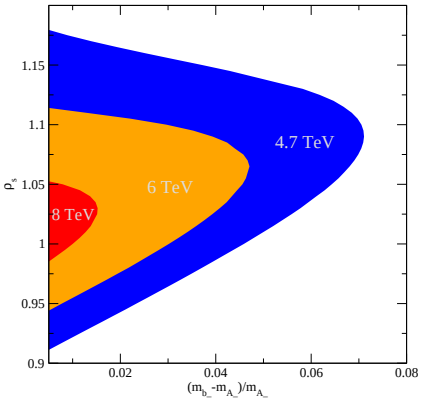

Figure 4.6: For a few selected values of the compactification scale, regions in the parameter space ρ_s– mass splitting in which Ωh^2 is lower or equal to the best fit value from cosmological observations.

mass of the DM candidate approaches the region excluded by electroweak physics (in the figure, the light-shaded horizontal band correspond to the 3 σ preferred region from the combined analysis of data on the CMB from WMAP 3-years data and from the SDSS large scale structure survey [272]; models which lay below the band correspond to configurations in which $A_-^{(1)}$ accounts for only a portion of the DM in the Universe, while those above it are cosmologically excluded). In Fig. 4.3 we plot the thermal relic abundance as a function of the mass splitting of the coannihilating states for a model with the minimum allowed compatification radius $1/R = 4.7$ TeV, and for a few values of ρ_s. In this case, as it can be seen, cosmological constraints restrict the Lorentz breaking parameter of $SU(3)_s$ roughly in the range [0.9, 1.2]; the interval is not symmetric around $\rho_s = 1$ since, in the Boltzmann equation, annihilations take place at a finite temperature. For $\rho_s < 1$, temperature corrections drive the process at energies always slightly above the resonance. In the opposite regime the resonance is always met, provided one considers sufficiently high temperatures; if ρ_s is large, the temperature at which the resonance is hit is too large compared to the freeze-out temperature and the models becomes cosmologically excluded. Curves for the four sample values of ρ_s overlap at a mass splitting of about 30%, beyond which coannihilation effects induce negligible changes on the $A_-^{(1)}$ relic abundance.

Conservatively, we include in the relic density calculation all states with a mass splitting below 50%. In Fig. 4.4 we illustrate better the role of coannihilations and of the Boltzmann suppression when mass splittings become too large. We consider the model with $1/R = 4.7$ TeV, $\rho_s = 1$ and $k_i = 1$, with

relic density of about 0.1, and plot the effective annihilation rate $W_{\rm eff}$, as defined in Eq. (2.14), over the center of mass energy squared s, as a function of the effective center of mass momentum $p_{\rm eff}$. Contributions to $W_{\rm eff}$ from the individual annihilation and coannihilation processes are shown; coannihilations appear here as thresholds at $\sqrt{s}$ equal to the sum of the masses of the coannihilating particles, with the NLKP entering first, and $c_-^{(1)}$ at a slightly larger $p_{\rm eff}$. The threshold effects are so sharp since coannihilation rates are large, but also because the number of internal degrees of freedom for the antiperiodic fermions is much larger than that for $A_-^{(1)}$ (see Table C.2). Also shown in Fig. 4.4 is the weight function $\kappa(p_{\rm eff}, T)$ defined implicitly by rewriting the thermally averaged cross section in Eq. (2.13) as

$$\langle \sigma_{\rm eff} v \rangle \equiv \int_0^\infty dp_{\rm eff} \frac{W_{\rm eff}\,(s)}{s}\, \kappa(p_{\rm eff}, T)\ . \tag{4.14}$$

The function κ contains the Boltzmann factors (hence it is exponentially suppressed at large $p_{\rm eff}$) and a phase-space integrand term (hence it goes to zero in the $p_{\rm eff} \to 0$ limit). It can be view as a weight function, since at any given temperature T, it selects the range of $p_{\rm eff}$ which are relevant for the thermal average. In Fig. 4.4, κ is plotted as a function of $p_{\rm eff}$ at the freeze-out temperature (defined as the temperature at which Y is equal to twice the final asymptotic value) in units of GeV^{-1} and with respect to the scale shown on the right-hand side of the plot. On the top of the panel, the tick mark with the label '0' corresponds to the momentum at which κ has its maximum, while the tick mark with label $-n$ indicates the momentum at which κ is 10^{-n} of its peak value. Coannihilation effects are relevant if they provide a significant enhancement in the effective annihilation rate within the range of momenta in which κ is not too small compared to its peak value; this is clearly the case for the $b_-^{(1)}$ in the example displayed. Also notice that the effect induced by the $c_-^{(1)}$ is not negligible by itself, however it gets marginal when superimposed to the one from the $b_-^{(1)}$.

Figs. 4.5 and 4.6 summarize the picture within our minimal DM framework. We select models whose thermal relic density matches the best fit value from cosmological observations $\Omega_{DM} h^2 = 0.105$. As already explained, there are three relevant mass parameters in the model: $m_{A_-}^{(1)}$ or equivalently $1/R$, $m_{b_-}^{(1)}$ or equivalently the relative mass splitting between $b_-^{(1)}$ and $A_-^{(1)}$, and $m_{g_+}^{(2)}$ or equivalently ρ_s. In Fig. 4.5 we select a few values of ρ_s and find the isolevel curves for Ωh^2 in the plane of the other two; in Fig. 4.6, instead, a few values of the compatification scale are considered and correlations between the other two parameters derived. The general trends we see here are essentially along the lines we have already discussed for Figs. 4.2 and 4.3; we display more clearly the strict upper limits on $1/R$ (about 9 TeV), and find that the NLKP–LKP mass-splitting needs to be at about the 7% level

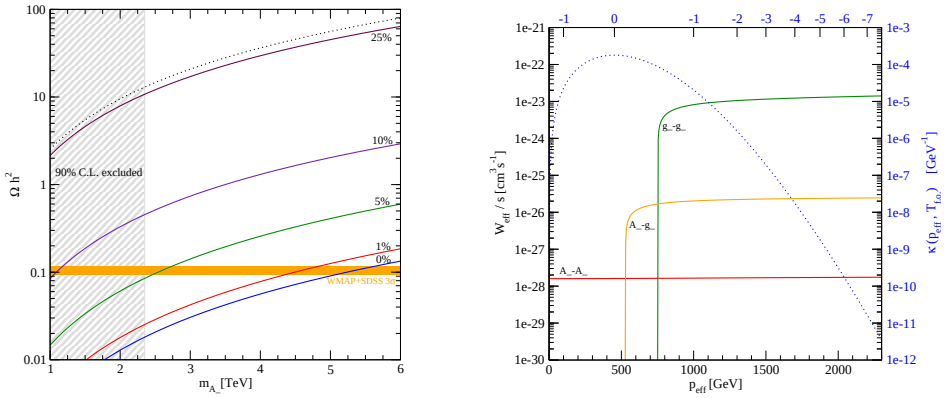

Figure 4.7: *Left Panel:* Relic density versus the $A_-^{(1)}$ mass, for a few value of the relative mass splitting between $g_-^{(1)}$ and $A_-^{(1)}$. Antiperiodic fermions have been decoupled assuming they have a mass splitting larger than 50%. *Right Panel:* Effective annihilation rate $W_{\rm eff}$ over the center of mass energy squared s, as in Fig. 4.4, but for a model with $g_-^{(1)}$ coannihilations decreasing the relic density of $A_-^{(1)}$ to the level of the best fit from cosmological observations. The thermal weight function κ is shown as a dotted curve; see Fig. 4.4, and the relative discussion in the text, for further details.

or smaller. The required range of ρ_s, for a given compactification scale and mass splitting, is also displayed.

We have definitely found a tight interplay among the parameters in the model; the procedure of embedding a DM candidate in this minimal scenario has been successful, pointing to a limited set of patterns in the parameter space.

DM in the framework with a copy of $SU(3)_s$

If the $\mathbf{Z}_2$ mirror symmetry acts on the colored $SU(3)_s$ group, the first antiperiodic KK gluon $g_-^{(1)}$, which has a mass of order $1/(2\,R)$, enters critically in the computation of the relic abundance for the $A_-^{(1)}$. In most extensions to the SM, strongly interacting gauge bosons are the particles with largest pair annihilation cross section per internal degree of freedom, hence tend to give the largest possible coannihilation effects. This has been verified also in the extra-dimension context studying the coannihilation of the LKP with the first KK excitation of the gluon in UED [267, 268].

We discuss the phenomenology in our model referring again to the three mass parameters introduced above. Note, however, that in this case we select values of ρ_s to fix both the mass of $g_-^{(1)}$ (we implement the tree-level relation $m_{g_-}^{(1)} = \rho_s/(2\,R)$) and the mass of $g_+^{(2)}$ (through the 1-loop mass splitting as found in Eq. (4.12)). We start by examining the effect of $g_-^{(1)}$ coannihilations

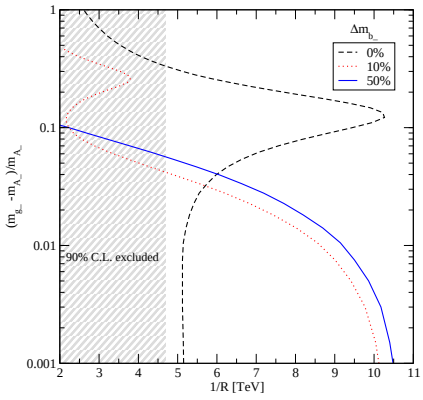

Figure 4.8: Correlation between the $A_-^{(1)} - g_-^{(1)}$ mass splitting and compactification scale for models with Ωh^2 matching the best fit value from cosmological observations, and for a few values of $A_-^{(1)} - b_-^{(1)}$ mass splitting.

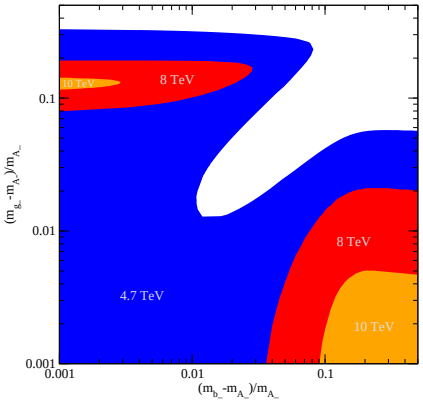

Figure 4.9: For a few selected values of the compactification scale, regions in the parameter space $m_{g_-}^{(1)} - m_{A_-}^{(1)}$ versus $m_{b_-}^{(1)} - m_{A_-}^{(1)}$ in which Ωh^2 is lower or equal to the best fit value from cosmological observations.

alone. In Fig. 4.7 we set $k_b = k_i = 1.5$, removing all antiperiodic fermions from the coannihilation list, and discuss the effect of degeneracies in mass between $g_-^{(1)}$ and $A_-^{(1)}$. In the limit of zero mass splitting we find as upper bound on the compactification scale $1/R \leq 11$ TeV. As expected, the bound on $1/R$ found within the minimal scenario has been relaxed. We also find that, at the lowest allowed value for $1/R$, $(m_{g_-}^{(1)} - m_{A_-}^{(1)})/m_{A_-}^{(1)} \leq 6\%$ must old. Even in the present framework, $g_-^{(1)}$ coannihilations appear as sharp thresholds in the invariant rate. The channels contributing to the annihilation rate are listed in Appendix C. They include the case of annihilation into quarks with the $g_+^{(2)}$ in a s-channel; however, this process always takes place slightly off–resonance, since $|\Delta m_g|$ is of the same size as Γ_g, and it is then always subdominant with respect to the process with gluon final states (one may compare the behavior of the $g_-^{(1)}$-$g_-^{(1)}$ term in the right panel of Fig. 4.7 as a function of $p_{\rm eff}$, with the analogous for the $b_-^{(1)}$-$b_-^{(1)}$ term in Fig. 4.4, where the enhancement due to the resonance is instead evident).

The general framework, with both $g_-^{(1)}$ and $b_-^{(1)}$ playing a role in the relic density calculation, is illustrated in Figs. 4.8 and 4.9. The picture is not a mere overlap of two distinct coannihilation effects. As we have already mentioned, at a given $1/R$ and given mass splitting between $b_-^{(1)}$ and $A_-^{(1)}$, the mass splitting between $g_-^{(1)}$ and $A_-^{(1)}$ sets also $m_{g_+}^{(2)}$ and hence whether the $b_-^{(1)}$ pair annihilation is resonantly enhanced or not. The second effect is due to the fact that we are superimposing coannihilations from states with different

annihilation strength, and, especially, different number of internal degrees of freedom ($g = 24$ for $g_-^{(1)}$): for equal mass splitting, the matching needs to be done at the level of annihilation rates per degree of freedom. The net effect can be both of increasing or lowering the thermal relic abundance for $A_-^{(1)}$. E.g., if we add, on top of a configuration with efficient $g_-^{(1)}$ coannihilations, a $b_-^{(1)}$ state with small mass splitting with the $A_-^{(1)}$, but with mass significantly displaced from the $g_+^{(2)}$ resonance, we are effectively including a set of passive degrees of freedom: maintaining the tower of states in thermal equilibrium becomes more energetically expensive, the freeze-out is anticipated and the thermal relic density increased. This is what happens at small $m_{g_-}^{(1)} - m_{A_-}^{(1)}$ and small $m_{b_-}^{(1)} - m_{A_-}^{(1)}$ in the throat region of Fig. 4.9.

Introducing the $g_-^{(1)}$ in the framework has enlarged the regions in the parameter space which are compatible with the cosmological constraints; still, the tight correlation patterns among parameters in the model, which had emerged in the minimal scheme, are maintained here, although in slightly different forms.

This feature might be view as a sign of fine tuning. To better quantify this point, in analogy to the study of naturalness of radiative electroweak symmetry breaking [273], we introduce the fine-tuning measure [274, 275]:

$$\Delta^{\Omega} \equiv \max \left\{ \frac{\partial \ln(\Omega h^2)}{\partial \ln(a)} \right\}, \tag{4.15}$$

where a labels any of the free parameters in our model. In the minimal DM framework, Δ^{Ω} changes from about 35 in the lower part of Fig. 4.6 to about 8 for the models with largest ρ_s. In the model with antiperiodic gluons, the parameter space with small $m_{b_-}^{(1)} - m_{A_-}^{(1)}$ and intermediate $m_{g_-}^{(1)} - m_{A_-}^{(1)}$ in Fig. 4.9 has a minimum Δ^{Ω} of about 7, while in the limit of large $m_{b_-}^{(1)} - m_{A_-}^{(1)}$ a fine-tuning correlated to the $A_-{}^{(1)}$–$g_-{}^{(1)}$ mass splitting of about 34; finally in the throat region, in which both mass splittings are small, the interplay among the parameters reaches its maximum and, correspondingly, Δ^{Ω} can be as large as 50. Such moderate degree of fine-tuning ($\Delta^{\Omega} \leq 10$ is expected in a "natural" model) is comparable or even smaller than what one obtains in other cases in the literature when the relic density of the WIMP DM candidate is driven by coannihilation effects, see, e.g., [275].

4.3.5 Multi-wavelength signals of $A_-^{(1)}$-annihilations at the GC

In this Section, we apply the procedure described in Chapter 3 to the $A_-^{(1)}$ DM candidate. We derive the induced multi-wavelength signals at the GC and the related constraints on the $A_-^{(1)}$ parameter space.

As already mentioned and arguable from Fig. 4.4, the $A_-^{(1)}$ pair annihilation rate at zero momentum is quite small ($\sigma_{ann}v \lesssim 5 \cdot 10^{-28} cm^3 s^{-1}$) compared to WIMPs in more standard scenarios. Combining EW and cosmological bounds, the $A_-^{(1)}$ mass is constrained in the narrow window 2.35 - 5 TeV. Naturalness arguments can restrict even more the parameter space of the model. Indeed the value for the mass preferred by EW observables is ~ 3 TeV [261] and the fine tuning associated to the DM relic density is minimized by the minimal framework [108], where $A_-^{(1)}$ annihilates only with $b_-^{(1)}$, leading to $(m_{b_-}^{(1)} - m_{A_-}^{(1)})/m_{A_-}^{(1)} \lesssim 7\%$ (see Fig. 4.10a).

In looking for WIMP induced signals of a candidate with a small annihilation rate and a quite heavy mass, it is mandatory to concentrate on a region where the DM density is very large. In the following we focus again on photon emissions at the GC.

Couplings with SM fermions are highly suppressed[7] since the latter (with the exception of bottom and top quarks) are mainly localized on the 4D brane at $y = 0$, where the $A_-^{(1)}$ wavefunction vanishes, being antiperiodic on S^1. As we can see from the mass spectrum in Fig. 4.1, some non–standard states are energetically accessible by the $A_-^{(1)}$ pair annihilation. However, only triplet representations, which are not coupled with boundary fields and have a constant wavefunction in the bulk, largely overlapping the $A_-^{(1)}$ wavefunction. The number of degrees of freedom associated to these fermionic triplets is huge and they constitute the dominant final states of the $A_-^{(1)}$ annihilation cross section. More precisely the annihilation branching ratios are: 75% into $b_+^{(0)}\bar{b}_+^{(0)}$, 24% into $\tau_+^{(0)}\bar{\tau}_+^{(0)}$ and 1% into SM quarks. The subsequent decays of $b_+^{(0)}$ and $\tau_+^{(0)}$ generate quark pairs (38%), τ lepton pairs (6%) and neutrinos (6%), charged (25%) and neutral (12%) weak gauge bosons, and Higgs bosons (12%).

In analogy to Fig. 3.4a, in Fig. 4.10 we show the differential energy spectra per $A_-^{(1)}$–annihilation into γ-rays and $e^+ - e^-$ in the minimal DM framework (variations of the DM mass within the allowed range do not affect the spectra in a sizable way). In the first case, on top of the spectrum originated from π^0 decay, we consider the contribution of primary gamma-rays from final state radiation following the line of Refs. [174] and [192]. The two spectra are soft since quarks and gauge bosons are the dominant annihilation modes. From the point of view of indirect searches, this feature distinguishes $A_-^{(1)}$ from the UED WIMP candidate $B^{(1)}$ [107, 276], whose pairs annihilation branching ratios are dominated by charged leptons and harder spectra are produced. The electron/positron and gamma-ray yields of Fig. 4.10 are at a comparable level, confirming, in this specific case, the general conclusion

[7] This fact implies a very small elastic scattering cross section between $A_-^{(1)}$ and light quarks, and the expected direct DM signals are well below the sensitivity of current detection experiments.

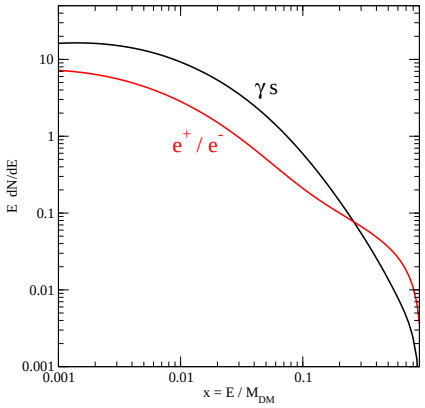

Figure 4.10: Gamma-ray and electron/positron differential spectra per annihilation of the DM candidate $A_-^{(1)}$ in the minimal framework.

drawn from Fig. 3.4b.

As listed in Table C.1, all the $A_-^{(1)}$-annihilation processes occur through t or u-channels mediated by an antiperiodic fermion. At a given DM mass, the only free parameter affecting in a sizable way the cross section computation is the mass of the mediator. As already mentioned before, in the minimal DM framework, the relic abundance is driven mostly by the $b_-^{(1)}$ coannihilation, highly constraining $m_{b_-}^{(1)}$ and hence k_b (see Eq. 4.11). It leads the total $A_-^{(1)}$ annihilation cross section within a small range, since the triplet pairs associated to the b–multiplet are the dominant annihilation modes. The 5D Lorentz symmetry breaking was introduced to achieve the correct value for the top mass; the Lorentz breaking parameter k_i associated to other fermions can be safely taken ~ 1. For our purposes k_b and k_τ are relevant in the computation of the annihilation cross section in the non–minimal scenario, where we assume $k_i \lesssim 2$. The allowed total annihilation cross sections as a function of the WIMP mass are shown in Fig. 4.3.5 by the filled band; in the minimal framework this region shrinks to its upper boundary.

In the determination of the $A_-^{(1)}$-induced emission at the GC, the ingredients related to the particle physics side are quite strictly constrained, while the astrophysical uncertainties remain large, as for any WIMP model. We need a model for the Milky Way halo profile and for the galactic medium, the latter in order to fix the diffusion coefficient, the magnetic field, the advective/convective velocity and the absorption effects. We refer to the analysis discussed in the previous Chapter.

The procedures implemented to extract the limits shown in Figs. 4.3.5a and 4.3.5b are outlined in the previous Chapter, as well. We assume $A_-^{(1)}$ accounting for the whole DM content of the Universe. Together with bounds associated to the mostly investigated profile in this Section, i.e. the A_{sp} pro-

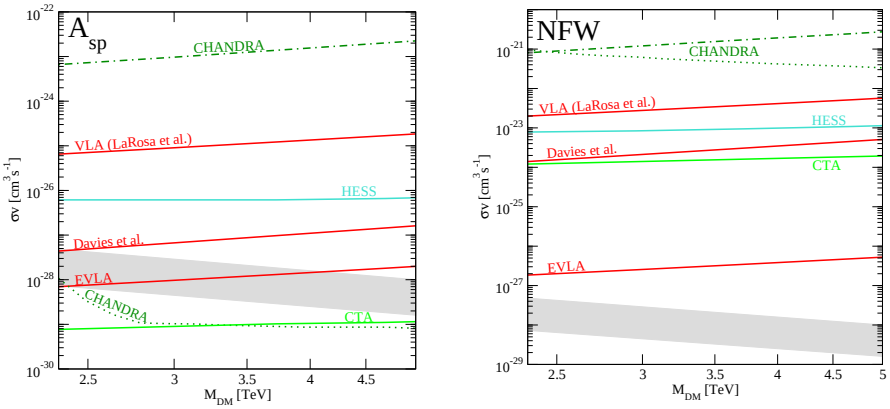

Figure 4.11: Exclusion limits on the $A_{-}^{(1)}$ annihilation cross section as a function of the WIMP mass. The *Left* and *Right Panels* show the cases of A_{sp} and NFW profiles, respectively.

file, we compute, for comparison, limits on the WIMP parameter space in case of a NFW profile, namely the mostly investigated case in the literature. We plot the tightest bounds in gamma-ray and radio bands obtained from spectral and angular analysis, comparing the WIMP signals with the emission detected by the γ-ray HESS ACT [165, 167] and with upper bounds in the radio surveys of Refs. [211] and [216]. In the X-ray band, synchrotron emission would require very strong magnetic field, especially in case of soft electron/positron spectrum. This could be possible only in the innermost region of the Galaxy, depending on the model considered for accretion flow around SMBH, hence the size of the DM induced source is very small. Limits on WIMP parameter space can be extracted by the comparison with the Sgr A* emission detected by the Chandra observatory [219], but they are highly model dependent. We plot the weakest constraint among the three cases with different choice of magnetic field radial profile of Section 3.3. The angular size of the emission induced by the inverse Compton scattering on CMB is much larger and the signature estimate involves more reliable assumptions on the magnetic field strength at larger scales. The limit extracted by the comparison with the detected X-ray diffuse emission [221] (dashed-dotted lines) is much less constraining (but more robust) with respect to the limit associated to the point–like synchrotron source (dotted lines); the fact that the latter is excluding the whole $A_{-}^{(1)}$ parameter space in the A_{sp} case should not be overemphasized, given the critical extrapolations involved in this result.

Then we derive projected limits from forthcoming gamma-ray surveys and wide-field radio observations. For heavy WIMP models, the parameter space can be more efficiently studied by ACTs rather than space satellites, due to the different energy ranges of detection. We consider the next genera-

tion of ACT, with performances as outlined for the CTA project in [239]. A diffuse radio emission was reported both in the Milky Way atlas of Ref. [214] and in the GC image of Ref. [215]. However, the two surveys have too poor angular resolutions to resolve the spatial profile of the emission in the innermost region. In the GC map of Ref. [216], such emission does not seem completely isotropic and tight constraints are derived from patches of the map where no astrophysical background is detected. The radio projected limits plotted in Figs. 4.3.5a and 4.3.5b are extracted again following Ref. [183], but assuming a detector sensitivity improved by a factor 10, as proposed in the EVLA project [236].

The DM spike related to the formation of the SMBH and described in the A_{sp} profile greatly enhances signals in the innermost region of the GC and the comparison with the Sgr A* source is very constraining, especially for $(\sigma v)/M_{DM} \gtrsim 10^{-32} cm^{-3} s^{-1} GeV^{-1}$ [233]. The limits associated to diffuse emissions are less constraining, since involve angular scales where the enhancement in the DM distribution A_{sp} is less pronounced with respect to an NFW profile, being related to the deepening in the potential well induced only by the stellar component. For the same reason, being the DM induced radio source more extended than the DM source itself, and thus than the gamma-ray source, the bound associated to wide field radio signal is less stringent with respect to gamma-ray limit in case of A_{sp} profile. The picture is reversed for the NFW distribution. In the case of the A_{sp} profile, all the multi-wavelength constraints extracted from past surveys, excluding the synchrotron X-ray bound, do not limit the region allowed by cosmological and EW bounds (filled band). On the other hand, in the next decade, the model could be completely tested through its gamma-ray emission by the CTA experiment. The plotted exclusion curve is computed assuming an effective area $\mathrm{A}_{eff} = 1$ km^2 and an exposure time $t_{exp} = 250$ hours in 5 years of collecting data. Depending on the properties of the galactic radio diffuse emission at small scales, the EVLA project could test the $A_{-}^{(1)}$ radio profile in a large fraction of the parameter space, covering basically the whole region of the minimal DM framework. In the case of NFW profile, no significant constraint can be derived. Note however that radio wide field observations can be much more efficient than gamma-ray measurements.

Radio observations with a wide field of view have detected extended emissions from the GC region. In Fig. 4.12a we plot schematic representations of the angular shape of the signals at 90 cm, as detected in the map of Ref. [216] (FWHM=43") and Ref. [215] (FWHM=40'). For both we sketch the profile of the extended source along its longitudinal axis. The level of the DM induced emission filtered over the same experimental angular resolutions is also shown, together with the 3σ sensitivity of the detectors. We take as benchmark case for the $A_{-}^{(1)}$ candidate, a mass of 3 TeV and an annihilation rate of $\sigma_{ann} v = 3 \cdot 10^{-28} cm^3 s^{-1}$. The DM distribution considered is again

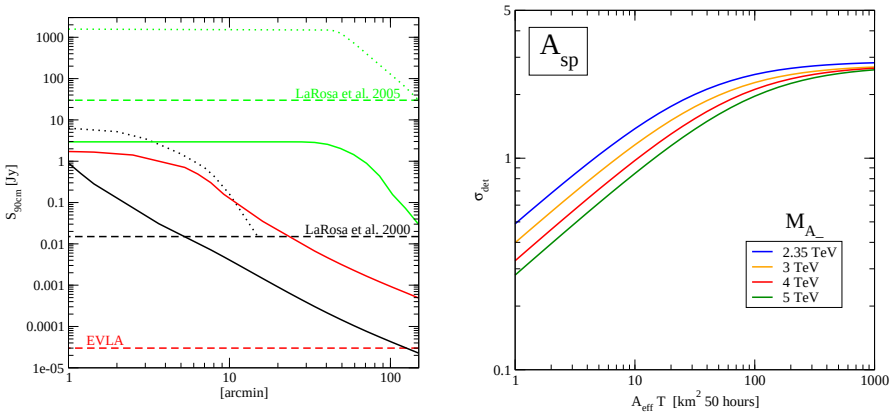

Figure 4.12: *Left Panel*: Angular profiles of the expected DM induced synchrotron source (solid lines) and of the detected diffuse emissions (dotted lines) at 90 cm in the surveys of Refs. [216] (green) and [215] (black). The DM signal profile is shown also for a hypothetical EVLA observation with FWHM=200"(red). We consider as benchmark case the A_{sp} halo profile, $M_{DM} = 3$ TeV and $\sigma_{ann}v = 3 \cdot 10^{-28} cm^3 s^{-1}$. Dashed lines show the experimental sensitivities. *Right Panel*: For a few selected values of the DM mass, detectability of a monochromatic gamma-ray signature by the CTA project as a function of effective area $\times$ exposure time. The latter is expressed in terms of 1 km$^2\times$ 50 hours, which can be considered as a conservative estimate for one year of observation by CTA.

the A_{sp} profile. If the astrophysical radio diffuse emission is approximately isotropic at any scales, bounds on WIMP parameter space that could be extracted are not so stringent, as shown by the green curves, which is averaged over an angular resolution of 40 arcmin. On the other hand, if, on smaller scales, regions with little contamination from astrophysical backgrounds are present, this type of surveys seems to be very promising, as shown in particular by the red curves, representing a hypothetical observation by EVLA with FWHM=200". However, this picture is probably based on a too optimistic assumption and it has to be considered as a limiting case.

So far we have considered only continuum energy spectra of photons and electrons/positrons. The coupling between $A_-^{(1)}$ and electrons is very tiny, since the latter are completely localized on the 4D brane at the boundary of the extra dimension. Thus, for our purposes, the prompt emission in monochromatic electrons and positrons can be neglected.

The real "smoking gun" of a DM induced gamma-ray signal would be a monoenergetic spectral signature. By definition, the DM coupling with photons is highly constrained, but a direct WIMP annihilation into $\gamma\gamma$ at one-loop level is allowed, producing photons with energy $E_\gamma \simeq M_{DM}$. Since A_- is an Abelian gauge boson, this process can occur through fermionic boxes. The main contribution is given by fermion triplets in the loop, for

the same reason (i.e. the delocalization) stated above referring to the tree level annihilation into fermions. The cross section computation is performed following Ref. [277], and obtaining $\sigma_{\gamma\gamma}v \simeq 2{\cdot}10^{-4}\,\sigma_{ann}v$. The total number of events associated to DM annihilations into monochromatic $\gamma\gamma$ in a detector pointing to the GC direction with angular resolution $\Delta\Omega$, is given by:

$$N_{line} = 1.9\ 10^{-13}\frac{\sigma_{line}v}{10^{-31}cm^3s^{-1}}\Big(\frac{\mathrm{TeV}}{M_{DM}}\Big)^2\bar{J}(\Delta\Omega)\Delta\Omega\frac{A_{eff}}{m^2}\frac{T}{s}\,. \qquad (4.16)$$

The quantity $\bar{J}(\Delta\Omega)$, containing all the spatial information, is defined as:

$$\bar{J}(\Delta\Omega) = \frac{1}{8.5\,\mathrm{kpc}}\Big(\frac{1}{0.3\,\mathrm{GeV/cm^3}}\Big)^2\frac{2\pi}{\Delta\Omega}\int d\theta\exp\Big(-\frac{\tan^2\theta}{2\tan^2\theta_d}\Big)\int_{l.o.s.}\rho^2(l)dl\,. \qquad (4.17)$$

The ratio between the gamma-ray signals originated in an A_{sp} and an NFW profiles is given by the ratio: $b = \bar{J}_{A_{sp}}(10^{-5}\mathrm{sr})/\bar{J}_{NFW}(10^{-5}\mathrm{sr})$, assuming $\Delta\Omega = 10^{-5}$ sr for modern ACTs. In the range of mass and cross section of the $A_-^{(1)}$ model, it approximately follows the law: $b \simeq 10^4\cdot\big[\big(\sigma_{ann}v/10^{-28}\mathrm{cm^3s^{-1}}\big)\,(\mathrm{TeV}/M_{DM})\big]^{-0.8}$. The dependence from the ratio $\sigma_{ann}v/M_{DM}$ reflects the fact that the initial DM distribution, from which the A_{sp} profile is derived, has a spike around the SMBH. In this case, self-annihilations frequently occur in the innermost region, triggering the final shape.

The number of events associated to the γ-ray continuum background in a CTA bin can be obtained integrating the spectrum of the detected GC source and of the misidentified showers from hadrons and electrons [200] over an energy resolution of 10%. The probability of disentangling N_l events associated to the DM induced gamma-ray line from N_{bg} events of the continuum background is related to $\sigma_{det} = N_l/\sqrt{N_{bg}+\epsilon_{sys}^2N_{bg}^2}$, where ϵ_{sys} gives the level of systematic errors, taken to be 1% for CTA [239]. We estimate N_l to be a fraction $\epsilon_{DM}\sim 2.7\%$ of the total number of events. At fixed systematic error, the maximal significance which can be achieved increasing the effective area or the exposure time is $\sigma_{det}^{max} = \epsilon_{DM}/\epsilon_{sys}$, i.e. the plateau in Fig. 4.12b. A conservative guess for $\mathrm{A}_{eff}{\times}\mathrm{T}_{exp}$ is 1 km$^2\times$ 50 hours in one year of observation by CTA. As shown in Fig. 4.12b, the prompt monochromatic emission of $\gamma\gamma$ originated from $A_-^{(1)}$ annihilation in an A_{sp} halo profile needs an extra factor of 100 in $\mathrm{A}_{eff}{\times}\mathrm{T}_{exp}$ in order to be detected at $\sim 3\sigma$; this could be reached only with a quite larger setup than the minimal designed and in several years of observation.

Chapter 5

Conclusions

The nature of dark matter is one of the most challenging issue of the physics today. Many gravitational evidences have been accumulated during the last decades. They rely on galactic, cluster and cosmological scales, and are based on different observables, such as rotation curves, velocity dispersions, gravitational lensing, X-ray emissions, large scale structure maps and CMB anisotropies.

Weakly interacting massive particles are a well motivated class of candidates for the non-baryonic component of DM. The WIMP paradigm is well-known: In thermal equilibrium in the primordial bath, WIMPs decouple in the non-relativistic regime and the weak interaction leads the relic abundance to be of the order of the mean energy density of DM in the Universe today. Being (weakly) interacting particles, WIMPs can annihilate in pairs in astrophysical structures, inducing detectable signatures. Complementary to direct DM searches and to collider experiments, indirect detection searches can provide crucial information about the fundamental nature of DM.

We have analyzed the possibility of searching for the multi–wavelength radiation induced by WIMP pair annihilations in dark matter halos, presenting a systematic, self-consistent study of the case in the Galactic center region. The WIMP signal is expected to extend from the radio band up to gamma-ray frequencies. The gamma-ray luminosity is mostly associated to the chain of decays and/or hadronization processes initiated by two-body annihilation channels, leading to the production of neutral pions and their subsequent decays into two photons. In analogous chains, and with comparable efficiencies, high-energy electrons and positrons are produced as well: emitted in a region with large magnetic fields, they give rise to synchrotron emission covering radio frequencies up to, possibly, the X-ray band. A minor role is also played by inverse Compton scattering on the cosmic microwave background or starlight.

Referring to a generic WIMP DM scenario, we have discussed spectral and angular features, and sketched the correlations among signals in the dif-

ferent energy bands. We have illustrated which are the critical assumptions in deriving such conclusions, starting from uncertainties in the DM source functions, regarding both WIMP models and DM distributions, up to the modeling of propagation for electrons and positrons, and the assumptions on magnetic field profiles. We have introduced benchmark cases to guide the discussion and extracted the most relevant general trends: Radio to mm synchrotron emission is essentially independent from the shape of the magnetic field in the innermost region of the Galaxy, while at shorter wavelengths, i.e. in the infrared and, especially, the X–ray band, a different choice for the magnetic field may change predictions dramatically. Radio signals have in general very large angular sizes, larger than the typical size for the source function and hence of the γ-ray signals. The size of the region of synchrotron X-ray emissivity shrinks dramatically going to larger frequencies, smaller WIMP masses, or softer annihilation channels.

The luminosity of the WIMP source at the different frequencies, and especially comparing the radio to the γ-ray band, is essentially at a comparable level, with luminosity ratios depending rather weakly on WIMP mass and annihilation channels. This is interesting, since the GC astrophysical source Sgr A*, an unusual source, certainly very different from typical galactic or extragalactic compact sources associated to black holes, has a very low luminosity over the whole spectrum, at a level at which it is plausible that a WIMP-induced component may be relevant. Indeed, after a closer look, one sees that none of the fluxes detected in GC direction has spectral or angular features typical of a DM source, still all data-sets contribute to place significant constraints on the WIMP parameter space. We have found that, although the γ-ray band is the regime in which it is most straightforward to make the connection between a given dark matter model and the induced signal (hence it is also the regime on which most of previous analyses have concentrated on), it does not seem to be the energy range with the best signal to background ratios. In the case of large magnetic fields close to the GC, X-ray data can give much tighter constraints. Radio and NIR measurements, which are less model dependent, tend to be more constraining as well.

Regarding an outlook for the future, we have explored the capability of improving γ-ray constraints on WIMP models of the FGST satellite telescope, and of CTA as representative of the next generation of air Cherenkov telescopes. The recent discovery of a γ-ray GC source and of a diffuse γ–ray component, however, limits the possibility of dramatic improvements, possibly reducing the region in the parameter space accessible to γ-ray telescopes to regimes that, within the range of assumptions listed in our analysis, are already excluded at other wavelengths. On the other hand, if the Sgr A source has a size in the radio band which is not significantly larger than its presently estimated value, future wide field radio observations could be a new effective way to test WIMP DM models.

One of the most well-motivated class of extensions to the SM of particle physics is given by models with extra-dimensions. We have shown how to embed WIMP dark matter candidates into non-universal flat higher dimensional theories aiming at the stabilization of the electroweak scale. We have focused on a specific model and shown that, in a large fraction of the parameter space, the lightest antiperiodic particle is a stable gauge field with the correct properties for being identified with the DM in the Universe. Although electroweak bounds force its mass to be larger than about 2.3 TeV, and its interaction rate is rather small, coannihilation and resonance effects involving colored particles can delay its decoupling from thermal equilibrium, and allow its relic abundance to be within the range currently favored by cosmological observations.

The picture we have introduced is rather unusual, since the WIMP dark matter candidate is significantly more massive than in standard (e.g. SUSY) scenarios, and its coupling to the SM is essentially limited to third generation quarks. The phenomenology of DM searches for this model is less appealing than in other frameworks; in particular its scattering rate on ordinary matter is suppressed and mediated mainly by radiative effects involving virtual bottom and top quarks. Moreover, its zero temperature pair annihilation rate is small, at the level of few times 10^{-28} cm^3 s^{-1}. We consider the multi–wavelength indirect signal induced the GC, in the case of a spiky halo profile for the Milky Way. Cosmology and EW precision tests fix the DM mass and total annihilation cross section in a narrow window, which is compatible with the bounds associated to the detected emissions at the GC, but can be definitely tested by the forthcoming gamma-ray and wide-field radio surveys. We also discuss the possible detection of an induced gamma-ray line in the same framework. On the other hand, in the case of NFW or more shallow profiles, the possible detection of the $A_-^{(1)}$ DM candidate by its annihilation signals in DM halos becomes very hard.

Nevertheless, embedding the dark matter candidate in the model introduces favored patterns in the parameter space; tests of this framework at future colliders may indeed give crucial information on the DM scenario described in this thesis.

Appendix A

Feynman Rules

In this appendix we give some details about the Feynman rules of our model, focusing in particular on vertices relevant for the calculations of Section 4.3.4. The Lagrangian (aside from ghosts and gauge–fixing terms) is given in Eqs.(2.4)–(2.7) of [261]. The gauge–fixing terms (and the corresponding ghost terms) we use are of the form

$$\mathcal{L}_{gf} = -\frac{1}{2\xi}\sum_a (\partial_\mu A^{\mu,a} - \xi\,\rho\,\partial_5 A_5^a)^2\,, \tag{A.1}$$

for all gauge groups. All cross–sections have been evaluated in the $\xi = 1$ gauge. Since ghosts and gauge bosons A_μ, A_5 are purely bulk fields, ghost, 3-bosons and 4-bosons vertices are easily derived from the usual standard ones. One has only to take into account the Lorentz violation in the fifth dimension replacing $A_5 \to \rho A_5$, $\partial_5 \to \rho\partial_5$ and take the linear combinations $\phi_\pm = (\phi_1 \pm \phi_2)/\sqrt{2}$ for $U(1)_i$ and $SU(3)_{i,s}$ gauge and ghost fields.

Fermion-gauge couplings are more involved, due to the non-trivial profile of fermions in the extra dimensions. The interactions between a gauge boson KK mode p with fermion KK modes m and n can be written as $iT^a g_4\gamma^\mu(c_{L,a}^{(m,n,p)}P_L + c_{R,a}^{(m,n,p)}P_R)$. The coupling g_4 is the 4D gauge coupling, related to the 5D one as $g_4 = g_5/\sqrt{2\pi R}$, the indices p, m, n run over even (odd) integers for $\mathbf{Z}_2$ even (odd) fields and $c_{L/R,a}^{(m,n,p)}$ are the integrals of the wavefunctions along the 5th dimension involving respectively left and right fermion components and broken or unbroken gauge field components $A_{\mu,a}$. In terms of the mode expansion (see Appendix of [261] for further details)

$$\begin{aligned}
\Psi_{L/R} &= \sum_n f_{L/R}^{(n)}(y)\chi_{L/R}^{(n)}\,,\\
\tilde{\Psi}_{L/R} &= \sum_n \tilde{f}_{L/R}^{(n)}(y)\chi_{L/R}^{(n)}\,,\\
q_{L/R} &= \sum_n g_{L/R}^{(n)}\chi_{L/R}^{(n)}\,,
\end{aligned} \tag{A.2}$$

where n in Eq.(A.2) is even (odd) for periodic (antiperiodic) fermions, one gets

$$c_{L/R,a}^{(m,n,p)} = \sqrt{2\pi R}\int_0^{2\pi R} dy\, f_{\mu,a}^{(p)}(y)\Big[f_{1,L/R}^{(n)}(y)f_{2,L/R}^{(m)}(y) + \widetilde{f}_{1,L/R}^{(n)}(y)\widetilde{f}_{2,L/R}^{(m)}(y) + g_1^{(n)}g_2^{(m)}\delta(y)\Big], \tag{A.3}$$

where $f_{\mu,a}^{(p)}(y)$ is the wave–function of the p^{th} KK mode of $A_{\mu,a}(y)$.

As one can check from the Feynman diagrams listed in Appendix C, the relevant couplings in our calculation are:

• $p = 0, m = n$: only gauge bosons of the unbroken SM $SU(2)_L \times U(1)_Y \times SU(3)_s$ gauge group have zero modes, with a constant wavefunction: $f_{\mu,a}^{(0)} = 1/\sqrt{2\pi R}$. The integral in square brackets in Eq. (A.3) is normalized to be 1 in order to have canonical fermion kinetic terms:

$$c_{L/R,a}^{(0,n,n)} = 1, \tag{A.4}$$

implying universal couplings for all fermions, as expected from the unbroken gauge symmetry.

• $p = m = 1, n = 0$: one gets

$$c_{R,a}^{(1,1,0)} = \pm\frac{k\,(k \mp MR)\,\epsilon}{\sqrt{2}\pi RM\,\left(k^2 + M^2R^2\right)\,\sqrt{Z_2}}, \tag{A.5}$$

$$c_{L,a}^{(1,1,0)} = \pm\frac{k_i\,(k_i \mp M_iR)\,\epsilon_i}{\sqrt{2}\pi M_iR\left(k_i^2 + M_i^2R^2\right)\,\sqrt{Z_1}}. \tag{A.6}$$

In Eqs.(A.5) and (A.6), the two different signs refers to the two towers of antiperiodic fermions with same mass and quantum numbers and the Z factors are those appearing in Eq.(2.18) of [260] taken at $\alpha = 0$ (no EWSB). These factors are typically $\simeq 1$, aside from the top quark where they can be substantially bigger ($\simeq 4$ in the chosen setup). In Eq. (A.6), $i = u, d$, depending on the doublet component, and M in Eq. (A.5) should be identified with M_u or M_d, depending on the singlet field under consideration. Similarly for ϵ and k. Antiperiodic fermion and gauge boson wavefunctions vanish at $y = 0$ and thus the overlap with the SM $n = 0$ fields is small, $O(\epsilon)$, except for the top and the left–handed bottom quark, for which one has an overlap $\sim O(1)$.

• $p = 2, m = n = 0$: we are interested only to the fermion gauge couplings to $g^{(2)}$, the first KK mode of $SU(3)_s$. One gets

$$c_{R,g}^{(2,0,0)} = \sqrt{2}\left[1 + 4\epsilon^2\frac{MR}{\pi k(k^2+4M^2R^2)}\coth\left(\frac{\pi MR}{k}\right)\right]Z_2^{-1}, \tag{A.7}$$

$$c_{L,g}^{(2,0,0)} = \sqrt{2}\left[1 + 4\sum_{i=u,d}\epsilon_i^2\frac{M_iR}{\pi k_i(k_i^2+4M_i^2R^2)}\coth\left(\frac{\pi M_iR}{k_i}\right)\right]Z_1^{-1} \tag{A.8}$$

This is a KK-number violating coupling, due to the localized Lagrangian term. As can be seen from Eqs.(A.7) and (A.8), this coupling is $\sim\sqrt{2}$ for all

SM fermions, but the top and the left–handed bottom for which it is much smaller ($\sim \sqrt{2}/Z_2^t$).

• $p = 2, m = n = 1$: again, the only coupling relevant for us is the one with $g^{(2)}$. Only bulk fields are involved and the computation is trivial, giving

$$c_{L/R,g}^{(2,1,1)} = \frac{1}{\sqrt{2}}. \tag{A.9}$$

All effects involving KK states with $p \geq 2$, with the exception of the possible gluon resonance state for $p = 2$, have been neglected.

Analogous considerations can be done for the couplings between fermions and the would–be Goldstone bosons A_5. The vertices can be written as $-kT^a g_4 \gamma^5 (d_{L,a}^{(m,n,p)} P_L + d_{R,a}^{(m,n,p)} P_R)$ where k is the Lorentz breaking factor and

$$d_{L/R,a}^{(m,n,p)} = \sqrt{2\pi R} \int_0^{2\pi R} dy\, f_{a,5}^{(p)}(y) \Big[f_{1,L/R}^{(n)}(y) f_{2,R/L}^{(m)}(y) + \widetilde{f}_{1,L/R}^{(n)}(y) \widetilde{f}_{2,R/L}^{(m)}(y) \Big]. \tag{A.10}$$

The only coupling relevant for us is the one with the colored would-be Goldstone bosons $p = m = 1$, $n = 0$, for which one has

$$\left| d_{L/R,g}^{(1,1,0)} \right| = \frac{\rho_s}{k} \frac{m_{f_-}^{(1)}}{m_{g_-}^{(1)}} \left| c_{L/R,g}^{(1,1,0)} \right| \quad . \tag{A.11}$$

Appendix B

One–loop Gluon Mass Correction

One-loop computations on orbifolds are conveniently performed by using the method of images to map the propagators on $S^1/\mathbf{Z}_2$ to those on the covering circle S^1 [278]. In this way, the vertices conserve the KK number and the KK violation induced by the boundaries is all encoded in a term in the propagator of the bulk fields.

As discussed in the main text, the only radiative correction of interest to us is the mass splitting $\Delta m_g = m_{g^{(2)}} - 2m_{g^{(1)}}$. There are three classes of radiative corrections: i) bulk (finite) corrections induced by bulk fields, ii) localized (divergent) corrections induced by bulk fields and iii) localized (divergent) corrections induced by boundary fermion fields. The corrections i) and ii) are one-to-one, in the formalism of [278], to loop corrections with respectively an even or odd number of insertions of KK-violating propagator terms.

This picture is valid in the limit of vanishing bulk-to-boundary mixing terms ($\epsilon \to 0$), that is a very good approximation for all the fermions but the top. In the latter case, the calculations are more involved, since $\epsilon_t \sim O(1)$ and the corrections ii) and iii) cannot be separated. We have nevertheless checked that the effect of ϵ is negligible in the radiative correction. Indeed, by taking the opposite limit $\epsilon \to \infty$, in which several simplifications occur, the top contribution to the mass splitting varies $\sim 1\%$ with respect to the $\epsilon = 0$ contribution. For all practical purposes, we can thus safely take $\epsilon = 0$ for all SM fields and consider separately contributions ii) and iii).

B.1 Bulk Contributions

Bulk contributions are easily computed. Since there are no bulk fields charged under both $SU(3)_{1,s}$ and $SU(3)_{2,s}$, mirror symmetry constrains the one-loop mass corrections to the gluons g_1 and g_2 (and hence g_+ and g_-) to

be equal. Divergences appear but they are associated with the renormalization of the 5D coupling constant and the Lorentz violating parameter ρ_s. The former does not alter the mass spectrum and the latter dependence clearly cancels in computing Δm_g. What is left is a finite universal correction, similarly to the case of [279]. The purely bosonic and ghost contributions are as in [279], once one rescales $1/R \to \rho_s/R$, since the Feynman rule for periodic and antiperiodic fields are essentially the same. Antiperiodic odd fields running in the loop give only rise to a phase $(-)^w$ after a Poisson resummation on the KK modes is performed. The contributions of virtual odd fields in the diagrams is proportional to $\sum_{w=1}^{\infty}(-)^w/w^3 = -3\zeta(3)/4$, and equals then $(-3/4)$ times the ones of the corresponding even fields, giving a partial cancellation. In total, the gluon and ghost contributions equal

$$\delta m^2_{g^{(n)}}\Big|_{g.+gh.} = \frac{9}{8}\frac{\alpha_s\zeta(3)}{\pi^3}\frac{\rho_s^2}{R^2}\Big(1-\frac{3}{4}\Big)\,. \tag{B.1}$$

Eq. (B.1) is valid for all periodic (even n) and antipeioridc (odd n) modes and is independent of the KK number of the external gluons, with the only exception of the $n = 0$ massless QCD gluons for which one clearly has $\delta m^2_{g^{(0)}} = 0$ by gauge invariance.

Fermion loops are similarly treated, although now the Lorentz breaking cannot be simply rescaled away. For a couple of fermion pairs $(\Psi_{1,2}\tilde{\Psi}_{1,2})$ in the fundamental representation of $SU(3)_{1,2,s}$ with bulk mass M_i and Lorentz breaking parameter k_i, one finds

$$\delta m^2_{g^{(n)}}\Big|_{fer.} \simeq -\frac{\alpha_s k^2}{\pi^3 R^2}\sum_{w=1}^{\infty}\frac{e^{-2w\lambda_i/k_i}}{w^3}\Big(\frac{1+(-)^w}{2}\Big)\Big[1+2w\frac{\lambda_i}{k_i}\Big]\,, \tag{B.2}$$

where $\lambda_i = \pi M_i R$ and we have neglected negligible corrections $O(1-k^2/\rho_s^2)$ in Eq. (B.2). The terms proportional to 1 and $(-)^w$ in Eq. (B.2) correspond (for $\mathbf{Z}_2$ even gluons) to periodic and antiperiodic fermion contributions respectively. As above, a partial cancellation of the mass correction is induced by antiperiodic fields. Again, the mass correction (B.2) is valid for any KK number of the external gluons, but the $n = 0$ gluons.

B.2 Localized Contributions from Bulk Fields

Due to the presence of one non-diagonal propagator, no sum over KK modes has to be performed in the Feynman diagram loop associated to these contributions. The diagrams are effectively four dimensional and logarithmically divergent. Such divergences are cancelled by introducing boundary kinetic counterterms for the gluons at the orbifold fixed points. Strictly speaking, this kind of contributions would then be incalculable, depending on the arbitrary renormalization prescription chosen to cancel these divergences. It

is however possible to estimate their effect by assuming that they are dominated by the calculable radiative corrections of the model. In other words, we require as renormalization prescription the vanishing of these counterterms at a scale of energy equal to the cut-off Λ of the theory.

The mass correction is encoded in the $\eta_{\mu\nu}$ coefficient Π of the gluon vacuum polarization term, taken at $p^2 = m^2_{g^{(n)}}$. Contrary to the bulk terms, boundary corrections also induce mixing between the KK modes, so that a diagonalization of an infinite mass matrix should be performed in order to get the mass eigenvalues. All off–diagonal components are however one–loop induced, so that at one–loop level we can safely neglect such terms and focus only on the diagonal two–point amplitudes. Since the Π factor is given by a 4D loop diagram, its form is the same for periodic and antiperiodic gluons. The only non-trivial issue is the sign of the mass correction. The latter is fixed by the boundary conditions (4.3).[1] The ending result is that no localized mass term is induced at $y = 0$, whereas at $y = \pi R$ the periodic and antiperiodic contributions are equal. The localized mass contributions induced by gluon and ghost fields is found to be ($n > 0$)

$$\delta m^2_{g^{(n)}} = \frac{23\alpha_s}{4\pi} m^2_{g^{(n)}} \ln\left(\frac{\Lambda}{m_{g^{(n)}}}\right), \tag{B.3}$$

where $m_{g^{(n)}} = \rho_s n/(2R)$ is the tree–level mass for periodic and antiperiodic gluons. The localized contributions induced by bulk fermion fields vanish trivially because the KK–violating terms in the fermion propagator contains a γ^5 factor which results in a vanishing trace over the spinor indices. From Eq. (B.3) we get the following one-loop contribution to Δm_g:

$$\Delta m_g = -\frac{23\alpha_s}{8\pi}\frac{\rho_s}{R}\ln 2\,, \tag{B.4}$$

independently of the cut–off Λ.

B.3 Localized Contributions from Boundary Fields

The contributions from colored fermions localized at $y = 0$ is straightforward. Being a purely 4D contribution, it is logarithmically divergent and will be renormalized as described before, requiring the vanishing of the localized operator at the scale Λ.[2]. Boundary fermions do not minimally couple to

[1] Instead of considering periodic and antiperiodic fields, as usual, one could alternatively consider an $S^1/(\mathbf{Z}_2 \times \mathbf{Z}_2')$ orbifold where all fields are periodic but with different orbifold parities at $y = 0$ and $y = \pi R$.

[2] As we have seen, the operator induced by bulk fields is localized only at $y = \pi R$ and thus the renormalization prescription performed here is independent from the one of section B.2.

$g_-^{(n)}$, so that $\delta m^2_{g^{(1)}} = 0$. Summing over all colored fields, for periodic KK gluons ($n > 0$) we find

$$\delta m^2_{g^{(n)}} = -\frac{\alpha_s}{3\pi} m^2_{g^{(n)}} \ln\left(\frac{\Lambda}{m_{g^{(n)}}}\right) \times 12\,. \tag{B.5}$$

We summarize in Table B.3 the different kind of contributions, summed over all the fields in the model.

	Δm_g
i) bulk bosons	$-\frac{27\,\zeta(3)}{16\pi^2}$
i) bulk fermions	$\frac{3}{\pi^2}$
ii) bulk bosons	$-\frac{23}{2}\ln(2)$
ii) bulk fermions	0
iii) boundary fermions	$-8\ln\left(\frac{\Lambda}{m_{g^{(2)}}}\right)$

Table B.1: Summary of mass corrections in terms of $\frac{\alpha_s}{4\pi}\frac{\rho_s}{R}$

For a cut–off scale $\Lambda \simeq (3 \div 4)/R$, the mass splitting Δm_g turns out to be approximately equal to

$$\Delta m_g = m^{(2)}_{g_+} - 2m^{(1)}_{g_-} \simeq -1.4\,\alpha_s \frac{\rho_s}{R}. \tag{B.6}$$

Appendix C

Annihilation and coannihilation processes

We collect in Table C.1 all the matrix elements which are relevant for the computation of the DM relic density. Recall that the bulk fermions are in either the $\bar{\mathbf{3}}_{1/3}$ or $\mathbf{6}_{1/3}$ of $SU(3)_w$, where in the subscript we have denoted their $U(1)$ charge under $U(1)_+$. After EWSB, they decompose as follows under $SU(2)_L \times U(1)_Y$: $\bar{\mathbf{3}}_{1/3} = \mathbf{2}_{1/6} \oplus \mathbf{1}_{2/3}$ and $\mathbf{6}_{1/3} = \mathbf{3}_{2/3} \oplus \mathbf{2}_{1/6} \oplus \mathbf{1}_{-1/3}$. In Table C.1 we have denoted by χ, ψ and ϕ respectively the $SU(2)_L$ singlet, doublet and triplet components of the lightest $n = 1$ KK mode of the 5D antiperiodic bulk fermions Ψ_- in both the $\bar{\mathbf{3}}$ and the $\mathbf{6}$, with the understanding that for the $\bar{\mathbf{3}}$ ϕ (and the corresponding processes) are missing. These fields coincide with the states that we have collectively denoted by $b_-^{(1)}$, $c_-^{(1)}$, etc. in Fig. 4.1 and in the main text. The subscript $a, b = 1, 2$ refers to the two distinct towers of KK mass eigenstates coming from the fermion pairs $(\Psi_-, \tilde{\Psi}_-)$. The SM fermions are denoted by f when we are considering both quarks and leptons and q for quarks only. We denoted by $b_+^{(0)}$ and $\tau_+^{(0)}$ the $n = 0$ KK mode of the $SU(2)_L$ periodic triplets arising from the 5D bulk fermions $\Psi_+^{b,\tau}$, as in Fig. 4.1. For each process, we also write the particle exchanged in the various (s, t, u) channels, whenever the flavor and gauge symmetries allow it. The channels mediated by $g_-^{(1)}$ should be considered only for the framework with a copy of $SU(3)_s$. The fourth column $4p$ indicates when a four-point interaction vertex is present.

In Table C.2 we list the degrees of freedom for the states relevant in the computation of the $A_-^{(1)}$ relic abundance. For fermions we have $D.F. = 2 \times 4\, N_c n_s$, where N_c is the color factor and n_s the number of states in the $SU(3)_w$ multiplet. The overall factor 2 takes into account the presence of two distinct towers for the antiperiodic fermions. In the case of gauge bosons one has simply $D.F. = 3N_g$, where N_g is the number of generators of the gauge group.

	Diagrams			
Process	s	t	u	4p
$A_-^{(1)}A_-^{(1)} \to (f_R\bar{f}_R, f_L\bar{f}_L)$		(χ_a, ψ_a)	(χ_a, ψ_a)	
$A_-^{(1)}A_-^{(1)} \to (b_+^{(0)}\bar{b}_+^{(0)}, \tau_+^{(0)}\bar{\tau}_+^{(0)})$		ϕ_a	ϕ_a	
$\chi_a\bar{\chi}_a \to q_R\bar{q}_R$	$g_+^{(0)}, g_+^{(2)}$	$g_-^{(1)}$		
$\chi_a\bar{\chi}_a \to q_L\bar{q}_L$	$g_+^{(0)}, g_+^{(2)}$			
$\chi_a\bar{\chi}_a \to b_+^{(0)}\bar{b}_+^{(0)}$	$g_+^{(0)}$			
$\chi_a\bar{\chi}_b \to q_R\bar{q}_R$		$g_-^{(1)}$		
$\chi_a\bar{\chi}_a \to g_+^{(0)}g_+^{(0)}$	$g_+^{(0)}$	$g_-^{(1)}$	$g_-^{(1)}$	
$\chi_a\chi_{a,b} \to q_Rq_R$		$g_-^{(1)}$	$g_-^{(1)}$	
$\psi_a\bar{\psi}_a \to q_L\bar{q}_L$	$g_+^{(0)}, g_+^{(2)}$	$g_-^{(1)}$		
$\psi_a\bar{\psi}_a \to q_R\bar{q}_R$	$g_+^{(0)}, g_+^{(2)}$			
$\psi_a\bar{\psi}_a \to b_+^{(0)}\bar{b}_+^{(0)}$	$g_+^{(0)}$			
$\psi_a\bar{\psi}_b \to q_L\bar{q}_L$		$g_-^{(1)}$		
$\psi_a\bar{\psi}_a \to g_+^{(0)}g_+^{(0)}$	$g_+^{(0)}$	$g_-^{(1)}$	$g_-^{(1)}$	
$\psi_a\psi_{a,b} \to q_Lq_L$		$g_-^{(1)}$	$g_-^{(1)}$	
$\phi_a\bar{\phi}_a \to b_+^{(0)}\bar{b}_+^{(0)}$	$g_+^{(0)}$	$g_-^{(1)}$		
$\phi_a\bar{\phi}_a \to (q_R\bar{q}_R, q_L\bar{q}_L)$	$g_+^{(0)}, g_+^{(2)}$			
$\phi_a\bar{\phi}_b \to b_+^{(0)}\bar{b}_+^{(0)}$		$g_-^{(1)}$		
$\phi_a\bar{\phi}_a \to g_+^{(0)}g_+^{(0)}$	$g_+^{(0)}$	$g_-^{(1)}$	$g_-^{(1)}$	
$\phi_a\phi_{a,b} \to b_+^{(0)}b_+^{(0)}$		$g_-^{(1)}$	$g_-^{(1)}$	
$\chi_{a,b}\overset{(-)}{\psi}_{a,b} \to q_R\overset{(-)}{q}_L$		$g_-^{(1)}$		
$\phi_{a,b}\overset{(-)}{\psi}_{a,b} \to b_+^{(0)}\overset{(-)}{q}_L$		$g_-^{(1)}$		
$\phi_{a,b}\overset{(-)}{\chi}_{a,b} \to b_+^{(0)}\overset{(-)}{q}_R$		$g_-^{(1)}$		
$A_-^{(1)}\chi_{a,b} \to g_+^{(0)}q_R$	$\chi_{a,b}$		$\chi_{a,b}$	
$A_-^{(1)}\psi_{a,b} \to g_+^{(0)}q_L$	$\psi_{a,b}$		$\psi_{a,b}$	
$A_-^{(1)}\phi_{a,b} \to g_+^{(0)}b_+^{(0)}$	$\phi_{a,b}$		$\phi_{a,b}$	
$g_-^{(1)}g_-^{(1)} \to (q_R\bar{q}_R, q_L\bar{q}_L)$	$g_+^{(0)}, g_+^{(2)}$	(χ_a, ψ_a)	(χ_a, ψ_a)	
$g_-^{(1)}g_-^{(1)} \to b_+^{(0)}\bar{b}_+^{(0)}$	$g_+^{(0)}$	ϕ_a	ϕ_a	
$g_-^{(1)}g_-^{(1)} \to g_+^{(0)}g_+^{(0)}$	$g_+^{(0)}$	$g_-^{(1)}$	$g_-^{(1)}$	x
$A_-^{(1)}g_-^{(1)} \to (q_R\bar{q}_R, q_L\bar{q}_L)$		(χ_a, ψ_a)	(χ_a, ψ_a)	
$A_-^{(1)}g_-^{(1)} \to b_+^{(0)}\bar{b}_+^{(0)}$		ϕ_a	ϕ_a	
$g_-^{(1)}\chi_{a,b} \to g_+^{(0)}q_R$	$\chi_{a,b}$	$g_-^{(1)}$	$\chi_{a,b}$	
$g_-^{(1)}\psi_{a,b} \to g_+^{(0)}q_L$	$\psi_{a,b}$	$g_-^{(1)}$	$\psi_{a,b}$	
$g_-^{(1)}\phi_{a,b} \to g_+^{(0)}b_+^{(0)}$	$\phi_{a,b}$	$g_-^{(1)}$	$\phi_{a,b}$	

Table C.1: List of all the relevant (co–)annihilation processes. See text for details.

State	$A_-^{(1)}$	$g_-^{(1)}$	$b_-^{(1)}$	$c_-^{(1)}$	$\tau_-^{(1)}$
D.F.	3	24	144	72	48

Table C.2: Degrees of freedom for the states involved in coannihilation.

Bibliography

[1] F. Zwicky, Helv. Phys. Acta **6** (1933) 110.

[2] S. Smith, Astrophys. J. **83** (1936) 23

[3] S. van den Bergh, arXiv:astro-ph/0005314.

[4] V. C. Rubin, N. Thonnard and W. K. . Ford, Astrophys. J. **238** (1980) 471.

[5] Bosma, A. 1981 AJ 86, 1791.

[6] http://lhc.web.cern.ch/lhc/

[7] N. A. Bahcall, J. P. Ostriker, S. Perlmutter and P. J. Steinhardt, Science **284** (1999) 1481 [arXiv:astro-ph/9906463].

[8] M. R. Nolta *et al.* [WMAP Collaboration], arXiv:0803.0593 [astro-ph].

[9] J. Dunkley *et al.* [WMAP Collaboration], arXiv:0803.0586 [astro-ph].

[10] E. Komatsu *et al.* [WMAP Collaboration], arXiv:0803.0547 [astro-ph].

[11] W. J. Percival, S. Cole, D. J. Eisenstein, R. C. Nichol, J. A. Peacock, A. C. Pope and A. S. Szalay, Mon. Not. Roy. Astron. Soc. **381** (2007) 1053 [arXiv:0705.3323 [astro-ph]].

[12] G. Steigman, Int. J. Mod. Phys. E **15** (2006) 1 [arXiv:astro-ph/0511534].

[13] S. Perlmutter *et al.* [Supernova Cosmology Project Collaboration], Astrophys. J. **517** (1999) 565 [arXiv:astro-ph/9812133].

[14] A. G. Riess *et al.* [Supernova Search Team Collaboration], Astron. J. **116** (1998) 1009 [arXiv:astro-ph/9805201].

[15] U. Seljak, A. Slosar and P. McDonald, JCAP **0610** (2006) 014 [arXiv:astro-ph/0604335].

[16] H. Dahle, arXiv:astro-ph/0701598.

[17] N. A. Bahcall, L. M. Lubin and V. Dorman, Astrophys. J. **447** (1995) L81 [arXiv:astro-ph/9506041].

[18] D. Clowe, M. Bradac, A. H. Gonzalez, M. Markevitch, S. W. Randall, C. Jones and D. Zaritsky, Astrophys. J. **648** (2006) L109 [arXiv:astro-ph/0608407].

[19] P. Salucci, arXiv:0707.4370 [astro-ph].

[20] A. Dekel, F. Stoehr, G. A. Mamon, T. J. Cox and J. R. Primack, Nature **437** (2005) 707 [arXiv:astro-ph/0501622].

[21] G. Gilmore, M. I. Wilkinson, R. F. G. Wyse, J. T. Kleyna, A. Koch, N. W. Evans and E. K. Grebel, arXiv:astro-ph/0703308.

[22] M. Mateo, Ann. Rev. Astron. Astrophys. **36** (1998) 435 [arXiv:astro-ph/9810070].

[23] G. Bertone, D. Hooper and J. Silk, Phys. Rept. **405** (2005) 279 [arXiv:hep-ph/0404175].

[24] K. G. Begeman, A. H. Broeils and R. H. Sanders, Mon. Not. Roy. Astron. Soc. **249** (1991) 523.

[25] X. X. Xue *et al.* [SDSS Collaboration], arXiv:0801.1232 [astro-ph].

[26] D. P. Clemens, Astrophys. J. **295**, 422 (1985).

[27] J. F. Navarro, C. S. Frenk and S. D. M. White, Astrophys. J. **490** (1997) 493 [arXiv:astro-ph/9611107].

[28] J. S. Bullock *et al.*, Mon. Not. Roy. Astron. Soc. **321** (2001) 559 [arXiv:astro-ph/9908159].

[29] J. D. Bekenstein, arXiv:astro-ph/0701848.

[30] Milgrom, M., 1983, Astroph. Jour., **270**, 365.

[31] S. McGaugh, arXiv:astro-ph/0606351.

[32] J. D. Bekenstein, Phys. Rev. D **70** (2004) 083509 [Erratum-ibid. D **71** (2005) 069901] [arXiv:astro-ph/0403694].

[33] P. Natarajan and H. Zhao, arXiv:0806.3080 [astro-ph].

[34] T. P. Sotiriou and V. Faraoni, arXiv:0805.1726 [gr-qc].

[35] P. Ivanov, P. Naselsky and I. Novikov, Phys. Rev. D **50** (1994) 7173.

[36] C. Alcock *et al.* [MACHO Collaboration], Astrophys. J. **542** (2000) 281 [arXiv:astro-ph/0001272].

[37] P. Tisserand *et al.* [EROS-2 Collaboration], Astron. Astrophys. **469** (2007) 387 [arXiv:astro-ph/0607207].

[38] Wilkinson, P. N., *et al.* Phys. Rev. Lett. **86** (2001) 584

[39] J. Yoo, J. Chaname and A. Gould, Astrophys. J. **601** (2004) 311 [arXiv:astro-ph/0307437].

[40] R. B. Metcalf and J. Silk, Phys. Rev. Lett. **98** (2007) 071302 [Phys. Rev. Lett. **98** (2007) 099903] [arXiv:astro-ph/0612253].

[41] A. Gould, B. T. Draine, R. W. Romani and S. Nussinov, *Neutron stars: graveyard of charged Dark Matter,* Phys. Lett. B **238** (1990) 337.

[42] S. Davidson, S. Hannestad and G. Raffelt, JHEP **0005** (2000) 003 [arXiv:hep-ph/0001179].

[43] A. Melchiorri, A. Polosa and A. Strumia, *New bounds on millicharged particles from cosmology,* Phys. Lett. B **650** (2007) 416 [arXiv:hep-ph/0703144].

[44] K. Sigurdson, M. Doran, A. Kurylov, R. R. Caldwell and M. Kamionkowski, *Dark-matter electric and magnetic dipole moments,* Phys. Rev. D **70** (2004) 083501 [Erratum-ibid. D **73** (2006) 089903] [arXiv:astro-ph/0406355].

[45] G. D. Mack, J. F. Beacom and G. Bertone, Phys. Rev. D **76** (2007) 043523 [arXiv:0705.4298 [astro-ph]].

[46] J. F. Navarro *et al.*, Mon. Not. Roy. Astron. Soc. **349** (2004) 1039 [arXiv:astro-ph/0311231].

[47] J. Diemand, M. Zemp, B. Moore, J. Stadel and M. Carollo, Mon. Not. Roy. Astron. Soc. **364** (2005) 665 [arXiv:astro-ph/0504215].

[48] A. Klypin, H. Zhao and R. S. Somerville, Astrophys. J. **573** (2002) 597 [arXiv:astro-ph/0110390].

[49] F. Prada, A. Klypin, J. Flix, M. Martinez and E. Simonneau, arXiv:astro-ph/0401512.

[50] M. Gustafsson, M. Fairbairn and J. Sommer-Larsen, Phys. Rev. D **74**, 123522 (2006) [arXiv:astro-ph/0608634].

[51] G. Gentile, P. Salucci, U. Klein, D. Vergani and P. Kalberla, Mon. Not. Roy. Astron. Soc. **351** (2004) 903 [arXiv:astro-ph/0403154].

[52] J. Sommer-Larsen and A. Dolgov, Astrophys. J. **551** (2001) 608 [arXiv:astro-ph/9912166].

[53] M. Fellhauer *et al.*, Astrophys. J. **651** (2006) 167 [arXiv:astro-ph/0605026].

[54] G. Kauffmann, S. D. M. White and B. Guiderdoni, Mon. Not. Roy. Astron. Soc. **264** (1993) 201.

[55] A. A. Klypin, A. V. Kravtsov, O. Valenzuela and F. Prada, Astrophys. J. **522** (1999) 82 [arXiv:astro-ph/9901240].

[56] B. Moore, S. Ghigna, F. Governato, G. Lake, T. Quinn, J. Stadel and P. Tozzi, Astrophys. J. **524** (1999) L19.

[57] P. J. E. Peebles, arXiv:astro-ph/0101127.

[58] G. De Lucia, V. Springel, S. D. M. White, D. Croton and G. Kauffmann, Mon. Not. Roy. Astron. Soc. **366** (2006) 499 [arXiv:astro-ph/0509725].

[59] R. G. Bower *et al.*, Mon. Not. Roy. Astron. Soc. **370** (2006) 645 [arXiv:astro-ph/0511338].

[60] J. R. Primack, Nucl. Phys. Proc. Suppl. **173** (2007) 1 [arXiv:astro-ph/0609541].

[61] M. Taoso, G. Bertone and A. Masiero, JCAP **0803** (2008) 022 [arXiv:0711.4996 [astro-ph]].

[62] S. Mashchenko, H. M. P. Couchman and J. Wadsley, Nature **442** (2006) 539 [arXiv:astro-ph/0605672].

[63] B. Moore, J. Diemand, P. Madau, M. Zemp and J. Stadel, Mon. Not. Roy. Astron. Soc. **368** (2006) 563 [arXiv:astro-ph/0510370].

[64] J. F. Beacom, N. F. Bell and G. D. Mack, Phys. Rev. Lett. **99** (2007) 231301 [arXiv:astro-ph/0608090].

[65] J. Einasto *et al.* [SDSS Collaboration], arXiv:astro-ph/0604539.

[66] K. Abazajian and S. M. Koushiappas, Phys. Rev. D **74** (2006) 023527 [arXiv:astro-ph/0605271].

[67] U. Seljak, A. Makarov, P. McDonald and H. Trac, Phys. Rev. Lett. **97** (2006) 191303 [arXiv:astro-ph/0602430].

[68] M. Viel, J. Lesgourgues, M. G. Haehnelt, S. Matarrese and A. Riotto, Phys. Rev. Lett. **97** (2006) 071301 [arXiv:astro-ph/0605706].

[69] M. Viel, G. D. Becker, J. S. Bolton, M. G. Haehnelt, M. Rauch and W. L. W. Sargent, Phys. Rev. Lett. **100** (2008) 041304 [arXiv:0709.0131 [astro-ph]].

[70] C. Amsler et al. (Particle Data Group), Physics Letters **B667**, 1 (2008)

[71] S. Tremaine and J. E. Gunn, Phys. Rev. Lett. **42** (1979) 407.

[72] J. L. Feng, A. Rajaraman and F. Takayama, Phys. Rev. Lett. **91** (2003) 011302 [arXiv:hep-ph/0302215].

[73] F. Borzumati, T. Bringmann and P. Ullio, Phys. Rev. D **77** (2008) 063514 [arXiv:hep-ph/0701007].

[74] R. D. Peccei and H. R. Quinn, Phys. Rev. Lett. **38** (1977) 1440.

[75] G. G. Raffelt, Lect. Notes Phys. **741** (2008) 51 [arXiv:hep-ph/0611350].

[76] J. E. Kim and G. Carosi, arXiv:0807.3125 [hep-ph].

[77] D. Gorbunov, A. Khmelnitsky and V. Rubakov, arXiv:0805.2836 [hep-ph].

[78] S. Dodelson and L. M. Widrow, Phys. Rev. Lett. **72** (1994) 17 [arXiv:hep-ph/9303287].

[79] A. Kusenko, AIP Conf. Proc. **917** (2007) 58 [arXiv:hep-ph/0703116].

[80] A. Boyarsky, A. Neronov, O. Ruchayskiy and M. Shaposhnikov, Mon. Not. Roy. Astron. Soc. **370** (2006) 213 [arXiv:astro-ph/0512509].

[81] C. R. Watson, J. F. Beacom, H. Yuksel and T. P. Walker, Phys. Rev. D **74** (2006) 033009 [arXiv:astro-ph/0605424].

[82] H. Yuksel, J. F. Beacom and C. R. Watson, arXiv:0706.4084 [astro-ph].

[83] G. Bertone, W. Buchmuller, L. Covi and A. Ibarra, JCAP **0711** (2007) 003 [arXiv:0709.2299 [astro-ph]].

[84] http://sci.esa.int/

[85] J. A. R. Cembranos, J. L. Feng and L. E. Strigari, Phys. Rev. Lett. **99** (2007) 191301 [arXiv:0704.1658 [astro-ph]].

[86] E. W. Kolb, D. J. H. Chung and A. Riotto, arXiv:hep-ph/9810361.

[87] S. Weinberg, Phys. Rev. Lett. **19** (1967) 1264.

[88] S. L. Glashow, J. Iliopoulos and L. Maiani, Phys. Rev. D **2** (1970) 1285.

[89] G. 't Hooft and M. J. G. Veltman, Nucl. Phys. B **44** (1972) 189.

[90] E. W. Kolb and M. S. Turner, Front. Phys. **69** (1990) 1.

[91] K. Griest and M. Kamionkowski, Phys. Rev. Lett. **64** (1990) 615.

[92] K. Griest and D. Seckel, Phys. Rev. D **43** (1991) 3191.

[93] P. Binetruy, G. Girardi and P. Salati, Nucl. Phys. B **237** (1984) 285.

[94] J. Edsjo and P. Gondolo, Phys. Rev. D **56** (1997) 1879 [arXiv:hep-ph/9704361].

[95] P. Gondolo and G. Gelmini, Nucl. Phys. B **360** (1991) 145.

[96] P. Gondolo, J. Edsjo, P. Ullio, L. Bergstrom, M. Schelke and E. A. Baltz, JCAP **0407** (2004) 008 [arXiv:astro-ph/0406204].

[97] H. Baer, K. m. Cheung and J. F. Gunion, Phys. Rev. D **59** (1999) 075002 [arXiv:hep-ph/9806361].

[98] J. Hisano, S. Matsumoto, M. Nagai, O. Saito and M. Senami, Phys. Lett. B **646** (2007) 34 [arXiv:hep-ph/0610249].

[99] M. Cirelli, A. Strumia and M. Tamburini, Nucl. Phys. B **787** (2007) 152 [arXiv:0706.4071 [hep-ph]].

[100] A. Sommerfeld, Ann. Phys. 11 257 (1931).

[101] T. Bringmann and S. Hofmann, JCAP **0407** (2007) 016 [arXiv:hep-ph/0612238].

[102] S. Profumo, K. Sigurdson and M. Kamionkowski, Phys. Rev. Lett. **97** (2006) 031301 [arXiv:astro-ph/0603373].

[103] G. Jungman, M. Kamionkowski and K. Griest, Phys. Rept. **267** (1996) 195 [arXiv:hep-ph/9506380].

[104] L. Bergstrom, Rept. Prog. Phys. **63** (2000) 793 [arXiv:hep-ph/0002126].

[105] C. Arina and N. Fornengo, JHEP **0711** (2007) 029 [arXiv:0709.4477 [hep-ph]].

[106] G. Belanger, A. Pukhov and G. Servant, JCAP **0801** (2008) 009 [arXiv:0706.0526 [hep-ph]].

[107] G. Servant and T. M. P. Tait, Nucl. Phys. B **650** (2003) 391 [arXiv:hep-ph/0206071].

[108] M. Regis, M. Serone and P. Ullio, JHEP **0703** (2007) 084 [arXiv:hep-ph/0612286].

[109] K. Agashe and G. Servant, Phys. Rev. Lett. **93** (2004) 231805 [arXiv:hep-ph/0403143]; JCAP **0502** (2005) 002 [arXiv:hep-ph/0411254].

[110] K. Agashe, A. Falkowski, I. Low and G. Servant, JHEP **0804** (2008) 027 [arXiv:0712.2455 [hep-ph]].

[111] G. Panico, E. Ponton, J. Santiago and M. Serone, Phys. Rev. D **77** (2008) 115012 [arXiv:0801.1645 [hep-ph]].

[112] A. Birkedal, A. Noble, M. Perelstein and A. Spray, Phys. Rev. D **74** (2006) 035002 [arXiv:hep-ph/0603077].

[113] L. Baudis, arXiv:0711.3788 [astro-ph].

[114] http://people.roma2.infn.it/ dama/web/home.html

[115] http://www.physics.ucla.edu/wimps/

[116] http://xenon.astro.columbia.edu/

[117] http://hepwww.rl.ac.uk/ukdmc/project/project.html

[118] http://dmrc.snu.ac.kr/

[119] http://www.klapdor-k.de/index.html

[120] http://www.unizar.es/lfnae/ipaginas/ip0400.html

[121] http://neutrino.lbl.gov/majorana/

[122] http://drift.group.shef.ac.uk/

[123] http://wwwgerda.mppmu.mpg.de/

[124] http://www.cresst.de/

[125] http://mckinseygroup.physics.yale.edu/clean/

[126] http://www-sk.icrr.u-tokyo.ac.jp/xmass/

[127] http://www.snolab.ca/deap1/

[128] people.physics.tamu.edu/jmaxin/Assets/SIGN

[129] http://warp.lngs.infn.it/

[130] http://neutrino.ethz.ch/ArDM/

[131] http://www-coupp.fnal.gov/

[132] http://www.picassoexperiment.ca/

[133] http://cdms.berkeley.edu/

[134] http://edelweiss2.in2p3.fr/

[135] http://www.unizar.es/lfnae/lfnae.html

[136] Z. Ahmed *et al.* [CDMS Collaboration], arXiv:0802.3530 [astro-ph].

[137] http://www-sk.icrr.u-tokyo.ac.jp/sk/index-e.html

[138] http://amanda.uci.edu/

[139] http://icecube.wisc.edu/

[140] http://antares.in2p3.fr/

[141] S. Desai *et al.* [Super-Kamiokande Collaboration], Phys. Rev. D **70** (2004) 083523 [Erratum-ibid. D **70** (2004) 109901] [arXiv:hep-ex/0404025].

[142] L. Bergstrom, J. Edsjo and P. Gondolo, Phys. Rev. D **58** (1998) 103519 [arXiv:hep-ph/9806293].

[143] A. W. Strong, I. V. Moskalenko and V. S. Ptuskin, Ann. Rev. Nucl. Part. Sci. **57** (2007) 285 [arXiv:astro-ph/0701517].

[144] http://pooh.physics.lsa.umich.edu/heat/X

[145] http://pamela.roma2.infn.it

[146] P. Picozza *et al.*, Astropart. Phys. **27** (2007) 296 [arXiv:astro-ph/0608697].

[147] http://ams.cern.ch/

[148] http://astrophysics.gsfc.nasa.gov/astroparticles/programs/bess/BESS.html

[149] http://www.roma2.infn.it/research/comm2/caprice/

[150] T. Bringmann and P. Salati, Phys. Rev. D **75** (2007) 083006 [arXiv:astro-ph/0612514].

[151] F. Donato, N. Fornengo and D. Maurin, arXiv:0803.2640 [hep-ph].

[152] http://www.cita.utoronto.ca/ kaya/gaps.html

[153] E. A. Baltz, M. Battaglia, M. E. Peskin and T. Wizansky, Phys. Rev. D **74** (2006) 103521 [arXiv:hep-ph/0602187].

[154] H. C. Cheng, K. T. Matchev and M. Schmaltz, Phys. Rev. D **66** (2002) 056006 [arXiv:hep-ph/0205314].

[155] http://www-bdnew.fnal.gov/tevatron/

[156] D. Bortoletto [CDF and D0 Collaborations], PoS **HEP2005** (2006) 347.

[157] http://www.linearcollider.org/cms/

[158] R. Bernabei *et al.* [DAMA Collaboration], arXiv:0804.2741 [astro-ph].

[159] C. Savage, G. Gelmini, P. Gondolo and K. Freese, arXiv:0808.3607 [astro-ph].

[160] Talk by M. Boezio at the IDM2008 conference.

[161] C. Boehm, J. Orloff and P. Salati, Phys. Lett. B **641** (2006) 247 [arXiv:astro-ph/0607437].

[162] D. P. Finkbeiner and N. Weiner, Phys. Rev. D **76** (2007) 083519 [arXiv:astro-ph/0702587].

[163] H. A. Mayer-Hasselwander *et al.*, Astron. Astrophys. **335**, 161 (1998).

[164] D. Hooper and B. L. Dingus, Phys. Rev. D **70** (2004) 113007 [arXiv:astro-ph/0210617].

[165] F. Aharonian *et al.* [The HESS Collaboration], Astron. Astrophys. **425** (2004) L13, [arXiv:astro-ph/0408145].

[166] F. Aharonian and A. Neronov, Astrophys. J. **619** (2005) 306 [arXiv:astro-ph/0408303].

[167] F. Aharonian *et al.* [H.E.S.S. Collaboration], Nature **439** (2006) 695 [arXiv:astro-ph/0603021].

[168] J. Albert *et al.* [MAGIC Collaboration], Astrophys. J. **638** (2006) L101 [arXiv:astro-ph/0512469].

[169] K. Tsuchiya *et al.* [CANGAROO-II Collaboration], Astrophys. J. **606** (2004) L115 [arXiv:astro-ph/0403592].

[170] K. Kosack *et al.* [The VERITAS Collaboration], Astrophys. J. **608** (2004) L97 [arXiv:astro-ph/0403422].

[171] C. van Eldik, O. Bolz, I. Braun, G. Hermann, J. Hinton and W. Hofmann [H.E.S.S. Collaboration], arXiv:0709.3729 [astro-ph].

[172] Q. D. Wang, F. J. Lu and E. V. Gotthelf, Mon. Not. Roy. Astron. Soc. **367** (2006) 937 [arXiv:astro-ph/0512643].

[173] D. Horns, Phys. Lett. B **607** (2005) 225 [Erratum-ibid. B **611** (2005) 297] [arXiv:astro-ph/0408192].

[174] L. Bergstrom, T. Bringmann, M. Eriksson and M. Gustafsson, Phys. Rev. Lett. **94** (2005) 131301 [arXiv:astro-ph/0410359].

[175] S. Profumo, Phys. Rev. D **72** (2005) 103521 [arXiv:astro-ph/0508628].

[176] F. Aharonian *et al.* [H.E.S.S. Collaboration], Phys. Rev. Lett. **97** (2006) 221102 [Erratum-ibid. **97** (2006) 249901] [arXiv:astro-ph/0610509].

[177] W. de Boer, C. Sander, V. Zhukov, A. V. Gladyshev and D. I. Kazakov, Astron. Astrophys. **444** (2005) 51 [arXiv:astro-ph/0508617].

[178] A. W. Strong, I. V. Moskalenko and O. Reimer, Astrophys. J. **613** (2004) 962 [arXiv:astro-ph/0406254].

[179] G. Dobler and D. P. Finkbeiner, arXiv:0712.1038 [astro-ph].

[180] D. Hooper, D. P. Finkbeiner and G. Dobler, Phys. Rev. D **76** (2007) 083012 [arXiv:0705.3655 [astro-ph]].

[181] D. Hooper, G. Zaharijas, D. P. Finkbeiner and G. Dobler, Phys. Rev. D **77** (2008) 043511 [arXiv:0709.3114 [astro-ph]].

[182] M. A. Miville-Deschenes, N. Ysard, A. Lavabre, N. Ponthieu, J. F. Macias-Perez, J. Aumont and J. P. Bernard, arXiv:0802.3345 [astro-ph].

[183] M. Regis and P. Ullio, Phys. Rev. D **78** (2008) 043505 [arXiv:0802.0234 [hep-ph]].

[184] G. D. Mack, T. D. Jacques, J. F. Beacom, N. F. Bell and H. Yuksel, arXiv:0803.0157 [astro-ph].

[185] M. Wood *et al.*, arXiv:0801.1708 [astro-ph].

[186] M. Kachelriess and P. D. Serpico, Phys. Rev. D **76** (2007) 063516 [arXiv:0707.0209 [hep-ph]].

[187] E. J. Ahn, G. Bertone and D. Merritt, Phys. Rev. D **76** (2007) 023517 [arXiv:astro-ph/0703236].

[188] S. Colafrancesco, S. Profumo and P. Ullio, Astron. Astrophys. **455** (2006) 21 [arXiv:astro-ph/0507575].

[189] S. Colafrancesco, S. Profumo and P. Ullio, Phys. Rev. D **75** (2007) 023513 [arXiv:astro-ph/0607073].

[190] E. A. Baltz and L. Wai, Phys. Rev. D **70** (2004) 023512 [arXiv:astro-ph/0403528].

[191] A. Tasitsiomi, J. M. Siegal-Gaskins and A. V. Olinto, Astropart. Phys. **21** (2004) 637 [arXiv:astro-ph/0307375].

[192] A. Birkedal, K. T. Matchev, M. Perelstein and A. Spray, arXiv:hep-ph/0507194.

[193] L. Bergstrom, J. Edsjo, P. Gondolo and P. Ullio, Phys. Rev. D **59** (1999) 043506 [arXiv:astro-ph/9806072].

[194] G. Rybicki and A.P. Lightman, 1979, 'Radiative Processes in Astrophysics', John Wiley & Sons Inc.

[195] Talk by C. Frenk at the IDM2008 conference.

[196] J. Diemand, M. Kuhlen, P. Madau, M. Zemp, B. Moore, D. Potter and J. Stadel, Nature **454** (2008) 735 [arXiv:0805.1244 [astro-ph]].

[197] R. Genzel, C. Pichon, A. Eckart, O. E. Gerhard and T. Ott, Mon. Not. Roy. Astron. Soc. **317** (2000) 348 [arXiv:astro-ph/0001428].

[198] A. Ghez, M. Morris, E. E. Becklin, T. Kremenek and A. Tanner, Nature **407** (2000) 349 [arXiv:astro-ph/0009339].

[199] R. Schodel *et al.*, Nature **419**, 694 (2002).

[200] L. Bergstrom, P. Ullio and J. H. Buckley, Astropart. Phys. **9** (1998) 137 [arXiv:astro-ph/9712318].

[201] A. Cesarini, F. Fucito, A. Lionetto, A. Morselli and P. Ullio, Astropart. Phys. **21** (2004) 267 [arXiv:astro-ph/0305075].

[202] D. Hooper, I. de la Calle Perez, J. Silk, F. Ferrer and S. Sarkar, JCAP **0409** (2004) 002 [arXiv:astro-ph/0404205].

[203] N. Fornengo, L. Pieri and S. Scopel, Phys. Rev. D **70** (2004) 103529 [arXiv:hep-ph/0407342].

[204] G. Zaharijas and D. Hooper, Phys. Rev. D **73** (2006) 103501 [arXiv:astro-ph/0603540].

[205] S. Dodelson, D. Hooper and P. D. Serpico, arXiv:0711.4621 [astro-ph].

[206] P. Gondolo, Phys. Lett. B **494** (2000) 181 [arXiv:hep-ph/0002226].

[207] G. Bertone, G. Sigl and J. Silk, Mon. Not. Roy. Astron. Soc. **326** (2001) 799 [arXiv:astro-ph/0101134].

[208] R. Aloisio, P. Blasi and A. V. Olinto, JCAP **0405** (2004) 007 [arXiv:astro-ph/0402588].

[209] L. Bergstrom, M. Fairbairn and L. Pieri, Phys. Rev. D **74** (2006) 123515 [arXiv:astro-ph/0607327].

[210] R. Narayan, R. Mahadevan, J. E. Grindlay, R. G. Popham and C. Gammie, Astrophys. J. **492** (1998) 554 [arXiv:astro-ph/9706112].

[211] R. D. Davies, D. Walsh and R. S. Booth, MNRAS **177** (1976) 319.

[212] F. Melia and H. Falcke, Ann. Rev. Astron. Astrophys. **39**, 309 (2001) [arXiv:astro-ph/0106162].

[213] Z. Q. Shen, K. Y. Lo, M. C. Liang, P. T. P. Ho and J. H. P. Zhao, Nature **438** (2005) 62 [arXiv:astro-ph/0512515].

[214] Haslam, C. G. T., Salter, C. J., Stoffel, H., & Wilson, W. E. 1982, A&AS, 47, 1

[215] T. N. LaRosa, C. L. Brogan, S. N. Shore, T. J. Lazio, N. E. Kassim and M. E. Nord, Astrophys. J. **626** (2005) L23 [arXiv:astro-ph/0505244].

[216] T. N. LaRosa, N. E. Kassim, T. J. W. Lazio and S. D. Hyman, Astrophys. J. **119** (2000) 207.

[217] R. Genzel *et al.*, Nature **425**, 934 (2003) [arXiv:astro-ph/0310821].

[218] Y. Clenet *et al.*, Astron. Astrophys. **417** (2004) L15 [arXiv:astro-ph/0312108].

[219] F. K. Baganoff *et al.*, Astrophys. J. **591** (2003) 891 [arXiv:astro-ph/0102151].

[220] Y. D. Xu, R. Narayan, E. Quataert, F. Yuan and F. K. Baganoff, Astrophys. J. **640** (2006) 319 [arXiv:astro-ph/0511590].

[221] M. P. Muno *et al.*, Astrophys. J. **613** (2004) 326 [arXiv:astro-ph/0402087].

[222] K. Ferriere, W. Gillard and P. Jean, Astron. Astrophys. **467** (2007) 611 [arXiv:astro-ph/0702532].

[223] T. A. Porter, I. V. Moskalenko, A. W. Strong, E. Orlando and L. Bouchet, arXiv:0804.1774 [astro-ph].

[224] M. Morris, arXiv:astro-ph/0701050.

[225] F. Melia, Ap. J. **387**, L25-L28,1992

[226] R. F. Coker and F. Melia, [arXiv:astro-ph/9909411].

[227] D. R. Ballantyne, F. Melia, S. Liu and R. M. Crocker, Astrophys. J. **657** (2007) L13 [arXiv:astro-ph/0701709].

[228] J. Bland-Hawthorn and M. Cohen, Astrophys. J. **582** (2003) 246 [arXiv:astro-ph/0208553].

[229] C. J. Law, arXiv:0705.0114 [astro-ph].

[230] T. Sjostrand, Comput. Phys. Commun. **82**, 74 (1994).

[231] P. Gondolo and J. Silk, Phys. Rev. Lett. **83** (1999) 1719, [arXiv:astro-ph/9906391].

[232] P. Ullio, H. Zhao and M. Kamionkowski, Phys. Rev. D **64** (2001) 043504, [arXiv:astro-ph/0101481].

[233] G. Bertone and D. Merritt, Phys. Rev. D **72** (2005) 103502, [arXiv:astro-ph/0501555].

[234] http://www.vla.nrao.edu/astro/

[235] http://www-glast.slac.stanford.edu/software/IS/glast_lat_performance.html

[236] http://www.aoc.nrao.edu/evla/

[237] http://www.alma.nrao.edu/

[238] http://www.eso.org/projects/vlt/

[239] http://www.mpi-hd.mpg.de/hfm/CTA/CTA_home.html

[240] Lenzen, R., Hofmann, R., Bizenberger, P., & Tusche, A. 1998, Proc. SPIE, 3354, 606.

[241] Rousset, G., et al. 2000, Proc. SPIE, 4007, 72.

[242] R. Morrison and D. McCammon, Astrophys. J. **270** (1983) 119.

[243] Zhao, P., Jerius, D. H., Edgar, R. J., Gaetz, T. J., Van Speybroeck, L. P., Biller, B., Beckerman, E., & Marshall, H. L. 2004, Proc. SPIE, 5165, 482

[244] http://glast.gsfc.nasa.gov/science/swg/feb07/

[245] S. Profumo, Phys. Rev. D **77** (2008) 103510 [arXiv:0801.0740 [astro-ph]].

[246] S. Colafrancesco, P. de Bernardis, S. Masi, G. Polenta and P. Ullio, Astron. Astrophys. **467** (2007) L1 [arXiv:astro-ph/0702568].

[247] P. Blasi, A. V. Olinto and C. Tyler, Astropart. Phys. **18** (2003) 649 [arXiv:astro-ph/0202049].

[248] C. Tyler, Phys. Rev. D **66** (2002) 023509 [arXiv:astro-ph/0203242].

[249] T. E. Jeltema and S. Profumo, arXiv:0805.1054 [astro-ph].

[250] L. E. Strigari, J. S. Bullock, M. Kaplinghat, J. D. Simon, M. Geha, B. Willman and M. G. Walker, Nature **454** (2008) 1096 [arXiv:0808.3772 [astro-ph]].

[251] L. E. Strigari, S. M. Koushiappas, J. S. Bullock, M. Kaplinghat, J. D. Simon, M. Geha and B. Willman, arXiv:0709.1510 [astro-ph].

[252] N. Arkani-Hamed, S. Dimopoulos and G. R. Dvali, Phys. Lett. B **429** (1998) 263 [arXiv:hep-ph/9803315].

[253] L. Randall and R. Sundrum, Phys. Rev. Lett. **83** (1999) 3370 [arXiv:hep-ph/9905221]; Phys. Rev. Lett. **83** (1999) 4690 [arXiv:hep-th/9906064].

[254] J. M. Maldacena, Adv. Theor. Math. Phys. **2** (1998) 231 [Int. J. Theor. Phys. **38** (1999) 1113] [arXiv:hep-th/9711200].

[255] R. Contino and A. Pomarol, Comptes Rendus Physique **8** (2007) 1058.

[256] M. Serone, AIP Conf. Proc. **794**, 139 (2005) [arXiv:hep-ph/0508019].

[257] R. Contino, L. Da Rold and A. Pomarol, Phys. Rev. D **75** (2007) 055014 [arXiv:hep-ph/0612048].

[258] T. Appelquist, H. C. Cheng and B. A. Dobrescu, Phys. Rev. D **64** (2001) 035002 [arXiv:hep-ph/0012100].

[259] C. A. Scrucca, M. Serone, L. Silvestrini, Nucl. Phys. B **669** (2003) 128 [hep-ph/0304220].

[260] G. Panico, M. Serone and A. Wulzer, Nucl. Phys. B **739** (2006) 186 [arXiv:hep-ph/0510373].

[261] G. Panico, M. Serone and A. Wulzer, Nucl. Phys. B **762** (2007) 189 [arXiv:hep-ph/0605292].

[262] B. C. Allanach *et al.*, Part 25, arXiv:hep-ph/0602198.

[263] E. W. Kolb, G. Servant and T. M. P. Tait, JCAP **0307** (2003) 008 [arXiv:hep-ph/0306159].

[264] J. A. R. Cembranos, A. Dobado and A. L. Maroto, Phys. Rev. Lett. **90** (2003) 241301 [arXiv:hep-ph/0302041].

[265] D. Hooper and S. Profumo, Phys. Rept. **453** (2007) 29 [arXiv:hep-ph/0701197].

[266] M. Regis, Phys. Lett. B **663** (2008) 250 [arXiv:0803.0631 [hep-ph]].

[267] K. Kong and K. T. Matchev, JHEP **0601** (2006) 038 [arXiv:hep-ph/0509119].

[268] F. Burnell and G. D. Kribs, Phys. Rev. D **73** (2006) 015001 [arXiv:hep-ph/0509118].

[269] J. R. Ellis, T. Falk and K. A. Olive, Phys. Lett. B **444** (1998) 367 [arXiv:hep-ph/9810360].

[270] J. Edsjo, M. Schelke, P. Ullio and P. Gondolo, JCAP **0304** (2003) 001 [arXiv:hep-ph/0301106].

[271] M. Kakizaki, S. Matsumoto, Y. Sato and M. Senami, Phys. Rev. D **71** (2005) 123522 [arXiv:hep-ph/0502059].

[272] M. Tegmark *et al.*, arXiv:astro-ph/0608632.

[273] R. Barbieri and G. F. Giudice, Nucl. Phys. B **306** (1988) 63.

[274] S. F. King and J. P. Roberts, JHEP **0609** (2006) 036 [arXiv:hep-ph/0603095].

[275] J. R. Ellis and K. A. Olive, Phys. Lett. B **514** (2001) 114 [arXiv:hep-ph/0105004].

[276] H. C. Cheng, J. L. Feng and K. T. Matchev, Phys. Rev. Lett. **89** (2002) 211301 [arXiv:hep-ph/0207125].

[277] L. Bergstrom, T. Bringmann, M. Eriksson and M. Gustafsson, JCAP **0504** (2005) 004, [arXiv:hep-ph/0412001].

[278] H. Georgi, A. K. Grant and G. Hailu, Phys. Lett. B **506** (2001) 207 [arXiv:hep-ph/0012379].

[279] H. C. Cheng, K. T. Matchev and M. Schmaltz, Phys. Rev. D **66**, 036005 (2002) [arXiv:hep-ph/0204342].